UNIVERSIDADE FEDERAL DO RIO GRANDE DO SUL

CENTRO DE BIOTECNOLOGIA

PROGRAMA DE PÓS-GRADUAÇÃO EM BIOLOGIA CELULAR E MOLECULAR

COMPARAÇÃO DE DIFERENTES CAMPOS DE FORÇA NA DESCRIÇÃO CONFORMACIONAL DE siRNAs

Pablo Ricardo Arantes

Porto Alegre – Brasil

Outubro de 2014

Comparação de diferentes campos de força na descrição conformacional de siRNAs

Pablo Ricardo Arantes

Dissertação de Mestrado elaborada no Grupo de Bioinformática Estrutural do Centro de Biotecnologia da Universidade Federal do Rio Grande do Sul sob orientação do professor doutor

Hugo Verli

Porto Alegre – Brasil

Outubro de 2014

Comparação de diferentes campos de força na descrição conformacional de siRNAs

Pablo Ricardo Arantes

Dissertação submetida ao Programa de Pós-Graduação em Biologia Celular e Molecular do Centro de Biotecnologia da Universidade Federal do Rio Grande do Sul como parte dos requisitos necessários para a obtenção do grau de Mestre em Biologia Celular e Molecular.

Banca Examinadora:

Prof. Hugo Verli
Centro de Biotecnologia - UFRGS
Orientador

Prof. Rogério Margis
Centro de Biotecnologia – UFRGS

Prof. Thereza Amélia Soares da Silva
Departamento de Química Fundamental – UFPE

Dr. Rodrigo Ligabue Braun
Pós-Doutor - PUCRS

Prof. Márcio Dorn (suplente)
Instituto de Informática - UFRGS

Esta dissertação foi desenvolvida sob a orientação do Professor Doutor Hugo Verli, com o apoio financeiro do Conselho Nacional de Desenvolvimento Científico e Tecnológico (CNPq), da Coordenação de Aperfeiçoamento de Pessoal de Nível Superior (CAPES) e da Fundação de Amparo à Pesquisa do Rio Grande do Sul (FAPERGS), como requisito para obtenção do grau de Mestre em Biologia Celular e Molecular, junto ao Centro de Biotecnologia da Universidade Federal do Rio Grande do Sul.

FICHA CATALOGRÁFICA

Arantes , Pablo Ricardo
Comparação de diferentes campos de força na descrição conformacional de siRNAs / Pablo Ricardo Arantes . -- 2014.
94 f.

Orientador: Hugo Verli.

Dissertação (Mestrado) -- Universidade Federal do Rio Grande do Sul, Centro de Biotecnologia do Estado do Rio Grande do Sul, Programa de Pós-Graduação em Biologia Celular e Molecular, Porto Alegre, BR-RS, 2014.

1. Biologia Computacional. 2. Dinâmica Molecular . 3. Ácidos Nucleicos. 4. Campos de Força. 5. siRNA. I. Verli, Hugo , orient. II. Título.

AGRADECIMENTOS

Primeiramente, gostaria de agradecer amplamente ao Professor Hugo Verli, pelo pelos ensinamentos, pelo exemplo de conduta científica e pela dedicação ao meu trabalho. Sinto-me honrado em fazer parte do seu grupo de pesquisa.

Aos membros da comissão de acompanhamento, Dr. Rogério Margis e Dr. Paulo Augusto Netz, pelo suporte durante toda a realização deste trabalho.

Ao Programa de Pós-Graduação em Biologia Celular e Molecular, pela oportunidade de realização do trabalho.

À Silvia e ao Luciano, pelo profissionalismo e pelo bom humor, mantido em todas as situações.

Aos membros da banca examinadora, por aceitarem o convite.

Aos colegas e amigos do Grupo de Bioinformática Estrutural, obrigado pelo companheirismo, pela ajuda, pela paciência e por me fazerem rir mesmo quando não era permitido.

Aos meus pais, pelo amor e apoio incondicional em todas as minhas escolhas (inclusive no presente trabalho). Pela enorme dedicação e confiança, que possibilitaram-me chegar até aqui. Obrigado Adriana e Sergio, por todo esforço e incentivo para meu crescimento intelectual e como ser humano.

Por fim e não menos importante, a minha noiva (até que enfim, né?) Mariana por todo amor, carinho, paciência e dedicação durante a realização deste trabalho. Obrigado por estar sempre ao meu lado, incentivando meu crescimento intelectual e profissional, pelo companheirismo e por fazer os meus dias cada vez mais felizes. TE AMO!!!

"Science and everyday life cannot and should not be separated."

Rosalind Franklin (1920-1958)

"It's always impossible, until it's done."

Nelson Mandela (1918-2013)

SUMÁRIO

LISTA DE ABREVIATURAS ix

RESUMO x

ABSTRACT xi

ÍNDICE DE FIGURAS xii

1. INTRODUÇÃO 1

1.1 VIA DO RNA DE INTERFERÊNCIA 1

1.2 ESTRUTURA DO siRNA 7

1.3 O PAPEL DA DINÂMICA MOLECULAR NA CARACTERIZAÇÃO CONFORMACIONAL DE ÁCIDOS NUCLEICOS 11

1.4 CAMPOS DE FORÇA 15

2. OBJETIVOS 18

3. MÉTODOS 19

3.1 PROGRAMAS UTILIZADOS 20

3.2 PREPARAÇÃO DO SISTEMA 21

3.4 ANÁLISE DOS RESULTADOS 23

4. RESULTADOS 24

4. 1 PREÂMBULO 24

5. DISCUSSÃO GERAL 35

5. 1 ANÁLISE GLOBAL DA ESTRUTURA 35

5. 2 ÂNGULOS TORCIONAIS E PARÂMETROS GEOMÉTRICOS 37

6. CONCLUSÕES 39

7. PERSPECTIVAS ..... **Error! Bookmark not defined.**

8. REFERÊNCIAS BIBLIOGRÁFICAS 40

9. APÊNDICES 45

10. CURRICULUM VITÆ 76

LISTA DE ABREVIATURAS

Ago	Argonauta
CG	*Coarse-grained*
DNA	Ácido desoxirribonucleico
RNA	Ácido ribonucleico
RNAi	RNA de interferência
siRNA	*Small interfering* RNA
miRNA	MicroRNA
piRNA	*Piwi-associated* RNA
mRNA	RNA mensageiro
tRNA	RNA transportador
rRNA	RNA ribossômico
SPC	*Single point charge*
DM	Dinâmica Molecular
FF	*Force Field*
PME	*Particle Mesh Ewald*
PDB	*Protein Data Bank*
RISC	*RNA-induced silencing complex*
RMN	Ressonância Magnética Nuclear
RMSD	*Root Mean Square Deviation*

RESUMO

siRNAs são pequenos RNAs de interferência de cadeia dupla que podem silenciar a expressão de genes específicos pós-transcricionalmente. A despeito de suas importantes funções biológicas, poucos estudos vêm se dedicando a abordá-los sob a perspectiva atomística. Com relação às técnicas computacionais, existem ainda poucas informações sobre a confiabilidade das predições *in silico* realizadas com estas pequenas moléculas de RNA de fita-dupla. Neste contexto, o presente trabalho compara os campos de força AMBER, CHARMM e GROMOS na descrição conformacional de siRNAs livres e complexados a proteína p19, através de simulações por dinâmica molecular. Destes, AMBER e CHARMM mantiveram a conformação molecular dos siRNAs similar à geometria cristalográfica, enquanto o GROMOS introduziu uma série de distorções, conforme descrito previamente para a molécula de DNA (RICCI ET AL., 2010). De forma geral, a complexação à p19 promoveu um aumento na rigidez dos siRNAs. Em contrapartida, os problemas apresentados pelo GROMOS foram extensos, incluindo abertura da dupla-hélice e perda do pareamento, possivelmente através de problemas nos ângulos torcionais descritores do esqueleto conformacional dos siRNAs. Assim, os dados obtidos apontam para AMBER e CHARMM como os principais campos de força para simulações de pequenos RNAs. Por outro lado, observamos potenciais pontos de partida para melhoria do GROMOS na descrição de ácidos nucleicos, o que permitiria simulações cobrindo escalas de tempo maiores em máquinas de custos menores.

ABSTRACT

The small interfering RNA (siRNA), which are small pieces of double-stranded RNA, can silence the expression of specific genes at the post-transcriptional level. While such molecules have an important biological function, only few studies have been dedicated to approach them under the atomistic perspective. Regarding the computational techniques, there is little information on the reliability of *in silico* predictions performed with these small double-strands RNA molecules. In this context, the current work intends to compare AMBER, CHARMM and GROMOS force fields on the conformational description of p19 protein complexed and uncomplexed siRNAs under molecular dynamics simulations. AMBER and CHARMM force fields behaved similarly to the crystallographic geometry, while GROMOS force field shows a series of distortions, as previously described in DNA simulations (RICCI ET AL., 2010). When complexed to p19, the dynamics of the siRNA demonstrated an increase in its rigidity. On the other hand, the problems presented on GROMOS force field were extensive, including opening of double strands, and loss of base pairing, possibly due to problems with backbone torsional angles of siRNAs. Thus, the obtained data points to AMBER and CHARMM as the main force fields for simulations of small RNAs. Moreover, we observed potential starting points for improving the GROMOS force field on the nucleic acids description, allowing simulations covering longer time scales at lower cost machines.

ÍNDICE DE FIGURAS

Figura 1. Representação tridimensional dos RNAs, bem como dos RNAs de interferência.....1

Figura 2. Primeira descrição fenotípica do RNA de interferência. As partes brancas nas flores de petúnia representam as áreas na qual o RNAi silenciou a expressão de um determinado gene relacionado com a coloração das flores. 2

Figura 3. Representação das vias de silenciamento da expressão gênica pelo miRNA (A) e piRNA (B). ..3

Figura 4. Representação da via do RNA de interferência para o siRNA. A proteína p19 do *tombusvirus*, que realiza o impedimento da ligação do complexo RISC, também esta representada na figura. 6

Figura 5. Representação esquemática dos nucleotídeos que compõe o siRNA e suas variações na base nitrogenada. 7

Figura 6. Os sete ângulos torcionais que especificam a conformação de cada nucleotídeo na cadeia do siRNA. O carboidrato ligado ao grupamento fosfato é caracterizado por seis ângulos torcionais. A orientação da base em relação ao carboidrato é especificada pela ligação glicosídica, um único ângulo torsional. 8

Figura 7. Parâmetros geométricos empregados como descritores da geometria dos siRNAs. 8

Figura 8. Estrutura primária e tridimensional de um siRNA, em ambas representações as extremidades coesivas estão destacadas. 10

Figura 9. Representação da equação de movimento de Newton. A proteína AT-glicosilada é apresentada como resultado da aplicação desta equação sobre seus sistema. 12

Figura 10. (A) Representação das condições periódicas de contorno em uma simulação de DM. (B) Representação do efeito de diferentes tempos de integração na amostragem de DM. 14

Figura 11. Representação dos termos que compõem os campos de força empregados em dinâmica molecular. 16

Figura 12. Representação dos aminoácidos em um campo de força descrevendo todos os átomos (verde), átomo unido (vermelho) e *coarse-grained* (azul).....17

Figura 13. Representação de sistemas construídos com diferentes tipos campos de força. Esta demonstrado também a utilização de dois tipos campos de força em uma mesmo sistema, chamado sistema híbrido. 17

Figura 14. Representação da metodologia utilizada para o estudo conformacional e estrutural dos siRNAs. Sistemas do siRNA complexado a proteína p19 na parte superior e siRNA livre na parte inferior da imagem. 19

Figura 15. Representação das estruturas de RNA e DNA, respectivamente, utilizadas para o estudo conformacional no presente trabalho. 21

Figura 16. Critério geométrico adotado para a existência de ligações intramoleculares de hidrogênio. D = Doador, A = Aceptor. 23

Figura 17. Diferenças estruturais apresentadas pelos siRNAs durante as simulações por DM nos três campos de força. 36

Figura 18. Perfis torcionais de energia, para os ângulos α e γ, calculados a partir dos parâmetros dos campos de força AMBER e GROMOS. 38

1. INTRODUÇÃO

1.1 VIA DO RNA DE INTERFERÊNCIA

Três tipos principais de moléculas de RNAs participam durante a tradução de proteínas em eucariotos: RNA mensageiro (mRNA), RNA transportador (tRNA) e RNA ribossômico (rRNA) (Figura 1). Além desses, existem pequenos RNAs que não são traduzidos em proteínas. Em vez disto, esses pequenos RNAs de 20 a 30 nucleotídeos, com sequência complementar à porções do transcrito de mRNA, regulam a expressão de determinados genes, interferindo no processo traducional. Esse processo, pós-transcricional, é conhecido como via do RNA de interferência ou via do silenciamento da expressão gênica (GROßHANS & FILIPOWICZ, 2008; MEISTER & TUSCHL, 2004). A descoberta desses pequenos RNAs e seu papel no silenciamento da expressão gênica alterou profundamente o entendimento da regulação gênica (NOVINA & SHARP, 2004).

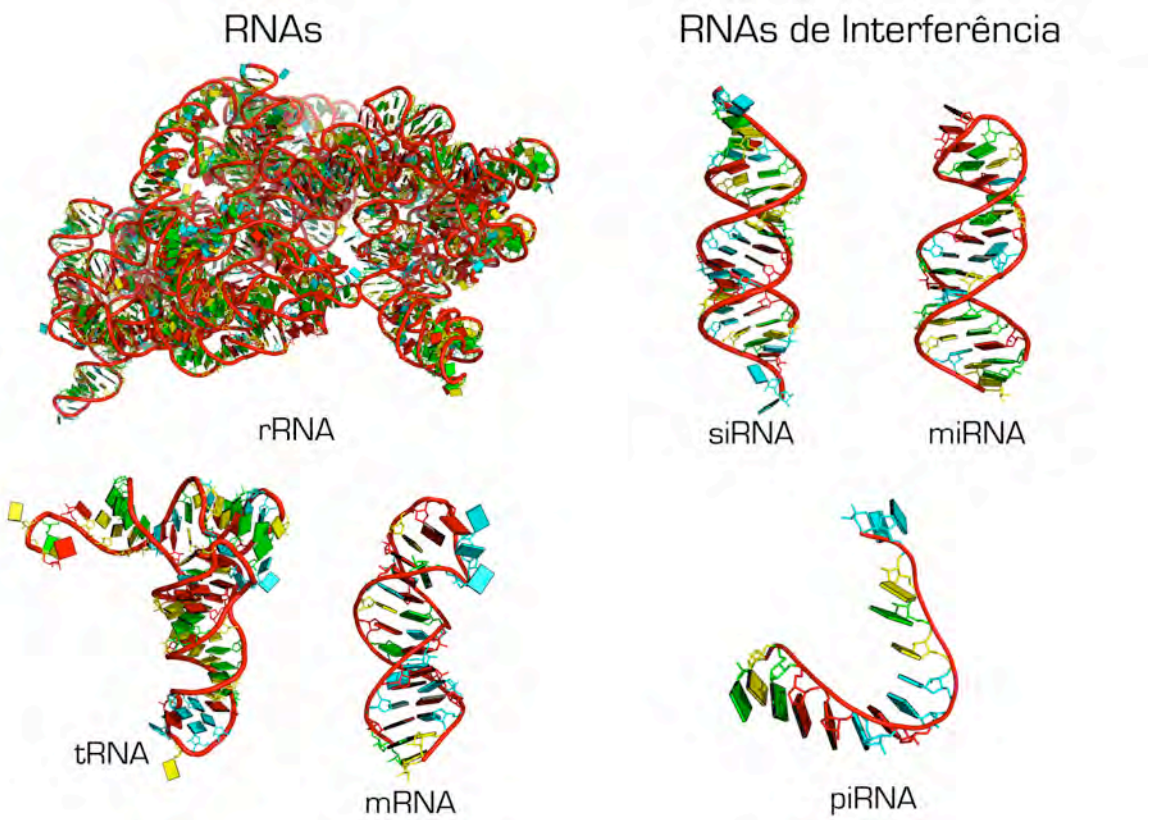

Figura 1. Representação tridimensional dos RNAs, bem como dos RNAs de interferência.

Esses pequenos ácidos nucleicos recebem o nome de RNAs de silenciamento ou RNAs de interferência (RNAi). Primeiramente encontrados apenas em plantas (Figura 2), estão presentes em eucariotos (MEISTER & TUSCHL, 2004; NOVINA & SHARP, 2004). Essa via de silenciamento foi descoberta como um mecanismo de defesa à infecção viral, protegendo o organismo do RNA viral e também prevenindo a integração aleatória dos elementos genéticos móveis (transposons) (MEISTER & TUSCHL, 2004). Existem diferentes classes de RNAs de interferência regulatórios, sendo as principais os microRNAs (miRNAs), RNAs associados a proteínas da subfamília Piwi (piRNAs) e pequenos RNAs de interferência (siRNAs) (Figura 1) (GROßHANS & FILIPOWICZ, 2008; JINEK & DOUDNA, 2009)

Figura 2. Primeira descrição fenotípica do RNA de interferência. As partes brancas nas flores de petúnia representam as áreas na qual o RNAi silenciou a expressão de um determinado gene relacionado com a coloração das flores (adaptado de GROßHANS & FILIPOWICZ, 2008).

Os miRNAs são codificados por genes específicos, os quais têm a função de reprimir a tradução do mRNA e de direcionar esse mRNA para a degradação (Figura 3A) (HANNON, 2002; GROßHANS & FILIPOWICZ, 2008; JINEK & DOUDNA, 2009). Na via de silenciamento da expressão gênica dos miRNAs, o transcrito primário contendo de 60 a 70 pares de bases (pri-miRNA, embora alguns segmentos de bases não sejam pareados), forma uma estrutura de grampo (*hairpin*) dentro do núcleo celular. Essa estrutura é processada pela enzima Drosha em um precursor do miRNA (pré-miRNA) e transportado para o

citoplasma. Dicer, uma enzima da família RNase III, realiza a clivagem do pré-miRNA, originando um duplex de miRNA. Esse pequeno RNA possui uma fita denominada passageira e uma fita denominada guia, que possibilitarão o reconhecimento do miRNA pela proteína Argonauta (Ago). Esta proteína Ago, é o elemento central de um sistema ribonucleoprotéico denominado complexo de silenciamento induzido por RNA (RISC). Este complexo utiliza a fita guia do miRNA para se ligar à sequência específica de silenciamento no mRNA. A partir do reconhecimento da sequência complementar do miRNA no mRNA, ocorre a ligação do complexo RISC, impedindo que o ribossomo se ligue ao RNA e realize a tradução. Além da repressão da tradução, o complexo RISC também realiza a remoção da cauda poli (A) na extremidade 3' do mRNA, direcionando esse ácido nucleico para a degradação (HANNON, 2002; GROßHANS & FILIPOWICZ, 2008; JINEK & DOUDNA, 2009).

O segundo tipo de RNAi compreende os piRNAs, de 24 a 31 nucleotídeos que têm como função principal o silenciamento dos transposons em células germinativas (JINEK & DOUDNA, 2009; GROßHANS & FILIPOWICZ, 2008). O mecanismo de ação desses pequenos ácidos nucleicos não está completamente esclarecido, embora algumas etapas já estejam elucidadas. Sabe-se que o precursor desse RNA é uma fita simples, pois a sua biogênese não necessita de uma enzima da família das RNases (JINEK & DOUDNA, 2009). Esses RNAs induzem um sistema recíproco de clivagem senso e anti-senso nos elementos de transposons (Figura 3B). Esse processo é mediado pelo complexo Piwi, formado pelas proteínas Piwi, Aubergina (AUB) e Argonautas (AGO3). O processo de silenciamento é iniciado com a proteína Piwi ou AUB realizando o corte das fitas senso dos transcritos de transposons, originando fitas senso de piRNAs. Estas são direcionadas à fita anti-senso de outro transcrito de transposon pela proteína AGO3. Os produtos dessa clivagem dão origem às fitas anti-senso de piRNAs, que por sua vez se ligam ao complexo Piwi, o qual orienta o corte das fitas senso dos transcritos de transposons, originando fitas senso de piRNAs (Figura 3B) (JINEK & DOUDNA, 2009). Esse processo é cíclico, permitindo que o mRNA seja processado corretamente e posteriormente utilizado no processo traducional em células germinativas.

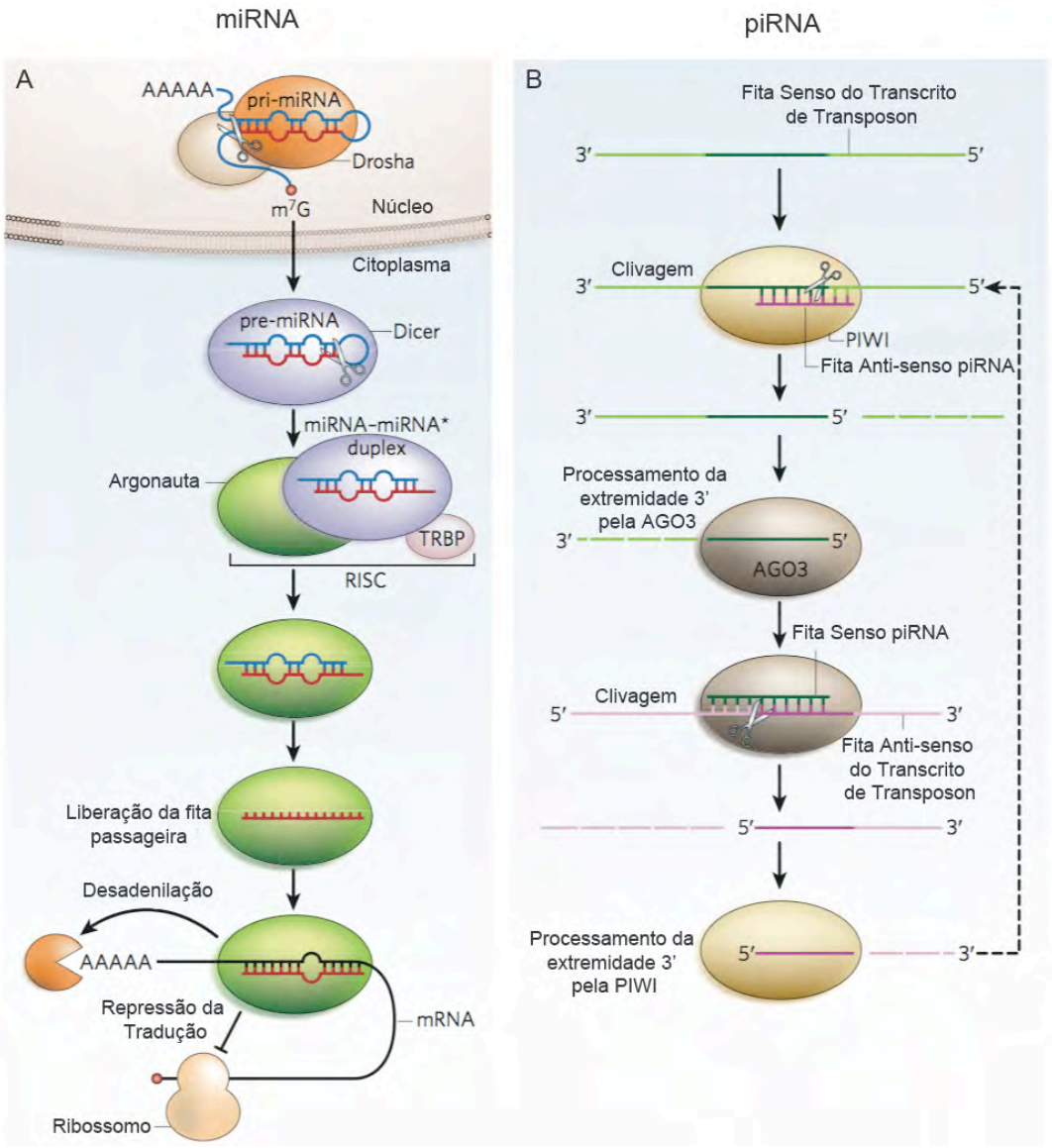

Figura 3. Representação das vias de silenciamento da expressão gênica pelo miRNA (A) e piRNA (B) (adaptado de JINEK & DOUDNA, 2009).

A terceira classe de RNAi, os pequenos RNA de interferência (siRNA), são moléculas derivadas de um longo RNA de fita dupla em resposta à replicação do RNA viral, à transcrição em convergência de genes celulares ou aos elementos genéticos móveis (GROßHANS & FILIPOWICZ, 2008; JINEK & DOUDNA, 2009; MEISTER & TUSCHL, 2004). Inicialmente, esse longo RNA é clivado pela endonuclease Dicer em pequenos RNAs de fita dupla com 20 a 25 nucleotídeos. Em seguida, uma a fita guia do siRNA é direcionada pela proteína Ago ao núcleo do complexo RISC, permitindo que a fita passageira seja clivada pela Ago e, assim, liberada do complexo RISC. A proteína Ago utiliza a fita guia para se associar ao mRNA através da complementaridade de sequência para então realizar a clivagem deste RNA. Os fragmentos de mRNA

resultantes são alvos para a outras enzimas que realizarão a degradação deste transcrito (Figura 4) (GROßHANS & FILIPOWICZ, 2008; JINEK & DOUDNA, 2009).

Existem vírus, encontrados principalmente em plantas, capazes de expressar determinadas proteínas que se ligam aos RNAs de interferência e impedem a ligação da proteína Argonauta (YE ET AL., 2003). Essa associação impede a ligação dos RNAs ao complexo RISC, suprimindo a atividade de silenciamento da expressão gênica. Como exemplo, o *tombusvirus,* que pode ser encontrado em tomates, expressa uma proteína chamada p19 (Figura 4), que interage com o siRNA impedindo a ligação do complexo RISC e permitindo a expressão de genes presentes no RNA viral. Como resultado desta contra-defesa, o vírus consegue expressar suas proteínas usando os componentes celulares da planta e se propaga pelo organismo (YE ET AL., 2003).

Os RNAs de interferência podem ser utilizados tanto na clínica quanto no laboratório. Os siRNAs, potencialmente, podem ser utilizados para silenciar genes relevantes a determinadas doenças (GROßHANS & FILIPOWICZ, 2008). Um dos maiores desafios para esta alternativa terapêutica é conseguir que o RNA se ligue de forma eficiente e específica no seu sitio de ação no organismo. Independente do seu potencial terapêutico, os siRNAs já revolucionaram a pesquisa biomédica básica. O uso de siRNAs sintéticos, grampos (*hairpins*) de RNA ou precursores de RNA fita dupla, permitem aos pesquisadores suprimir a função de um gene ou até mesmo elucidar rotas biológicas com facilidade e velocidade sem precedentes (HANNON, 2002; GROßHANS & FILIPOWICZ, 2008).

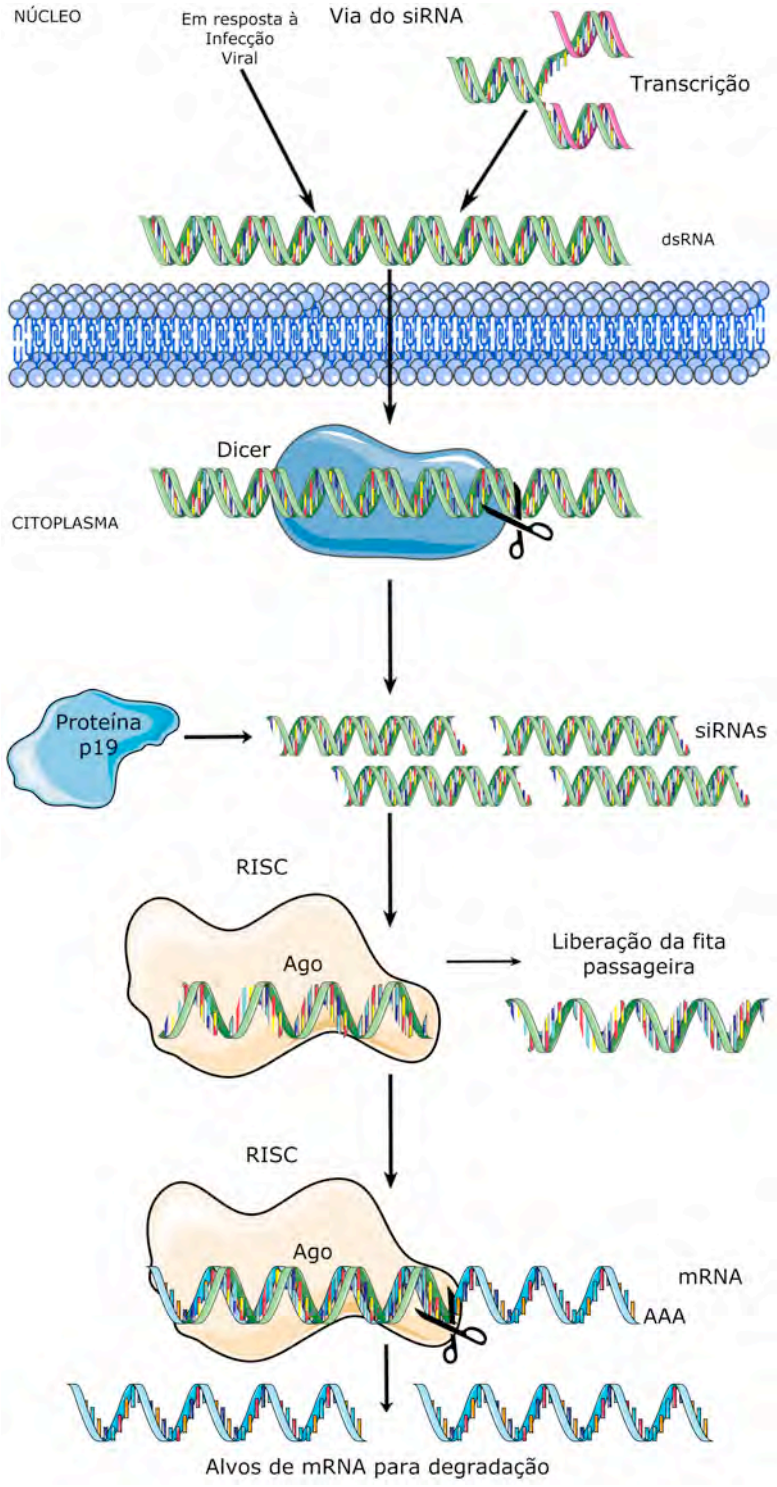

Figura 4. Representação da via do RNA de interferência para o siRNA. A proteína p19 do *tombusvirus*, que realiza o impedimento da ligação do complexo RISC, também esta representada na figura (baseado em JINEK & DOUDNA, 2009).

"While the biological properties of deoxypentose nucleic acid suggest a molecular structure containing great complexity, X-ray diffraction studies described here... show the basic molecular configuration has great simplicity."

Rosalind Franklin (1920-1958)

1.2 ESTRUTURA DO SIRNA

Os RNAs, incluídos os siRNAs, são polímeros sintetizados a partir de quatro diferentes tipos de nucleotídeos, cada um formado por três partes: uma base nitrogenada, um carboidrato e um grupamento fosfato. No caso dos RNAs, as bases nitrogenadas são a adenina (A), a guanina (G), a citosina (C) e a uracila (U), e a parte sacarídica é chamada β-D-ribose (Figura 5) (BLOOMFIELD, ET AL., 2000; JINEK & DOUDNA, 2009).

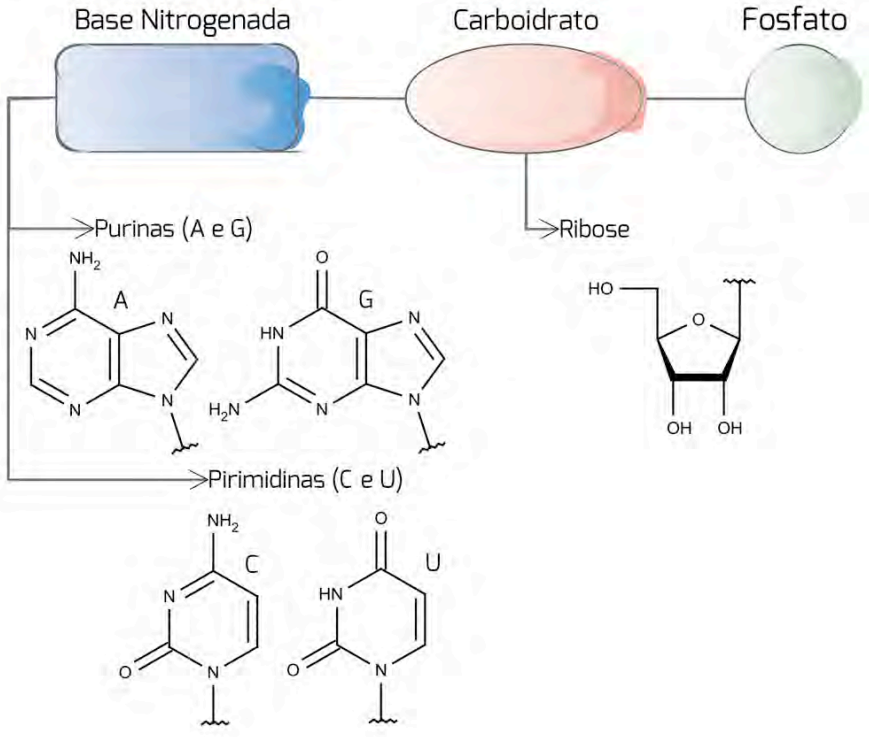

Figura 5. Representação esquemática dos nucleotídeos que compõe o siRNA e suas variações na base nitrogenada (adaptada de VERLI, 2014).

A polimerização destes nucleotídeos para compor os diferentes tipos de ácidos nucléicos se dá através da formação de uma ligação química entre os grupos fosfato, denominada ligação fosfodiéster (Figura 6). Esta ligação

estabelece uma série de ângulos torcionais, ou seja, ligações ao redor das quais pode haver rotação. Enquanto numa ligação peptídica são formados 3 ângulos torcionais (ω, ψ, ϕ), na ligação fosfodiéster encontramos os ângulos α, β, γ (na região 5'), δ (entre os átomos 3' e 4' da pentose), ε e ζ (na porção 3'). Há, ainda, o ângulo χ, formado entre o carbono 1' da pentose e a base nitrogenada que representa a ligação glicosídica entre a base e o açúcar. (Figura 6) (BLOOMFIELD, ET AL., 2000). Observa-se, assim, que os grupos fosfato agregam grande flexibilidade às moléculas de ácidos nucléicos. Ainda em analogia à estrutura de proteínas, a porção de ácidos nucléicos que não

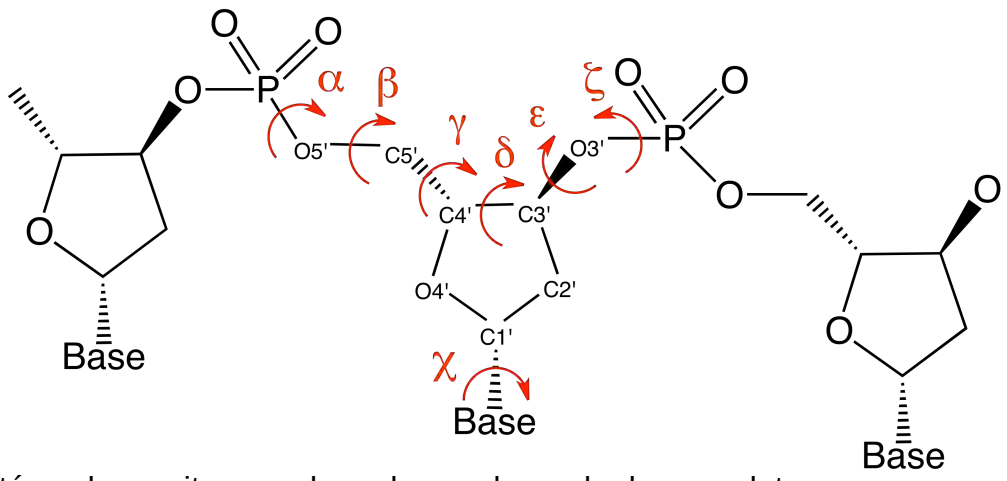

contém a base nitrogenada pode ser chamada de esqueleto.

Figura 6. Os sete ângulos torcionais que especificam a conformação de cada nucleotídeo na cadeia do siRNA. O carboidrato ligado ao grupamento fosfato é caracterizado por seis ângulos torcionais. A orientação da base em relação ao carboidrato é especificada pela ligação glicosídica, um único ângulo torcional (adaptada de VERLI, 2014).

Contudo, ângulos torcionais não são a única forma de descrever estas moléculas. Ao estabelecerem o pareamento entre as fitas, os ácidos nucléicos dupla-hélice definem uma série de parâmetros geométricos importantes para a caracterização estrutural e conformacional destas biomoléculas (Figura 7) (BLOOMFIELD, ET AL., 2000; VERLI, 2014). Estes parâmetros são definidos a partir dos movimentos translacionais ou rotacionais que cada base ou pares de bases podem sofrer dentro da região pareada.

Considerando um espaço cartesiano definido pelos eixos x, y e z (Figura 7), os parâmetros geométricos translacionais de bases em uma dupla fita de

siRNA envolvem 1) o deslocamento do par de bases ao longo do eixo x ou do eixo y, 2) o deslocamento de uma base em relação à outra, seja como uma distensão ao longo do eixo y (*stretch*), 3) seja como cisalhamento ao longo do eixo x (*shear*), um 4) escalonamento acima ou abaixo do plano xy (*stagger*), ou ainda uma elevação ao longo do eixo z (*rise*), seja como um 5) deslizamento ao longo do eixo y (*slide*) ou 6) ao longo do eixo x (*shift*).

Os parâmetros rotacionais de bases ou pares de bases entre si produzem diferentes tipos de inclinação definidas como *tip*, *inclination*, *roll* e *tilt*. Alguns pares de bases podem ainda ser classificados como torcidos, os quais são definidos como *twist, propeller* ou *buckle*, e abertos definidos como *opening* (BLOOMFIELD, ET AL., 2000; VERLI, 2014).

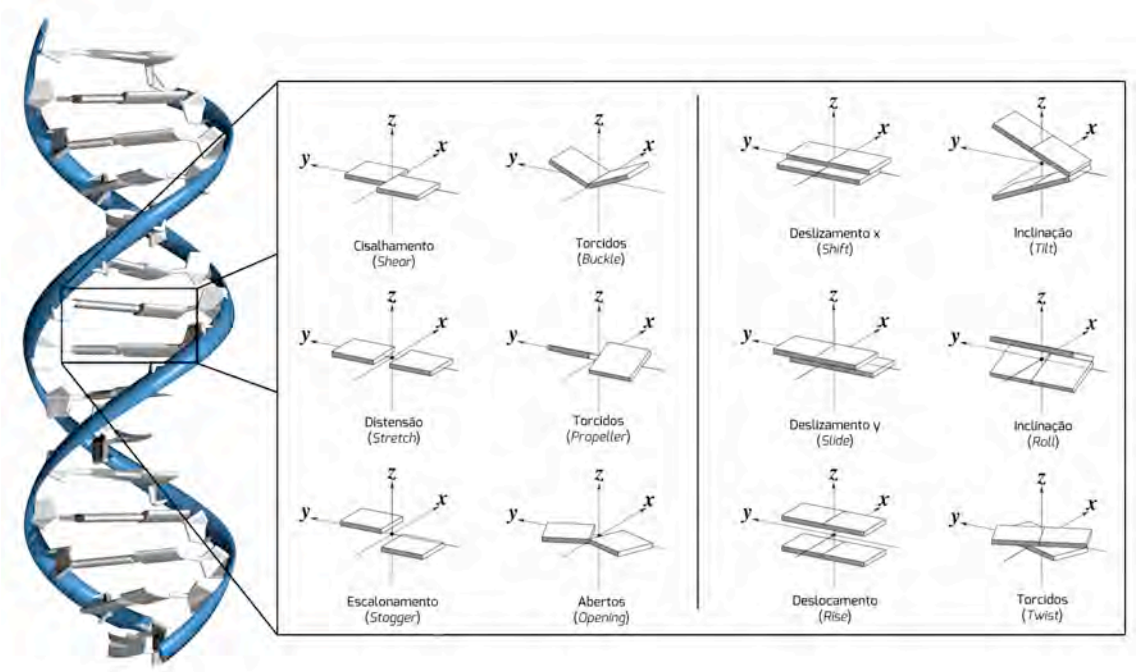

Figura 7. Parâmetros geométricos empregados como descritores da geometria dos siRNAs (LU ET AL., 2003; VERLI, 2014).

Os siRNAs, como demonstrado anteriormente, são pequenos fragmentos de 21 a 25 nucleotídeos provenientes de um processamento realizado pela Dicer, a partir de um longo RNA de dupla fita (GROßHANS & FILIPOWICZ, 2008; JINEK & DOUDNA, 2009). Por serem ácidos nucleicos, essas moléculas possuem como segmentos terminais o grupamento 5'- fosfato e a 3'-hidroxila. Na extremidade 3' existem nucleotídeos salientes e não pareados, que recebem o nome de extremidades coesivas (Figura 8) (YE, ET AL., 2003).

Assim, os siRNAs possuem um duplex de 19 a 23 pares de bases, geralmente com 2 nucleotídeos salientes na extremidade 3’ (Figura 8). Existem proteínas virais (Figura 4) com a capacidade de reconhecimento e ligação ao núcleo central dos siRNAs. Como exemplo, a proteína p19 que possui a capacidade de ligação específica com os 19 pares de bases centrais dos siRNAs, não reconhecendo as extremidades coesivas.

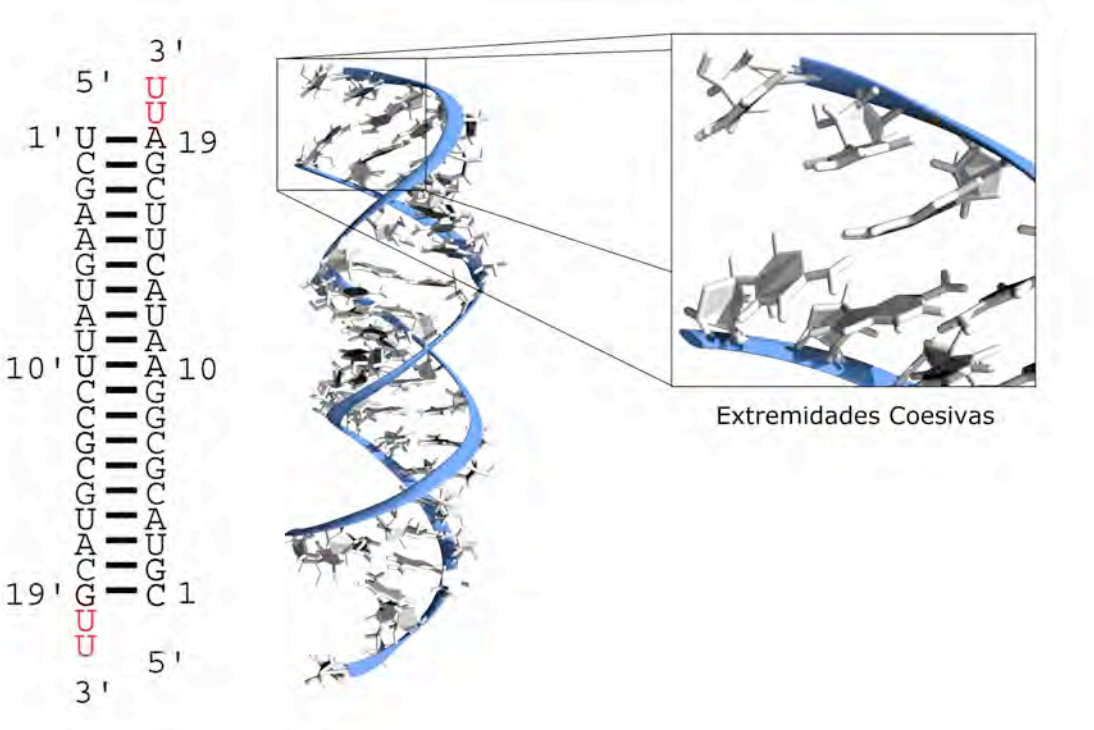

Figura 8. Estrutura primária e tridimensional de um siRNA, em ambas representações as extremidades coesivas estão destacadas.

1.3 O papel da Dinâmica Molecular na Caracterização Conformacional de Ácidos Nucleicos

A elucidação das bases moleculares para fenômenos biológicos passa pela caracterização de suas estruturas tridimensionais com resolução atômica. Infelizmente, o emprego de métodos como a cristalografia de raios-X na determinação das estruturas de ácidos nucleicos implica tanto em custos elevados quanto em dificuldades de descrever adequadamente a flexibilidade molecular (SIM, ET AL., 2012). Métodos alternativos, como aqueles baseados no uso de computadores (também chamados de estudos *in silico*), oferecem abordagens complementares, capazes de transitar tanto por informações na forma de sequências de nucleotídeos quanto na forma de estruturas tridimensionais (LAING & SCHLICK, 2010; LAING & SCHLICK, 2011).

O conjunto de métodos *in silico* que lidam com moléculas com resolução atômica podem também ser chamados de bioinformática estrutural, oferecendo inclusive a possibilidade de descrever a flexibilidade molecular. Esta área foca na representação, no armazenamento, na recuperação, na análise e na visualização estrutural, oferecendo abordagens para a manipulação de informação sobre macromoléculas biológicas e a busca pelas bases estruturais para fenômenos biológicos, patológicos e terapêuticos (BOURNE & WEISSIG, 2003). Uma das técnicas em bioinformática estrutural mais comumente empregadas neste sentido é a dinâmica molecular (DM).

A DM descreve a variação do comportamento molecular em função do tempo. Segundo a IUPAC (*International Union of Pure and Applied Chemistry*), a DM consiste em um procedimento de simulação que calcula o movimento dos átomos segundo a equação do movimento de Newton. Por ser baseada na física de Newton, a DM faz parte dos métodos chamados de mecânica molecular (ou mecânica clássica), em oposição aos métodos de física quântica denominados mecânica quântica (VERLI, 2014).

A descrição conformacional oferecida pela DM baseia-se na integração da 2ª Lei de Newton, onde *Fxi* é a força aplicada ao átomo *i* na posição *x*, *t* é o tempo, *v* é a velocidade e a_i a aceleração do átomo *i* (LEACH, 2001). Aplica-se essa equação a todos os átomos do sistema, sucessivamente, e assim obtém-se uma sequência de diferentes posições dos átomos em função do tempo, ou seja, uma trajetória de movimento das moléculas em estudo (LEACH, 2001).

Esse conjunto de coordenadas pode representar, por exemplo, as mudanças conformacionais de uma molécula de ácido nucleico em solução aquosa (Figura 9).

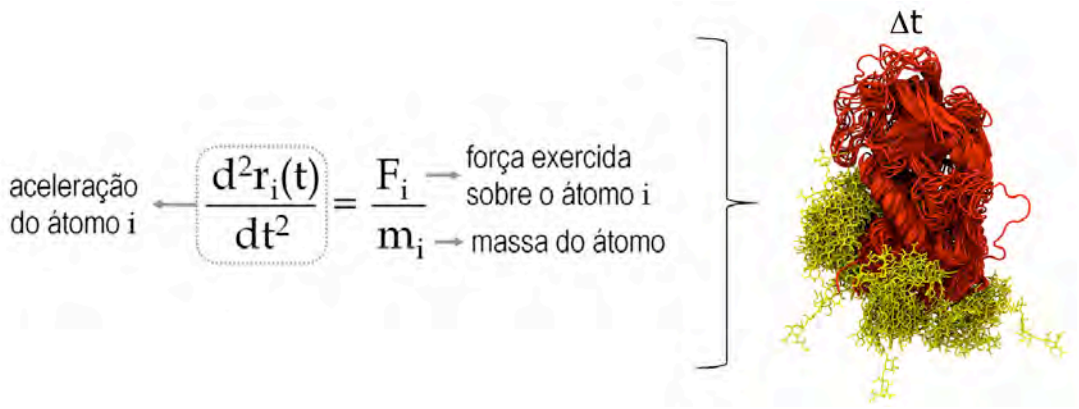

Figura 9. Representação da equação de movimento de Newton utilizada para a descrição conformacional oferecida na DM. A proteína AT-glicosilada é apresentada como resultado da aplicação desta equação sobre seus sistema.

Quando se inicia um estudo por DM podemos utilizar estruturas de partida de diferentes origens, tais como aquelas derivadas do método de cristalografia de raios-X ou RMN, disponíveis no *Protein Data Bank* (www.rcsb.org). Em seguida, precisamos incluir as moléculas do solvente em quantidade representativa da concentração dos solutos em estudo nos sistemas de interesse (como no citoplasma, por exemplo). Esta adição cria, contudo, interações soluto-solvente até então inexistentes nas estruturas determinadas experimentalmente. Tais interações são acomodadas através de um cálculo denominado minimização de energia, que reorienta as posições atômicas buscando reduzir a energia global do sistema e, assim, em conformações e orientações moleculares mais estáveis para o sistema em estudo (LEACH, 2001; VERLI, 2014).

Nas simulações por DM, alguns aspectos metodológicos importantes devem ser considerados, dentre os quais destacam-se:

- *Condições periódicas de contorno:* Permitem que a caixa de simulação (espaço tridimensional que contém as moléculas em estudo) seja replicada em todas as suas dimensões, de forma periódica. Estas réplicas são idênticas à caixa construída, de forma que um movimento molecular em uma será idêntico ao

movimento da mesma molécula na outra (Figura 10 A). Uma das principais consequências desta abordagem é que as faces da caixa nunca entram em contato com o vácuo, criando um contínuo mais próximo do ambiente de interesse (VERLI, 2014).

- *Equilibração: :* É a primeira parte da simulação, necessário para a eliminação de variações ou comportamentos moleculares aleatórios e não representativos dos fenômenos de interesse. Assim, o tempo de simulação deve ser suficientemente longo para que as propriedades estejam adequadamente equilibradas e possam, em seguida, ser coletadas (LEACH, 2001; VERLI, 2014).
- *Amostragem:* É o nome dado para o volume de informação conformacional obtido em uma determinada simulação por DM, estando diretamente relacionada ao tempo de simulação. Deve ser longa o bastante para descrever os fenômenos de interesse o que, na maioria dos sistemas proteicos, é ainda extremamente difícil de ser alcançado. Para moléculas flexíveis como ácidos nucleicos e carboidratos e fluidos como membranas, contudo, uma amostragem adequada é alcançada com relativa facilidade, em torno de centenas de nanossegundos (VERLI, 2014).
- *Tempo de Integração:* O cálculo de DM é dividido em pequenos passos, na escala de fentossegundos (fs). A sucessão destes passos resultará na trajetória. O tamanho dessas "janelas temporais" é conhecido como tempo de integração. Quanto maior este valor, menos passos de cálculos serão necessários para descrever um fenômeno e, portanto, menor será o custo computacional. Da mesma forma, quanto menor este valor, mais passos serão necessários e maior será o custo computacional. Contudo, o uso de tempos de integração muito elevados podem provocar instabilidades, de forma que normalmente são utilizados valores intermediários, de 1 a 4 fs (Figura 10 B) (LEACH, 2001; VERLI, 2014).

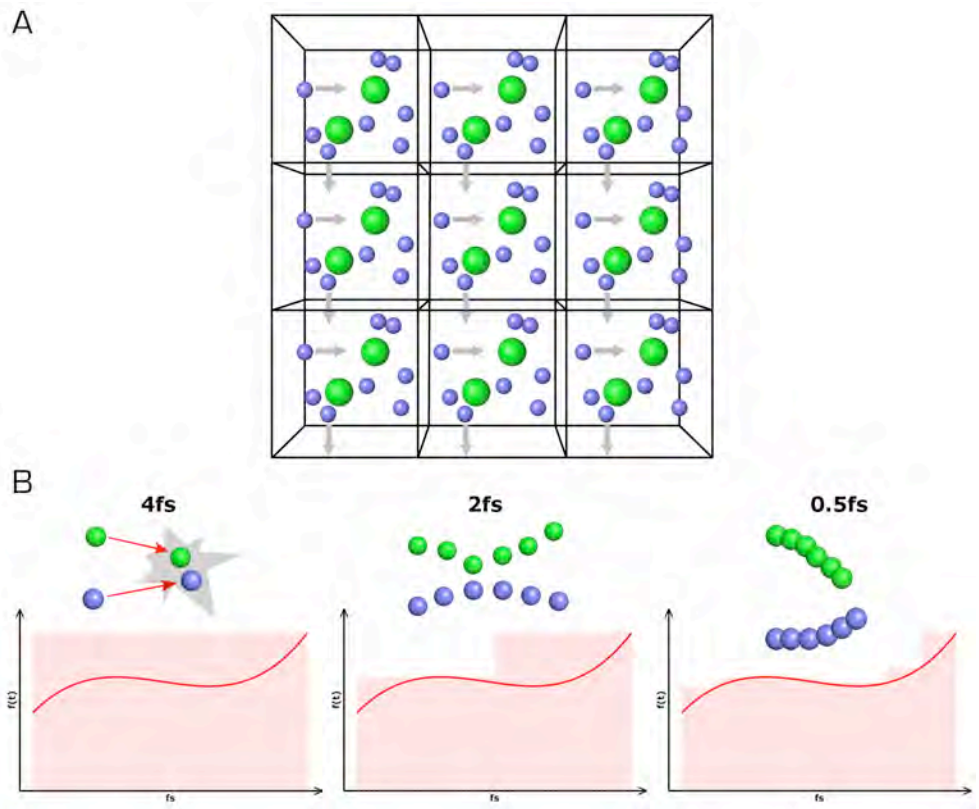

Figura 10. (A) Representação das condições periódicas de contorno em uma simulação de DM. (B) Representação do efeito de diferentes tempos de integração na amostragem de DM (adaptada de VERLI, 2014).

Ao introduzir explicitamente propriedades como flexibilidade e temperatura nos estudos dos sistemas moleculares de interesse, a DM aproxima os modelos estruturais de biomoléculas da realidade biológica (VERLI, 2014). Contudo, algumas características desta técnica restringem sua aplicação a alguns tipos de problemas moleculares. Por exemplo, cálculos baseados em mecânica molecular não descrevem os elétrons, limitando sua contribuição em estudos de fenômenos como reações enzimáticas e processos oxidativos. Como mencionado acima, principalmente no caso de sistemas contendo proteínas, é ainda extremamente difícil a obtenção de amostragem compatível com dados experimentais (há ainda uma diferença de ordens de grandeza entre a escala de tempo alcançável computacionalmente e aquela de alguns processos biológicos).

1.4 Campos de Força

Como visto anteriormente, a resolução da equação de movimento de Newton em diversos passos de integração nos permite descrever o movimento dos átomos nas moléculas em estudo. Contudo, os átomos do sistema não estão isolados, mas ligados a outros átomos formando moléculas que , por sua vez, interagem com outras moléculas. A referida equação não descreve essas interações, papel realizado por um conjunto de equações denominados de campo de força (LEACH, 2001).

O campo de forca pode ser definido como um conjunto de funções e parametrizações usados em cálculos de mecânica molecular (DE SANT'ANNA, 2002). Estas funções são equações dedicadas a reproduzir certos aspectos do comportamento molecular, como o estiramento de ligações químicas, a deformação de um ângulo de ligação ou a torção de um diedro (Figura 11) (LEACH, 2001). Interações não-covalentes, como interações de van der Waals, podem também ser calculadas, através do potencial de Lennard-Jones, assim como as interações eletrostáticas podem ser avaliadas por um termo de Coulomb (Figura 11).

Existem diferentes níveis de simplificação na descrição atômica das moléculas (Figuras 12 e 13), originando diferentes classes de campos de força. Um deles permite descrever todos os átomos do sistema (*all atom*), implicando em maior custo computacional e, consequentemente, dificultando o estudo de grandes sistemas moleculares. Pertencem a esta classe os campos de força AMBER (LINDORFF-LARSEN ET AL., 2010) e CHARMM (MACKERELL & BANAVALI, 2000; FOLOPPE & MACKERELL, 2000). Outra classe de campo de força é denominada de átomo unido (*united atom*), na qual o átomo de hidrogênio, mais abundante em sistemas biológicos, é simplificado. Neste caso, os átomos de hidrogênios ligados aos átomos carbonos apolares são unidos a este elemento, dando origem a um pseudoátomo CH, CH_2 ou CH_3. Os átomos de hidrogênio presentes nos carbonos aromáticos, mais polares, estão descritos explicitamente. O GROMOS96 (OOSTENBRINK ET AL., 2004; SOARES ET AL., 2005) é um exemplo dessa classe. O terceiro tipo de simplificação, denominado *coarse-grained* (CG), consiste na agregação de vários átomos em uma única partícula. O aminoácido alanina, por exemplo, é considerado como uma única partícula. Esta abordagem perde a resolução atômica e, como consequência,

propriedades como conteúdo de estrutura secundária deixam de ser descritas com precisão. Entretanto, por ser muito rápido, o CG pode acessar movimentos lentos e complexos, como a fusão de vesículas, lamelas ou o a dinâmica entre domínios proteicos.

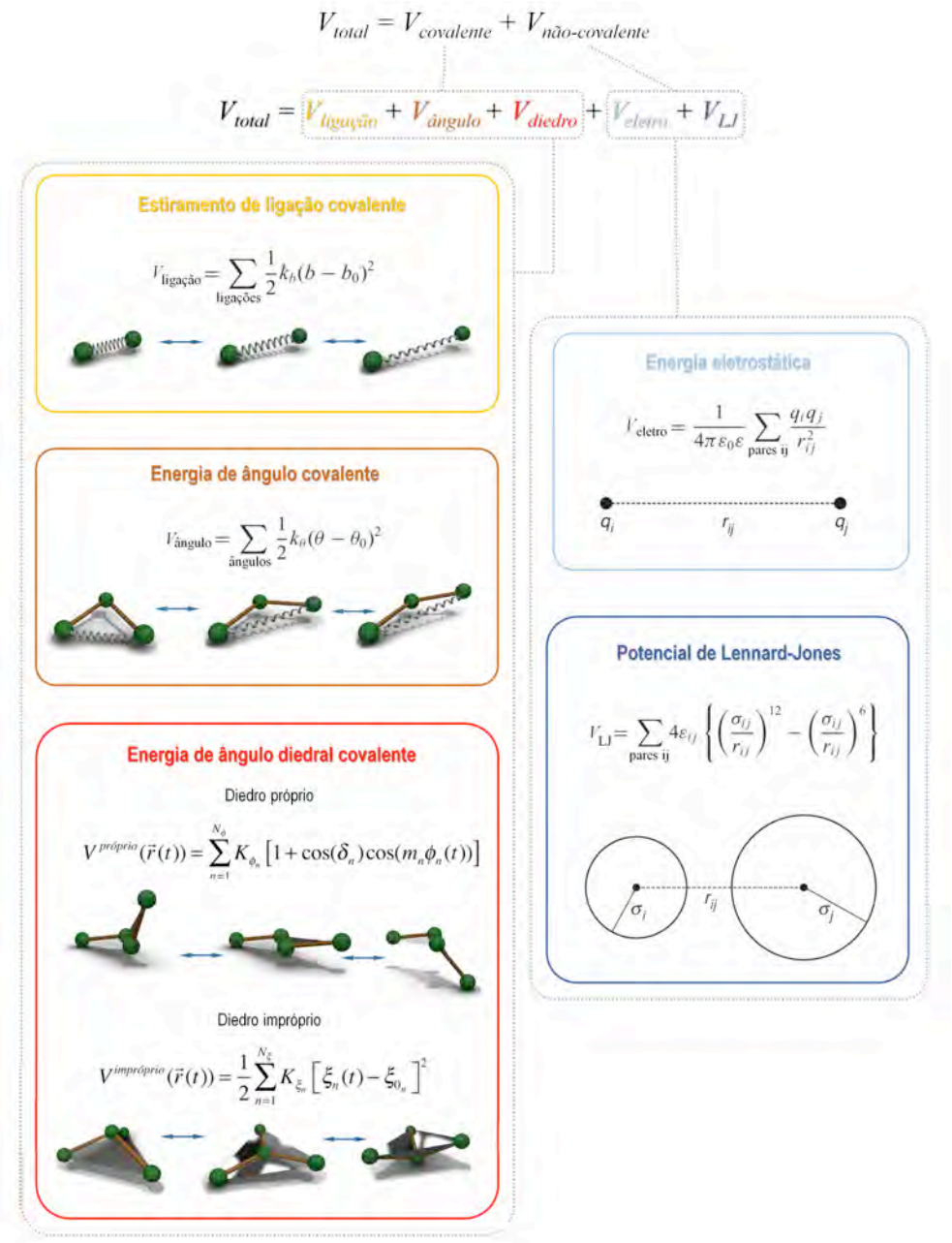

Figura 11. Representação dos termos que compõem os campos de força empregados em dinâmica molecular (adaptado de SERDYUK ET AL., 2007).

O emprego de simulações por DM e cálculos baseados em campos de força a moléculas de DNA é relativamente antigo na literatura (VAN GUNSTEREN., 1987; VON KITZING., 1992), principalmente empregando os campos

de força AMBER e CHARMM (VON KITZING., 1992; XIA ET AL., 2009). O GROMOS, contudo, a despeito de seu menor custo computacional, se demonstrou pouco adequado a descrição deste tipo de ácido nucleico (RICCI ET AL., 2010), apontando para a necessidade de uma reparametrização. Com relação a siRNAs, a despeito de diversas estruturas cristalográficas já determinadas[1], somente 2 estudos por DM foram descritos (XIA ET AL., 2009; WANG ET AL., 2010), empregando o campo de força CHARMM.

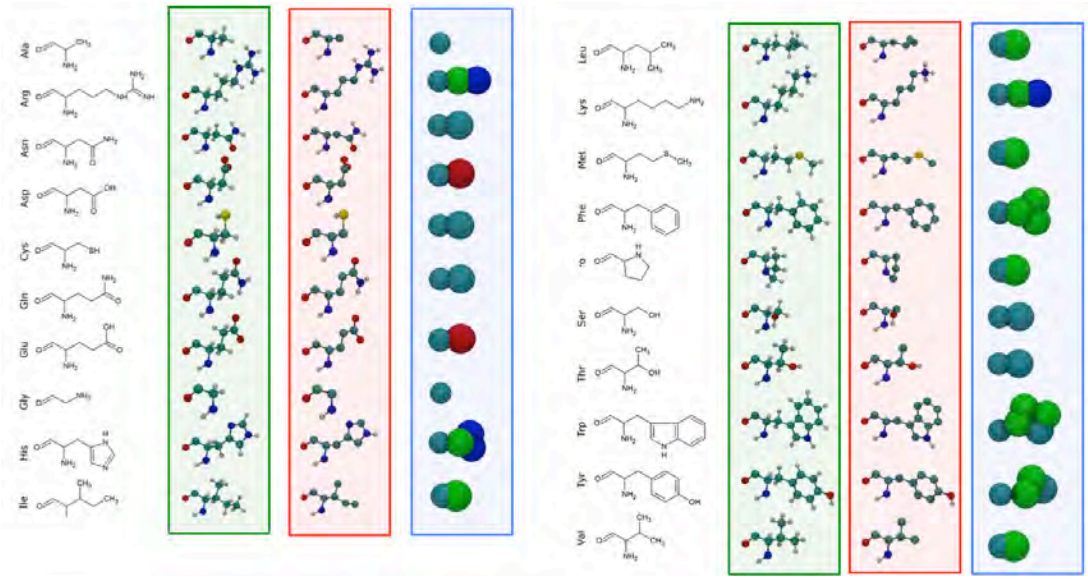

Figura 12. Representação dos aminoácidos em um campo de força descrevendo todos os átomos (verde), átomo unido (vermelho) e *coarse-grained* (azul) (adaptada de VERLI, 2014).

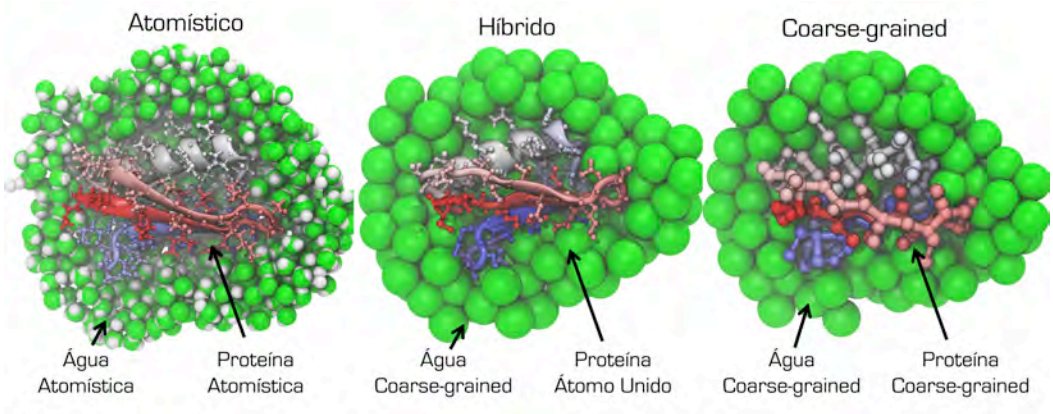

Figura 13. Representação de sistemas construídos com diferentes tipos campos de força. Esta demonstrado também a utilização de dois tipos campos de força em uma mesmo sistema, chamado sistema híbrido.

[1] PDB IDs: 1R9F, 1RPU, 1SI2, 1SI3, 1W9H, 1Z25, 1Z26, 1ZBH, 1ZBU, 2BGG, 2F8S, 2F8T, 2KWG, 2W42, 2YHA, 2YHB, 2ZIO, 2CZ3, 3P4A, 3P4B, 3P4C, 3P4D, 3S7C, 3S8U e 3VEM.

2. OBJETIVOS

Apesar da importância biológica dos siRNAs, não há estudos comparando a forma como os diferentes campos de força descrevem esses pequenos e flexíveis RNAs de cadeia dupla, o que prejudica as aplicações mais amplas de simulações moleculares para avaliar sua dinâmica e papéis funcionais. Neste contexto, o presente trabalho tem como objetivo, comparar os campos de força AMBER, CHARMM e GROMOS na conformação e descrição estrutural de siRNAs livres e complexados à proteína p19, bem como uma sequência de DNA equivalente como controle. Para tal, as seguintes metas foram traçadas:

- Verificar diferenças entre os campos de forças *all-atom* (AMBER e CHARMM) e *united-atom* (GROMOS) na descrição de siRNAs;

- Avaliar a dependência de propriedades conformacionais e estruturais dos siRNAs nos diferentes campos de força;

- Verificar o papel da proteína na manutenção da estrutura do siRNA.

3. MÉTODOS

O protocolo geral de simulação foi baseado em procedimentos previamente descritos para ácidos nucleicos (conforme esquematizado na Figura 14) (HASHEM & AUFFINGER, 2009; RICCI ET AL., 2010). Foram realizadas simulações por DM para o siRNA, bem como simulações de uma molécula de DNA, as quais foram utilizadas como controle.

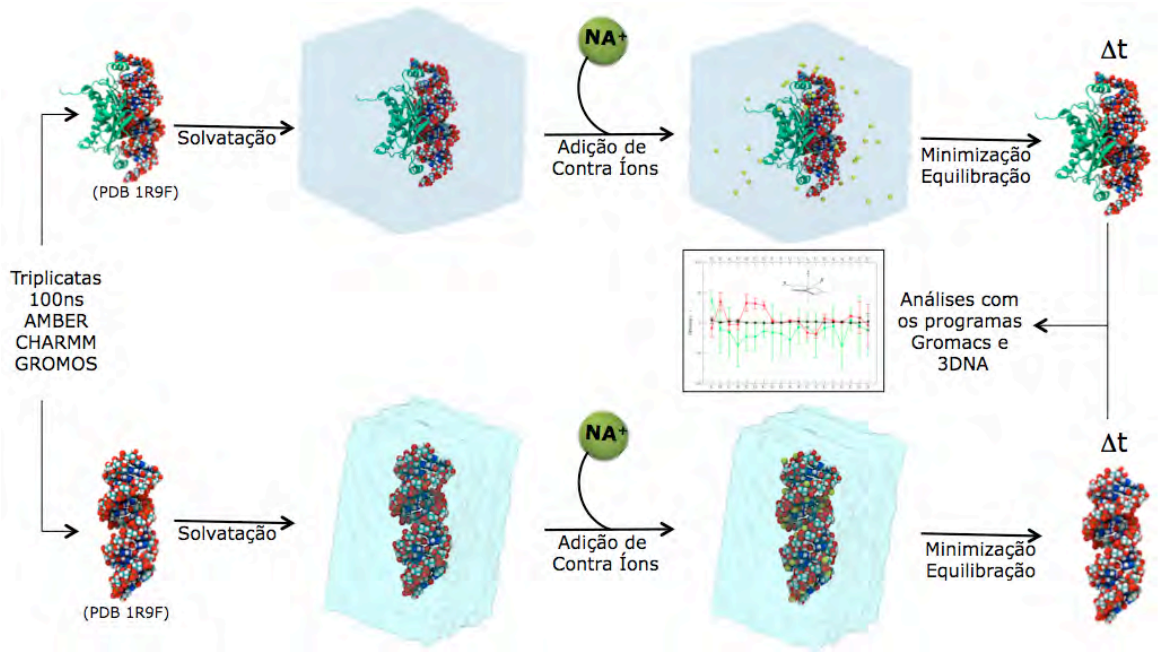

Figura 14. Representação da metodologia utilizada para o estudo conformacional e estrutural dos siRNAs. Sistemas do siRNA complexado a proteína p19 na parte superior e siRNA livre na parte inferior da imagem.

3.1 PROGRAMAS UTILIZADOS

Os principais programas e protocolos e em quais partes da presente dissertação eles foram empregados encontram-se abaixo, na Tabela 1:

Tabela 1. Descrição dos programas e/ou parâmetros empregados para a realização de diversas tarefas.

Finalidade	Programas e/ou Parâmetros
Visualização e Manipulação de Estruturas	VMD 1.9.1 (HUMPHREY ET AL., 1996) PyMol (SCHRÖDINGER, LLC) MOLDEN (SCHAFTENAAR & NOORDIK, 2000)
Dinâmica Molecular	GROMACS 4.5.1 (PRONK ET AL., 2013) GROMOS 53a6 (OOSTENBRINK ET AL., 2004; SOARES ET AL., 2005) AMBER99SB-ILDN (LINDORFF-LARSEN, ET AL., 2010) CHARMM27 (MACKERELL & BANAVALI, 2000; FOLOPPE & MACKERELL, 2000)
Análise dos Resultados	GROMACS 4.5.1 (PRONK ET AL., 2013) 3DNA (LU ET AL., 2008)

3.2 Preparação do Sistema

O siRNA estudado possui sua estrutura cristalizada, depositada no banco de dados do PDB, sob código 1R9F (YE ET AL., 2003), complexado à proteína p19 (Figura 15). Essa proteína é um homodímero que interage com os 19 pares de bases centrais do siRNA. As extremidades coesivas do siRNA não estão presentes nesse complexo e, assim, foram incluídas com o programa 3DNA (LU ET AL., 2008). Paralelamente, uma molécula de DNA controle foi construída também pelo programa 3DNA (LU ET AL., 2008), com o mesmo número de nucleotídeos dos siRNAs estudados e na forma de uma dupla-hélice de B-DNA genérico (*Twist* = 36.0 º, *Rise* = 3.375 Å) (Figura 15). Foram assim construídos três sistemas:

i) siRNA livre;

ii) siRNA complexado a proteína p19;

iii) B-DNA dupla-fita com o mesmo número de pares de bases.

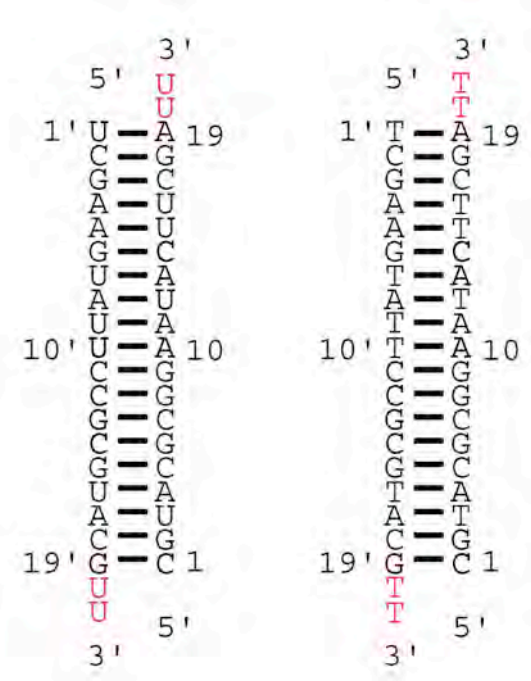

Figura 15. Representação das estruturas de RNA e DNA, respectivamente, utilizadas para o estudo conformacional no presente trabalho.

Todos estes sistemas foram simulados em triplicata, nos campos de força AMBER99SB-ILDN (LINDORFF-LARSEN, ET AL., 2010), CHARMM27 (MACKERELL & BANAVALI, 2000; FOLOPPE & MACKERELL, 2000) e GROMOS 53a6

(OOSTENBRINK ET AL., 2004; SOARES ET AL., 2005), totalizando 27 simulações por DM.

3.3 Dinâmica Molecular

Para o estudo por DM, o pacote de simulações do GROMACS 4.5.1 (PRONK, ET AL., 2013) foi utilizado em conjunto com os campos de força GROMOS 53A6 (OOSTENBRINK ET AL., 2004; SOARES ET AL., 2005), AMBER99SB-ILDN (LINDORFF-LARSEN ET AL., 2010) e CHARMM27 (MACKERELL & BANAVALI, 2000; FOLOPPE & MACKERELL, 2000). Os sistemas foram solvatados a partir dos modelos de água TIP3P (AMBER e CHARMM) (MAHONEY & JORGENSEN, 2000) e SPC (GROMOS) (BERENDSEN ET AL., 1987) em caixas octaédricas com a presença de condições periódicas de contorno. Adição de contra íons de Na^+ foi necessária para a neutralização do sistema, já que os ácidos nucleicos possuem alta carga negativa devido à presença do grupamento fosfato. As minimizações de energia foram conduzidas no algoritmo *Steepest Descent*, enquanto que o tratamento eletrostático empregou o método PME (DARDEN ET AL., 1993). Os comprimentos das ligações covalentes foram fixados pelo método de Lincs (HESS ET AL., 1997), permitindo o emprego de um tempo de integração de 2 fs.

As simulações por DM podem ser divididas em duas fases: equilibração e produção. Na equilibração a biomolécula de estudo teve uma restrição de posição imposta visando à obtenção de uma acomodação lenta e gradual da orientação dos outros componentes do sistema, como, solvente e contra íons. Assim duas simulações, uma de 0,0001 μs e outra de 0,001 μs, foram realizadas para cada sistema, com uma constante de força 1.000 kJ/mol para os átomos pesados. A primeira dessas foi realizada com volume e temperatura constantes (NVT), enquanto as posteriores foram realizadas com pressão e temperatura constantes (NPT). Na fase de produção (também NPT), na qual ocorre a coleta dos resultados, todo o sistema (siRNA, siRNA/proteína e DNA) tem seu movimento liberado da restrição imposta, possibilitando a avaliação da dinâmica. Nesta fase, o tempo de cada simulação foi de 0,1 μs. Na simulação de NVT, o acoplamento de temperatura foi realizado com o termostato V-rescale (BUSSI ET AL., 2007), enquanto que na NPT o barostato Parrinelo-Rahman (PARRINELO & RAHMAN, 1981; NOSE & KLEIN, 1983) foi utilizado.

3.4 Análise dos Resultados

As trajetórias da simulação foram analisadas com o pacote de programas GROMACS, a fim de calcular a evolução temporal do desvio quadrático médio (RMSD) e a evolução temporal das ligações de hidrogênio intramoleculares. As ligações de hidrogênio foram definidas usando um critério geométrico (distância entre o doador e aceptor de menos de 0,35 nm e ângulo receptor-doador-hidrogênio inferior a 30 °) (Figura 16).

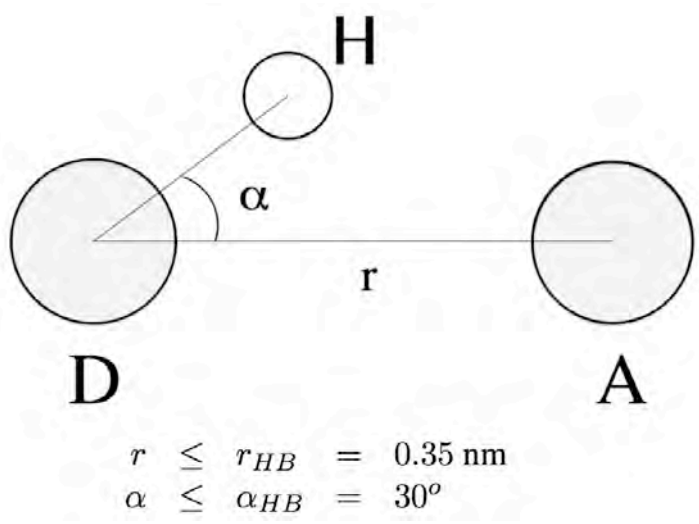

Figura 16. Critério geométrico adotado para a existência de ligações intramoleculares de hidrogênio. D = Doador, A = Aceptor (VAN DER SPOEL ET AL., 2010).

Para a análise de parâmetros específicos dos nucleotídeos foi necessária a utilização de programas diferentes daqueles conhecidos para a análise de proteína e de carboidratos. Como demonstrado anteriormente, o estudo de ácidos nucleicos envolve a análise de diferentes parâmetros (descritores geométricos e ângulos torcionais), para isso foi empregado o programa 3DNA (LU ET AL., 2008). Esse pacote permite a análise de praticamente todos os parâmetros para o estudo conformacional e estrutural de uma molécula de ácido nucleico.

4. RESULTADOS

4.1 PREÂMBULO

Os resultados obtidos durante a realização da presente dissertação serão apresentados sob a forma de um manuscrito a ser submetido à publicação. A seguir, será apresentado o resumo e a íntegra do referido trabalho, seguindo os padrões[2] do periódico: *Journal of Computational Chemistry*, possível local de publicação deste trabalho.

[2] Disponíveis em <<http://onlinelibrary.wiley.com/journal/10.1002/(ISSN)1096-987X/homepage/jcc_author_guidelines.html>>

Force Fields Reliability on the Description of protein bound and unbound siRNA

Pablo Ricardo Arantes,[1] Hugo Verli,[2]

Correspondence to: Hugo Verli (E-mail: *hverli@cbiot.ufrgs.br*)

[1] *P. R. Arantes*
Biotechnology Center, Federal University of Rio Grande do Sul, Porto Alegre, RS, Brazil 91500-970
[2] *H. Verli*
Biotechnology Center, Federal University of Rio Grande do Sul, Porto Alegre, RS, Brazil 91500-970

ABSTRACT

Small interfering RNAs (siRNA) which are small fragments of double-stranded RNA, can silence the expression of specific genes at the post-transcriptional level by a pathway known as RNA interference. While such molecules have an important function, computational simulations of them are still not common in literature, and there is little information on the extent of reliability of the available force fields to deal with such small double-strand structures. The current work intends to compare AMBER, CHARMM and GROMOS force fields regarding the conformational and structural description of protein-complexed, and uncomplexed siRNAs, under molecular dynamics simulations. The obtained data point to AMBER and CHARMM as the main force fields for RNA simulation. On the other hand, GROMOS force field leads to strong distortion of nucleic acids, resulting in the complete disruption of the double strand.

Introduction

In eukaryotes, during the translation process, at least three main types of RNA are needed: messenger RNA (mRNA), transfer RNA (tRNA) and ribosomal RNA (rRNA). In addition, there are small double-stranded RNAs which are not translated into proteins.[1] Instead, those small 20-30 nucleotides long RNAs regulate the expression of genes, by binding with complementary portions of other transcript sequences, interfering with the translation process.[2] This post-transcriptional process is known as RNA interference pathway or the silencing of gene expression pathway.[1,2] The discovery of these small RNAs and their main role in the silencing of gene expression has profoundly altered the understanding of gene regulation.[3] These particular nucleic acids are called silencing RNA or interference RNA (RNAi). Originally found only in plants, they are present in many eukaryotic organisms.[2,3]

There are different classes of interference RNAs, the main ones are: microRNAs (miRNAs), RNAs associated with Piwi subfamily proteins (piRNAs) and small interfering RNAs (siRNAs).[1,4]

Small interfering RNAs are molecules derived from a long double-stranded RNA (dsRNA) in response to viral RNA replication, transcription in convergence or transposons.[1,2,4] siRNAs are small 21-25 nucleotide fragments from a processing performed by Dicer enzyme from long dsRNA.[1,4] These molecules have terminal segments, as all nucleic acids, with group 5'-phosphate and 3'-hydroxyl. At the 3 '-hydroxyl termini there are overhang segments of unpaired nucleotides, which are called cohesive ends (Figure 1).[5] Thus, duplex siRNAs have 19-23 base pairs, usually with 2 nucleotides on 3'-hydroxyl overhang terminus (Figure 1).

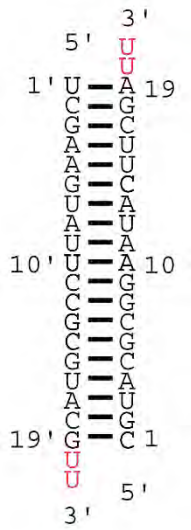

Figure 1. Representation of siRNA from PDB ID 1RF9, with cohesive ends highlighted.

The siRNA molecules may be associated with different proteins. As an example of such a combination, there are Argonaute protein and other proteins present in the RISC complex.[4] Additionally, there are viral proteins with ability to associate with siRNAs.[5] The protein p19, from *Tombusvirus*, is a siRNA activity repressor and binds specifically to such molecules.[5] The p19 protein receives this name because it is capable of specifically binding to 19 base pairs of siRNAs and does not recognize the cohesive ends.

The siRNAs constitute a very complex system and require special approaches in order to understand some experimental results or to build models at microscopic level. Molecular dynamics simulations are one of the special approaches to study these systems.[6]

Since the RNA backbone conformation is defined by six different torsion angles (Figure 2), it means that the available conformational space for nucleic acids is more complex than that available for proteins. Also, RNA has charged phosphate groups, which demand a very precise treatment. The RNA is a class of molecules that is formed by several types with different conformations. The small number of siRNAs simulations, when compared to protein, reflects these challenges.

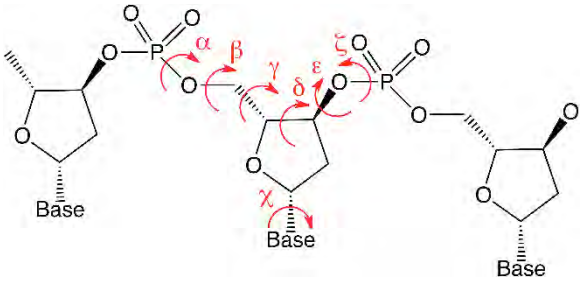

Figure 2. Backbone ($\alpha, \beta, \gamma, \delta, \varepsilon$ and ζ) and glycosidic, (χ) torsion angles.

Several force fields have been proposed to simulate RNA and DNA, among these are AMBER,[7-10] CHARMM,[11-13] OPLS,[14,15] and GROMOS[16-18]. Although many studies compared the use of these different force fields in DNA simulations,[6,19] the computational simulations for siRNAs are still rare, and there is little information on the reliability of the available force fields to deal with such small double-strands.

In this context, the current work intends to compare AMBER,[7-10] CHARMM[11-13] and GROMOS[16-18] force fields on the conformational and structural description of protein complexed and uncomplexed siRNAs, as well as a equivalent DNA sequence, under molecular dynamics simulations.

Methods

System preparation

The siRNA used in the present work has its crystal structure deposited in the PDB database under the code 1R9F (Figure 1).[5] This crystal has the p19 protein from *Tombusvirus* complexed to siRNA. p19 protein is a homodimer that interacts with the core 19 base pairs of siRNA. The cohesive ends of the siRNA are not present in the crystal. Thus, for the proper study of these biomolecules the construction of cohesive ends was carried out using 3DNA package.[20] Subsequently, the DNA molecule was constructed with 3DNA,[20] with the same

number of nucleotides as the siRNA and in the B-DNA form. For termini definitions, we performed all simulations without terminal phosphates.

From these structures, three systems were obtained: free siRNA; siRNA complexed to p19 protein and double-stranded DNA. All systems were simulated in triplicate with force fields AMBER99SB-ILDN,[10] CHARMM27,[12,13] and GROMOS53a6,[17] resulting in 27 simulations .

Molecular dynamics simulations

For molecular dynamics simulations the GROMACS 4.5.1 package[21] was used with the force fields GROMOS 53A6,[17] AMBER99SB-ILDN[10] and CHARMM27.[12,13] The systems were solvated with water models TIP3P[22] (AMBER and CHARMM) and SPC[23] (GROMOS) in octahedral boxes with the presence of periodic boundary conditions. Adding counter ions was necessary to neutralize the system, since the nucleic acids are highly negatively charged due to the presence of phosphate groups. The energy minimizations were conducted with Steepest Descent algorithm. Furthermore, for electrostatic interactions, the PME[24] method was used. The LINCS[25] algorithm was chosen to constrain covalent bond lengths and an integration step of 2 fs was applied. The barostat chosen was Parrhinello-Rahman,[26,27] with a 2.0 ps coupling constant, while the thermostats chosen were V-rescale[28] (NVT step) and Nosé-Hoover (NPT equilibration and production MD)[29,30] with a coupling constant of τ=0.5. Constant temperature of 310 K and constant pressure of 1 atm were also implemented.

First, two simulations for equilibration were performed with position restraints: a NVT and a NPT of 0.1 ns and 0.9 ns, respectively. Subsequently, 100 ns unrestrained NPT MD simulations were performed for each system, generating the production run where data was collected for the analyses.

Analyses of results

The simulation trajectories were analyzed with standard GROMACS tools in order to calculate the time evolution of the root mean square deviation (RMSD) and the time evolution of the intramolecular hydrogen bonds. The hydrogen bonds were defined using a geometrical criterion[31] (donor-acceptor distance of less than 0.35 nm and acceptor-donor-hydrogen angle of less than 30°).

The nucleotide-specific parameters[32-35] were calculated along the simulation trajectories, from 10 ps spaced snapshots, using 3DNA tools (*find-pair* and *analyze*). The local deformations of siRNA double helix were deduced from main chain torsion angles, and local base-pair-step parameters.

Results and Discussion

Global Stability

We first analyzed the effect of different force fields in the overall stability of the oligonucleotides. According to Figure 3, the structures simulated on AMBER and CHARMM force fields were more stable than those simulated on GROMOS 53a6.

For siRNA, without protein (Figure 3A), in AMBER simulations the RMSD values ranged between 0.3-0.5 nm. In CHARMM force field the values ranged between 0.5-0.7, while the structures simulated with GROMOS reached extremely high RMSD values (>1.0 nm). These high RMSD for GROMOS force field could indicate a helix deformation and denaturation of both nucleic acids during the simulations.

siRNA complexed with p19 protein (Figure 3B) shows more stable structures than the structures simulated without the protein. In both AMBER and CHARMM simulations, the RMSD values ranged between 0.2-04 nm and in the GROMOS system the RMSD values were between 0.6-0.8 nm. These data show an influence of protein on siRNA structure.

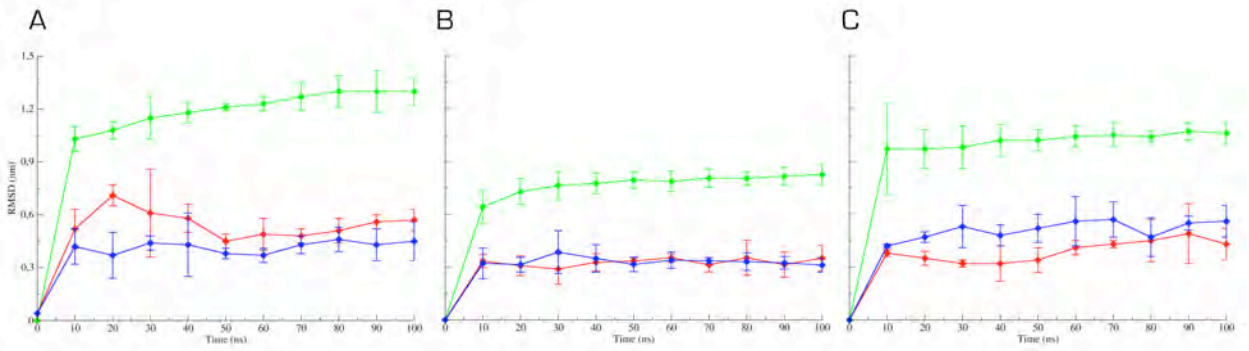

Figure 3. Root mean square deviation (RMSD), calculated along the MD trajectories for (A) siRNA, (B) siRNA complexed to protein and (C) DNA. Blue line (AMBER); red line (CHARMM); green line (GROMOS). Each point in the graphs represents the average of three simulations for each system.

For DNA structure (Figure 3C), the data demonstrate the same situation as observed for siRNA. Molecules simulated with AMBER and CHARMM force fields were more stable than structures simulated with GROMOS. This stability present on nucleic acids simulated with AMBER force field against GROMOS has been previously described in literature.[6]

Similar tendencies can be deduced from the analysis of the intramolecular hydrogen bonds, between the double-strands, depicted in Table 1. These data confirm that the structure of the oligonucleotides simulated with AMBER force field was well conserved during the simulation. In the simulations with CHARMM, the number of hydrogen bonds decreases slightly but do not affect nucleic acid structure (Figure 3). Finally, the simulations with the GROMOS force field, the number of hydrogen bonds decreased and reached roughly half of the value observed experimentally. GROMOS simulations showed a much less stable profile, with rupture of base pairs leading to a complete disruption of the double strands (Figure 3 and Table 1). These results are in agreement with a previous study,[36] which estimated the energetics of DNA base pair via potential energetics (including AMBER, CHARMM and GROMOS) and predicted that the relative H-bond strengths with different force fields obeyed the following order AMBER > CHARMM > GROMOS.

Table 1. Average of Intramolecular Hydrogen Bonds calculated from triplicates of MD trajectories

Force Field	siRNA	siRNA/Protein	DNA
AMBER	47.71 ± 1.19	48.87 ± 0.13	48.75 ± 0.87
CHARMM	35.00 ± 0.4	39.93 ± 1.26	45.57 ± 0.74
GROMOS	20.14 ± 2.53	17.28 ± 2.55	29.35 ± 4.00

[a] Experimental value expected between the double strand: 48 hydrogen bonds

Backbone Parameters

We performed the analyses of some backbone torsional angles (Figure 2) to assess the conformational stability of the backbone during the simulations and to correlate backbone alterations with helix deformations.

α and γ Angles

Among the backbone angles, the α and γ angles are particularly important for description of the backbone conformation of nucleic acids. These angles are involved in conformational changes of backbone.[37]

The α and γ angles, on AMBER force field, show values with some variation when compared to experimental or B-DNA form (Figure 4). Some nucleotides, on all three systems, present distant values from experimental data. On the other hand, there are nucleotides on all systems

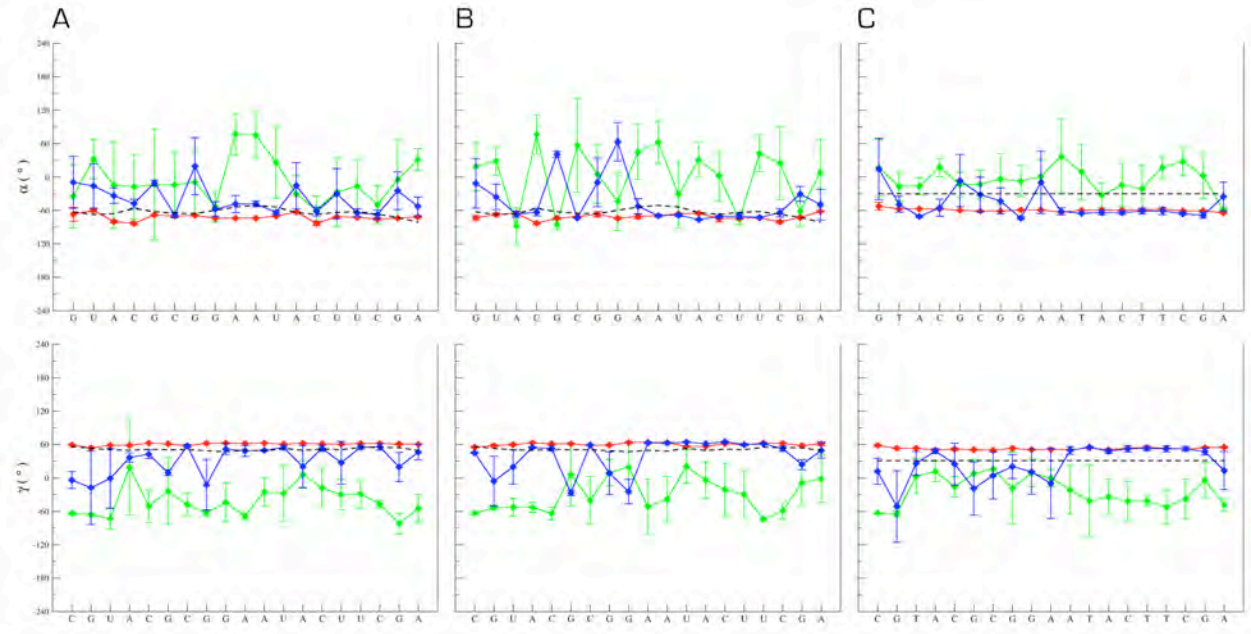

Figure 4. Values of α (top) and γ (bottom) angles for strand 1 on (A) siRNA, (B) siRNA complexed to protein and (C) DNA. Blue line (AMBER); red line (CHARMM); green line (GROMOS). Each point in the graphs represents the average of three simulations for each system. Dashed lines represent crystal data for siRNA (A and B) and values for B-DNA form on DNA (C).

with values very close to experimental data and B-DNA structure for both angles. The variations shown in these data do not affect the structure of siRNA and DNA during the simulation, according to RMSD analysis (Figure 3). These data are in agreement with a previous study with DNA,[6] that presented some fluctuation on α and γ angles for AMBER force field.

Simulations with CHARMM force field present very similar values when compared to experimental data or B-DNA form (Figure 4) for α and γ angles. Both nucleic acids simulated had stable values with low standard deviation, compared to AMBER and GROMOS. These results are in agreement with previous RMSD analysis that shows stability of the oligonucleotides simulated in CHARMM.

Nevertheless, GROMOS force field presents a much more dispersed values for α and γ angles when compared to experimental data or B-DNA form (Figure 4). siRNA and DNA simulated show high variation with high standard deviations. These data indicate that simulations on GROMOS were less restrict on α and γ angles when compared to simulations performed with AMBER and CHARMM (Figure 4). The dispersion presented on GROMOS force field, for both angles, could be related to the lack of backbone maintenance and thus the helix deformation displayed on RMSD and intramolecular hydrogen bonds analyses.

ε and ζ Angles

The ε and ζ angles are strongly related to B-DNA flexibility and the backbone conformation. Both angles are involved with phosphate geometry in the backbone of nucleic acids.

The values of ε and ζ angles on AMBER force field were very close to experimental data for siRNA (Figure 5A and 5B). These results show more stable values for both angles when compared to CHARMM and GROMOS force fields. For DNA (Figure 5C), the values of both angles are more dispersed than the siRNA on

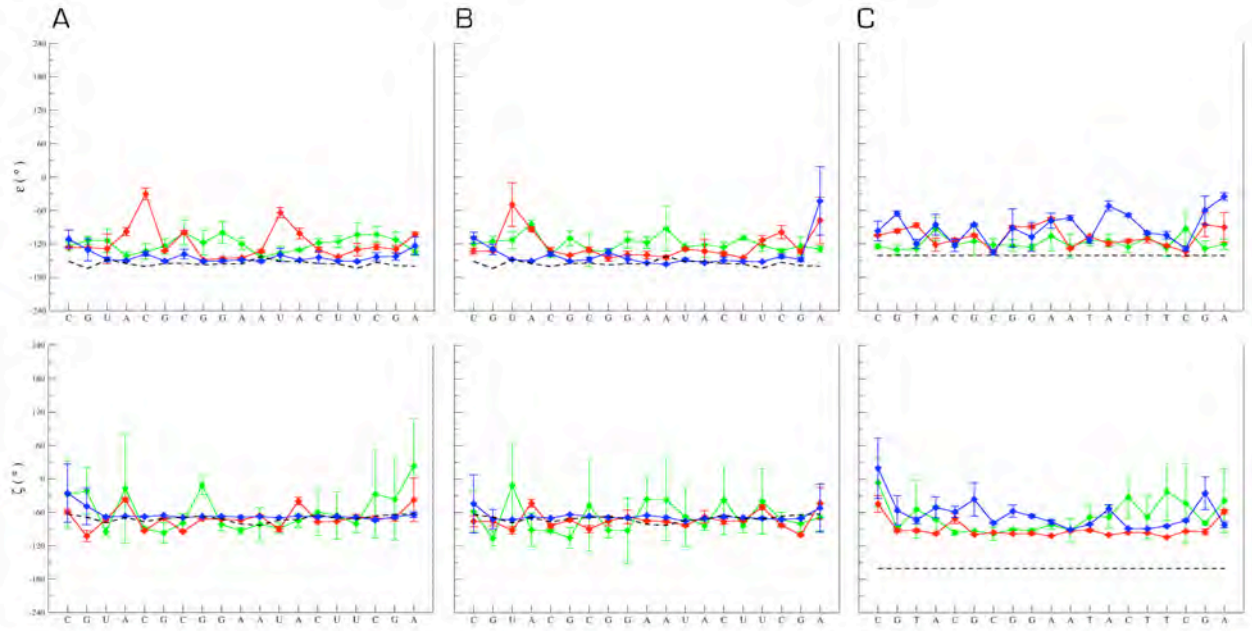

Figure 5. Values of ε (top) and ζ (bottom) angles for strand 1 on (A) siRNA, (B) siRNA complexed to protein and (C) DNA. Blue line (AMBER); red line (CHARMM); green line (GROMOS). Each point in the graphs represents the average of three simulations for each system. Dashed lines represent crystal data for siRNA (A and B) and values for B-DNA form on DNA (C).

AMBER. For ζ angle the values are more distant from B-DNA form than results observed for ε angle. On both nucleic acids the value for each nucleotide show a low standard deviation for ε and ζ angles, indicating a low variation during the simulation. Again, these values are in agreement with RMSD analysis, show that oligonucleotides simulated with AMBER force field were well conserved during the simulation.

On CHARMM force field the same situation is observed, values for both angles were close to experimental data on siRNA (Figure 5A and 5B). Several nucleotides presented distant values from experimental data when compared to AMBER force field. These results show an increased flexibility on ε and ζ angles of oligonucleotides simulated with CHARMM force field, when compared to AMBER. For DNA (Figure 5C), once more, the values of both angles were more dispersed and the results of ζ angle were distant from B-DNA form but close to the AMBER values.

The simulations of siRNA on GROMOS force field present values for ε and ζ angles close to experimental data, with a slight dispersion on some nucleotides (Figure 5A and 5B). When compared to AMBER and CHARMM force fields, there is an increased flexibility on both angles. On DNA simulations (Figure 5C), the values for ε and ζ angles are close to AMBER and CHARMM force fields. On both nucleic acids, simulated on GROMOS, the value for each nucleotide have high standard deviations, indicating a higher variation during the simulation when compared to AMBER and CHARMM force fields. In contrast to α and γ angles on GROMOS simulations, that showed much more dispersed values and were distant from experimental data, the ε and ζ angles presented values closer to AMBER and CHARMM force fields, close to experimental data as well. These results for ε and ζ angles on GROMOS simulations demonstrated a probably low influence on helix deformation displayed on RMSD and intramolecular hydrogen bonds analyses.

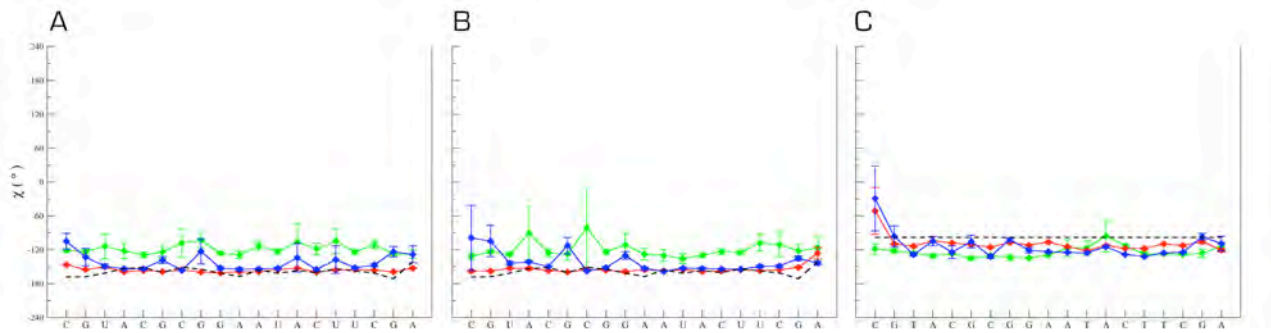

Figure 6. Values of χ angle for strand 1 on (A) siRNA, (B) siRNA complexed to protein and (C) DNA. Blue line (AMBER); red line (CHARMM); green line (GROMOS). Each point in the graphs represents the average of three simulations for each system. Dashed lines represent crystal data for siRNA (A and B) and values for B-DNA form on DNA (C).

χ Angle

In a nucleotide, each base is attached to the 1'carbon of the sugar by a glycosidic bond. The torsion angle about this bond is specified by the angle χ (Figure 2). The rotational profile of this glycosidic linkage is extremely important for backbone maintenance and base pairing on nucleic acids.

On simulations with AMBER and CHARMM force fields, all results for glycosidic linkage were close to experimental data and B-DNA form (Figure 6). The rotational profile on siRNA and DNA were very stable with low variation. The low values for standard deviation represents stability during the simulation for both force fields. These rotational profiles for χ angle are in agreement with stable base pairing show, during the MD simulations, for AMBER and CHARMM force fields on intramolecular hydrogen bonds analysis (Table 1).

On siRNA, GROMOS simulations demonstrate for χ angle, values close to experimental data, as well to AMBER and CHARMM force fields (Figure 6A and 6B). On DNA, the results are close to B-DNA form and again to AMBER and CHARM values (Figure 6C). Both nucleic acids show an increased flexibility, when compared to AMBER and CHARM force fields. The standard deviation on siRNA and DNA present a slight variation, indicating a rotational profile of glycosidic linkage, more flexible during the simulation with GROMOS force field. These results indicate that the lack of backbone maintenance and thus the helix deformation, present on GROMOS systems, are probably related to other torsional angles. The χ angle showed results close to experimental data and similar to AMBER and CHARMM force fields, leading a correct behavior for this torsional angle.

Dinucleotide Step Parameters

Among the several dinucleotide step parameters that can be used to describe the nucleic acid structure, roll, twist, and slide were selected to perform the analysis. The conformational space of any dinucleotide step is almost completely defined by these three parameters. [38]

According to Figure 7, the results of roll, twist, and slide in the AMBER and CHARMM simulations were reasonably close to the crystal data and B-DNA form. AMBER and CHARMM simulations demonstrated low variation on these parameters in agreement with previous analysis of torsional angles that showed stable results, close to the experimental data. As the

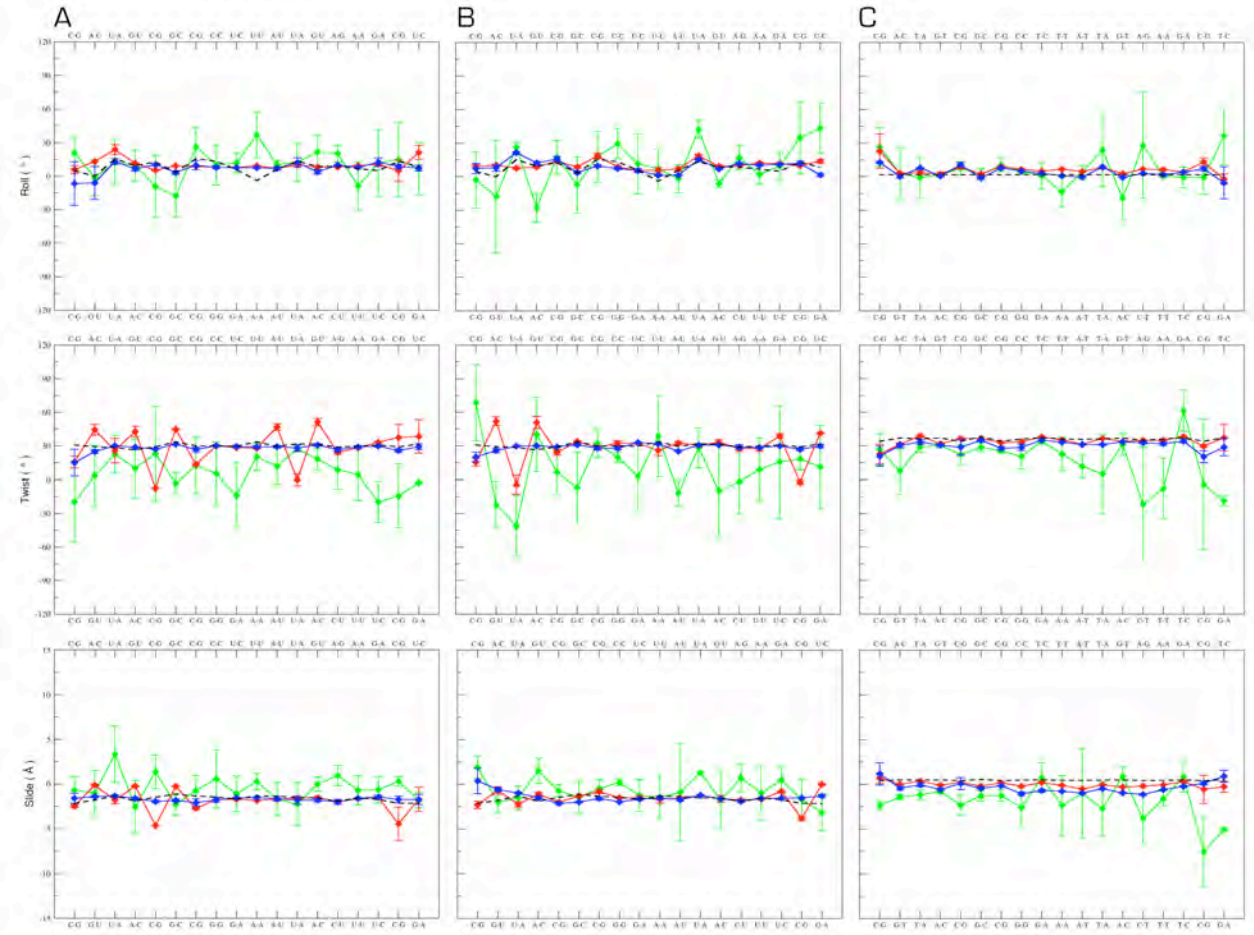

Figure 7. Values of dinucleotide step parameters: roll (top), twist (middle) and slide (bottom) on (A) siRNA, (B) siRNA complexed to protein and (C) DNA. Blue line (AMBER); red line (CHARMM); green line (GROMOS). Each point in the graphs represents the average of three simulations for each system. Dashed lines represent crystal data for siRNA (A and B) and values for B-DNA form on DNA (C).

rotational angles are responsible for definition of backbone conformation on nucleic acids, the results of dinucleotide step parameters are probably mechanical consequences of this backbone.

On GROMOS simulations, the results of roll, twist, and slide show values of bases-pair parameters which are far more distant from experimental data and B-DNA form (Figure 7), also displaying large fluctuations on standard deviation. On previous torsional angles analyses, on GROMOS force field, the α and γ angles displayed dispersed values, distant from experimental data. So, these previous results affect base-pair parameters showed on Figure 7. These analyses reinforce the helix deformation and denaturation of nucleic acids simulated on GROMOS force field simulations.

Base Pairs Parameters

Another way to describe the structure of nucleic acids can be through the base pairs parameters. These parameters are classified as translational and rotational. Shear, stretch, and stagger are types of translational parameters. On the other hand, propeller, buckle, and

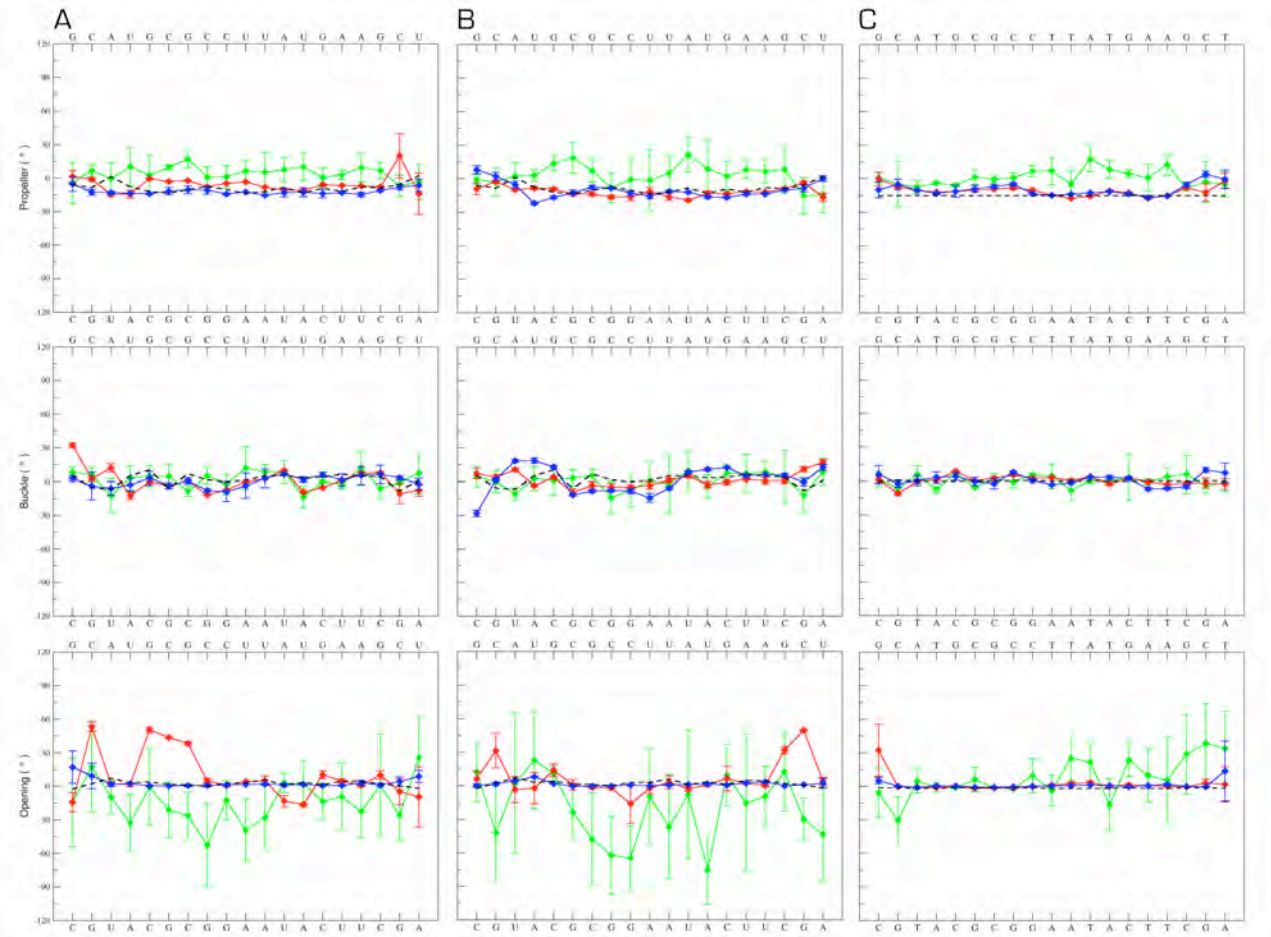

Figure 8. Values of base pairs parameters: propeller (top), buckle (middle) and opening (bottom) on (A) siRNA, (B) siRNA complexed to protein and (C) DNA. Blue line (AMBER); red line (CHARMM); green line (GROMOS). Each point in the graphs represents the average of three simulations for each system. Dashed lines represent crystal data for siRNA (A and B) and values for B-DNA form on DNA (C).

opening are types of rotational parameters. In order to perform the analyses, rotational parameters were chosen in agreement a previous study,[38] which showed that translational parameters display very little variation. So, to analyse nucleic acids we may take all translational parameters as insignificant and concentrate only on the rotational parameters.

The results of propeller, buckle, and opening parameters in the AMBER and CHARMM simulations were close to the crystal data and B-DNA form (Figure 8). AMBER and CHARMM simulations demonstrated stability on rotational parameters, in accordance with previous analyses of torsional angles that showed stable results and close to the experimental data. These results (Figure 7 and Figure 8) confirm AMBER and CHARMM as the main force fields for RNA simulation, as previously indicated by RMSD and torsional angles analyses.

The data for GROMOS simulations (Figure 8), for the propeller parameter, show values with a slight dispersion when compared to experimental data and B-DNA form. The standard deviation displays a high variation during the simulation, when compared to AMBER and CHARMM simulations. Again, the previous torsional angles results, on GROMOS force field, influenced the base pair parameters.

Buckle results, for GROMOS force field (Figure 8), were very close to crystal data and B-DNA form. When compared to AMBER and CHARMM force fields, the GROMOS simulations are in the same range with slight increase of standard deviation. Theses analyses show a low influence of torsional angles in this rotational parameters.

Finally, the opening parameter (Figure 8) for GROMOS simulations shows large dispersion of values when compared to experimental data and B-DNA form. The standard deviation displays a high variation during the simulation, in comparison with the others force field. These results confirm the loss of base pairing and denaturation of nucleic acids simulated on GROMOS force field.

Conclusions

The choice of force field on molecular dynamics simulations is crucial for accurate description of biomolecules. So, we performed 100 ns simulations with siRNA, siRNA complexed to protein, and DNA using AMBER99SB-ILDN, CHARMM27, and GROMOS53a6 aiming to assess the reliability of these force fields in describing such small double-strands.

Simulations with AMBER and CHARMM force fields were very stable and reproduced the experimental data and the experimental parameters for B-DNA. The obtained data points to AMBER and CHARMM as the main force fields for RNA simulation, as previously indicated for DNA.[6] On the other hand, analyses of RMSD, number of intramolecular hydrogen bonds, torsional angles, and base-pairs steps indicate that the nucleic acids simulated with GROMOS 53a6 force field have strong distortions. The torsional angles α and γ on GROMOS simulations displayed several problems such as disperse values, distant from experimental data.

In conclusion, despite being a very successful force field for simulating proteins and carbohydrates, GROMOS 53a6 leads to major distortion of nucleic acids, such as opening of double-strands, loss of base pairing and main parameters with high variation resulting in the complete disruption of the double strand.

Acknowledgments

This work was supported by Conselho Nacional de Desenvolvimento Científico e Tecnológico (CNPq), MCT, by Coordenação de Aperfeiçoamento de Pessoal de Nível Superior (CAPES), MEC, Brasília, DF, Brazil, and the Fundação de Amparo à Pesquisa do Estado do Rio Grande do Sul (FAPERGS).

Keywords: nucleic acids, RNA, DNA, force field, molecular dynamics

References and Notes

1. H. Großhans, W. Filipowicz, *Nature* **2008**, *451*, 414-416.
2. G. Meister, T. Tuschl, *Nature* **2004**, *431*, 343-349.
3. C. D. Novina, P. A. Sharp, *Nature* **2004**, *430*, 161-164.
4. M. Jinek, J. A. Doudna, *Nature* **2009**, *457*, 405-412.
5. K. Ye, L. Malinina, D. Patel, *Nature* **2003**, *426*, 874–878.
6. C. G. Ricci, A. S. C. de Andrade, M. Mottin, P. A. Netz, *J. Phys. Chem. B* **2010**, *114*, 9882–9893.
7. W. D. Cornell, P. Cieplak, C. I. Bayly, I. R. Gould, K. M., Jr. Merz, D. M. Ferguson, D. C. Spellmeyer, T. Fox, J. W. Caldwell, P. A. Kollman, *J. Am. Chem. Soc.* **1995**, *117*, 5179.
8. J. Wang, P. Cieplak, P. A. Kollman, *J. Comput. Chem.* **2000**, *21*, 1049–1074.
9. Y. Duan, C. Wu, S. Chowdhury, M. C. Lee, G. Xiong, W. Zhang, R. Yang, P. Cieplak, R. Luo, T. Lee, J. Caldwell, J. Wang, P. Kollman, *J. Comput. Chem.* **2003**, *24*, 1999–2012.
10. K. Lindorff-Larsen, S. Piana, K. Palmo, P. Maragakis, J. L. Klepeis, R. O. Dror, D. E. Shaw, *Proteins*, **2010**, *78*, 1950-1958.

11. A. D. Jr. Mackerell, J. W. Kuczera, M. Karplus, *J. Am. Chem. Soc.* **1995**, *117*, 11946–11975
12. A. D. Jr. Mackerell, N. Banavali, *J. Comp. Chem.* **2000**, *21*, 105-120.
13. N. Foloppe, A. D. Jr. Mackerell, *J. Comp. Chem.* **2000**, *21*, 86-104.
14. W. L. Jorgensen, J. Tirado-Rives, *J. Am. Chem. Soc.* **1988**, *110*, 1657–1666.
15. W. L. Jorgensen, D. S. Maxwell, J. Tirado-Rives, *J. Am. Chem. Soc.* **1996**, *118*, 11225–11236.
16. W. R. P. Scott, P. H. Hunenberger, I. G. Tironi, A. E. Mark, S. R. Billeter, J. Fennen, A. E. Torda, T. Huber, P. Kruger, W. F. van Gunsteren, *J. Phys. Chem. A* **1999**, *103*, 3596–3607.
17. C. Oostenbrink, A. Villa, A. E. Mark, W. F. van Gunsteren, *J. Comput. Chem.* **2004**, *25*, 1656-1676.
18. C. Oostenbrink, T. A. Soares, N. F. A. van der Vegt, W. F. van Gunsteren, *Eur. Biophys. J.* **2005**, *34*, 273–284.
19. M. Feig, B. M. Pettitt, *Biophys. J.* **1998**, *75*, 134–139.
20. X. Lu, W. K. Olson, *Nat. Protoc.* **2008,** *3*, 1213-27.
21. S. Pronk, S. Páll, R. Schulz, P. Larsson, P. Bjelkmar, R. Apostolov, M. R. Shirts, J. C. Smith, P. M. Kasson, D. van der Spoel, B. Hess, E. Lindahl, *Bioinformatics*, **2013**, *29*, 845-854.
22. M. W. Mahoney, W. L. Jorgensen, *J. Chem. Phys.* **2000** ,*112*, 8910-8922.
23. H. J. C. Berendsen, J. R. Grigera, T. P. J. Straatsma, *Phys. Chem.* **1987**, *91*, 6269–6271.
24. T. Darden, D. York, L. Pedersen, *J. Chem. Phys.* **1993**, *98*, 10089-10092.
25. B. Hess, H. Bekker, H. J. C. Berendsen, J. G. E. M. Fraaije, *J. Comput. Chem.* **1997**, *18*, 1463-1472.
26. S. Nosé, M. L. Klein, *Mol. Phys.* **1983**, *50*, 1055-1076.
27. M. Parrinello, A. Rahman, *J. Appl. Phys.* **1981**, *52*, 7182-7190.
28. G. Bussi, D. Donadio & M. Parrinello, *J. Chem. Phys.* **2007**, *126*, 014101-014107.
29. S. Nosé, *Mol. Phys.* **1984**, *52*, 255-268.
30. W. G. Hoover, *Phys. Rev. A.* **1985,** *31*, 1695-1697.
31. D. Rappaport, *Mol. Phys.* **1983**, *50*, 1151.
32. R. E. Dickerson, H. R. Drew, B. N. Conner, R. M. Wing, A. V. Fratini, M. L. Kopka, *Science* **1982**, *216*, 475–485.
33. R. E. Dickerson, *Nucleic Acids Res.* **1989**, *17*, 1797–1803.
34. R. E. Dickerson, *Methods Enzymol.* **1992**, *211*, 67–110.
35. X. J. Lu, W. K. Olson, *J. Mol. Biol.* **1999**, *285*, 1563–1575.
36. N. Arora, B. Jayaram, *J. Phys. Chem. B* **1998**, *102*, 6139–6144.
37. P. Varnai, D. Djuranovic, R. Lavery, B. Hartman, *Nucleic Acids Res.* **2002**, *30*, 5398–5406.
38. M. A. ElHassan, C. R. Calladine, *Philos. Trans. R. Soc. London, Ser. AsMath. Phys. Eng. Sci.* **1997**, *355*, 43–100.

5. DISCUSSÃO GERAL

5.1 ANÁLISE GLOBAL DA ESTRUTURA

Os resultados obtidos durante a simulação de dinâmica molecular dos siRNAs e dos DNAs demonstram estruturas mais estáveis nos campos de força AMBER e CHARMM, com valores de RMSD mais baixos em comparação com o campo de força GROMOS. Por outro lado, os ácidos nucleicos simulados no campo de força GROMOS apresentaram altos valores de RMSD, indicando uma possível perda estrutural do siRNA, conforme previamente descrito para a molécula de DNA (RICCI ET AL., 2010). Além do RMSD, a estabilidade das duplas fitas foi também avaliada por outras propriedades, como o padrão de interações por ligação de hidrogênio associados aos pareamentos de bases esperados.

O campo de força AMBER apresentou um rigidez maior frente ao CHARMM, já que as ligações de hidrogênio durante as simulações apresentaram valores mais estáveis com menor perda de pareamento entre as bases. Essa característica presente no campo de força AMBER pode não ser adequada para eventos conformacionais em que a molécula de ácido nucleico necessite de uma maior flexibilidade. Assim, o campo de força CHARMM apresenta vantagem, em relação ao AMBER, nessas situações.

Por outro lado, o campo de força GROMOS demonstrou perda de pareamento de bases nas análises de interações por ligações de hidrogênio. Esses dados estão de acordo com as análises prévias de RMSD, confirmando a perda estrutural do siRNA e consequente deformação da dupla-hélice durante as simulações por DM.

A complexação dos siRNAs com a proteína p19, em comparação com o siRNA livre, promoveu redução nos valores de RMSD do ácido nucleico, demonstrando uma rigidez maior da estrutura do siRNA quando complexado a proteína. Apesar dos valores RMSD para os siRNA complexados a proteína terem diminuídos também no campo de força GROMOS, as estruturas dos ácidos nucleicos continuaram apresentando perda de pareamento entre as bases, ou seja, ruptura da dupla fita e deformação da dupla hélice.

Os resultados obtidos para descrição da estrutura global dos siRNAs livres durante as simulações por DM foram condensados na Figura 17. Nesta representação é possível verificar a estabilidade das estruturas simuladas nos campos de força que descrevem todos os átomos do sistema frente às estruturas estudadas no campo de força de átomo unido. A desnaturação do siRNA fica clara no campo de força GROMOS, já que a estrutura inicial é completamente perdida.

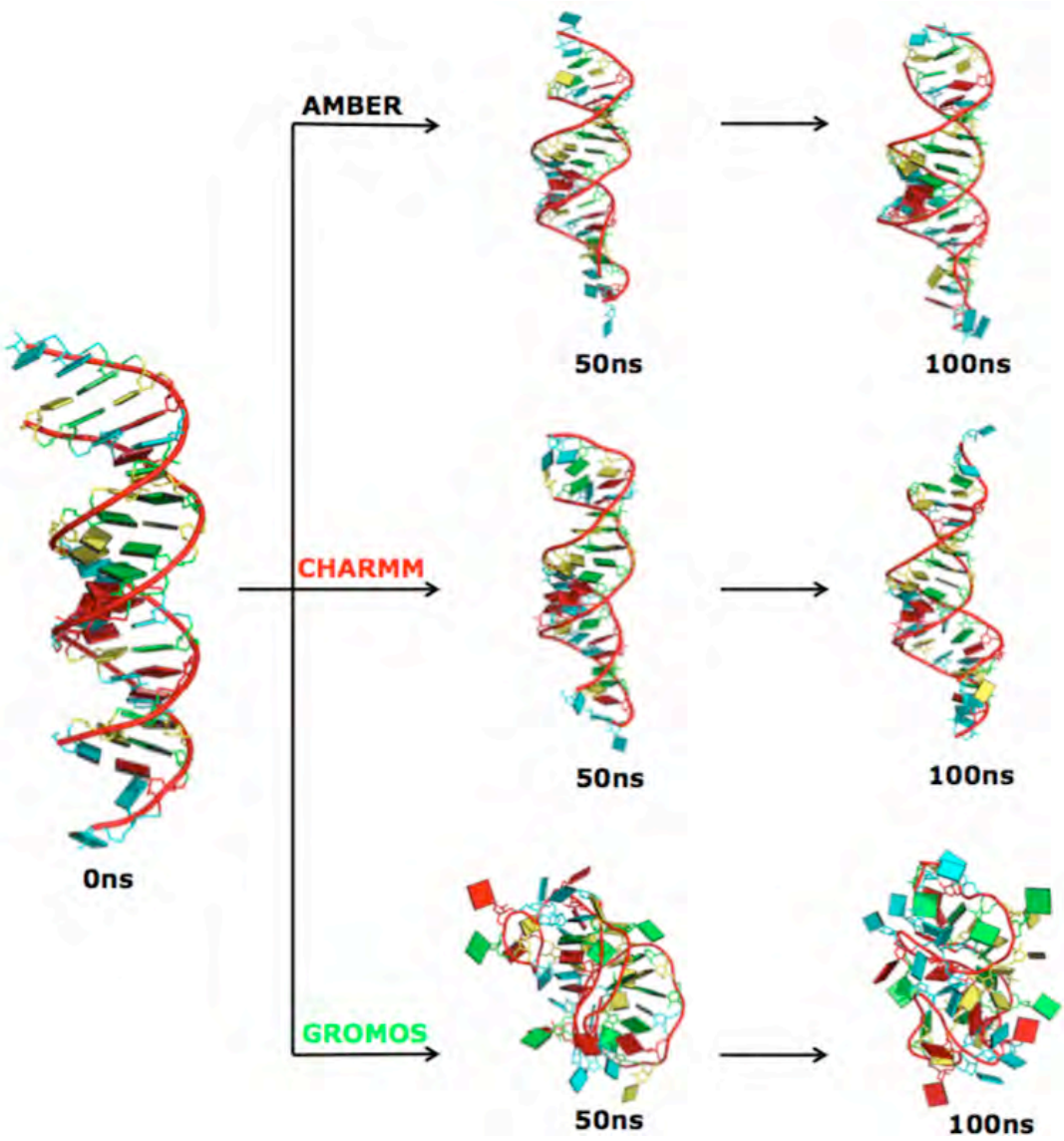

Figura 17. Diferenças estruturais apresentadas pelos siRNAs durante as simulações por DM nos três campos de força.

5. 2 Ângulos Torcionais e Parâmetros Geométricos

Embora dados de RMSD e padrão de ligações de hidrogênio ofereçam uma perspectiva global sobre a estabilidade do ácido nucleico, o entendimento da amostragem conformacional produzida com resolução atômica exige a avaliação de propriedades locais, relacionadas a bases individuais ou em pares. Para tal, diversos descritores foram avaliados e seus valores médios ao longo das trajetórias e entre as três trajetórias produzidas foram empregados.

As simulações por DM dos ácidos nucleicos nos campos de força AMBER e CHARMM apresentaram resultados muito próximos aos dados experimentais para todos os ângulos torcionais analisados. Alguns parâmetros apresentaram alguma faixa de variação, embora a estrutura global tenha permanecido estável durante as simulações. Como os ângulos torcionais são responsáveis pelo esqueleto conformacional dos ácidos nucleicos, os parâmetros geométricos são consequências mecânicas da conformação obtida nesses esqueletos. Assim, como obtivemos valores próximos aos dados experimentais para os ângulos rotacionais nas simulações com AMBER e CHARMM, os parâmetros geométricos analisados se mostraram estáveis e próximos aos dados experimentais. Esses resultados demonstram uma excelente descrição da conformação do esqueleto de RNA e DNA nesses campos de força.

Por outro lado, o campo de força GROMOS apresentou problemas na descrição conformacional do esqueleto durante as simulações. Os ângulos torcionais α e γ apresentaram valores extremamente altos, distantes dos dados experimentais, e com alta flutuação. Da mesma forma, a maior parte dos descritores geométricos apresentou resultados ruins, com alta variação e diferença em relação aos valores experimentais.

Os resultados obtidos, para o campo de força GROMOS, podem estar correlacionados com os diferentes potenciais torcionais de energia que os ângulos α e γ adotam nos campos de força de átomo unido em comparação com os campos de forças que descrevem todos os átomos do sistema (RICCI ET AL. 2010; SOARES ET AL., 2005) (Figura 18).

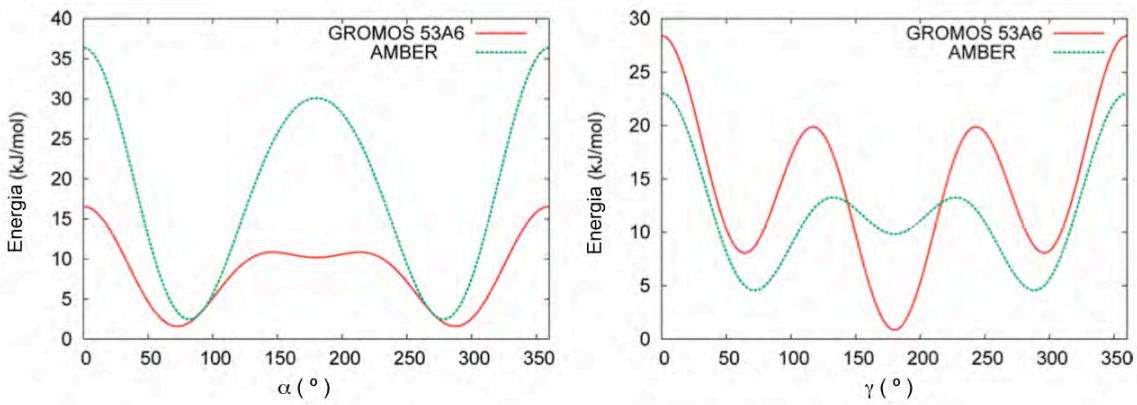

Figura 18. Perfis torcionais de energia, para os ângulos α e γ, calculados a partir dos parâmetros dos campos de força AMBER e GROMOS. (adaptado de RICCI ET AL., 2010)

Por fim, os parâmetros analisados confirmaram os campos de força AMBER e CHARMM como os mais adequados para simulações de RNA, bem como de DNA. Por outro lado, os descritores também reforçaram a perda do pareamento de bases e assim a desnaturação dos ácidos nucleicos simulados no campo e força GROMOS. Este resultado indica que a forma como foi desenvolvido o campo de força de átomo unido, pode estar relacionado com a perda estrutural dos ácidos nucleicos durante as simulações.

6. CONCLUSÕES

A partir dos objetivos previamente descritos, a concretização do presente trabalho tornou possível:

- Confirmação dos campos de força *all-atom* (AMBER e CHARMM) como principais escolhas para simulação de RNA e, conforme já descrito, para DNA. Em contrapartida, apesar de ser um campo de força muito bem sucedido para a simulação de proteínas e carboidratos, o campo de força *united-atom* (GROMOS) apresentou uma série de problemas, resultando na deformação e rompimento da dupla hélice;

- Analisar os diferentes ângulos torcionais, que descrevem o esqueleto conformacional dos ácidos nucleicos, demonstrando que as moléculas simuladas no campos de forças AMBER e CHARMM apresentaram resultados muito próximos aos dados experimentais. Por outro lado, o campo de força GROMOS apresentou problemas nos ângulos torcionais e assim a deformação do esqueleto conformacional durante as simulações;

- Verificar a influência dos ângulos torcionais nos descritores geométricos. Os descritores geométricos confirmaram os dados obtidos nas análises anteriores, confirmando os campos de força que descrevem todos os átomos do sistema como as principais escolhas para simulação de RNA.

- Avaliar a influência da proteína na estrutura dos ácidos nucleicos, durante a simulação. A complexação dos siRNAs com a proteína p19 promoveu uma rigidez na estrutura do siRNA em todos os campos de força estudados. Contudo, no campo de força GROMOS, apesar da rigidez, as estruturas dos ácidos nucleicos continuaram apresentando uma série de problemas e assim deformação da dupla hélice.

8. REFERÊNCIAS BIBLIOGRÁFICAS

Bourne, P. E.; Weissig, H.: Structural Bioinformatics. 1st Ed., **2003**, Hoboken, New Jersey.

Darden, T.; York, D.; Pedersen, L.: Particle mesh Ewald: An N●log(N) method for Ewald sums in large systems. *J. Chem. Phys*., **1993**, *98*, 10089–10092.

De Sant'anna, C. M. R.: Glossário de termos usados no planejamento de fármacos (recomendações IUPAC 1997). *Quim. Nova*, **2002**, *25*, 505-512.

Foloppe, N.; MacKerell, Jr., A.D.: All-atom empirical force field for nucleicacids: (1) Parameter optimization based on small molecule and condensed phase macromolecular target data. *J. Comp. Chem.* **2000**, *21*, 86-104.

Großhans, H.; Filipowicz, W.: The expanding world of small RNAs. *Nature,* **2008**, *451*, 414-416.

Hannon, G. J.: RNA interference. *Nature,* **2002**, *418*, 244-251.

Hashem, Y.; Auffinger, P.: A short guide for molecular dynamics simulations of RNA systems. *Methods,* **2009,** *47*, 187–197.

Hess, B.; Bekker, H.; Berendsen, H. J. C.; Fraaije, J. G. E. M.: LINCS: a linear constraint solver for molecular simulations. *J. Comput. Chem*., **1997**, *18*, 1463-1472.

Hoover, W. G.: Canonical dynamics: equilibrium phase-space distributions. *Phys. Rev. A.*, **1985**, *31*, 1695-1697.

Humphrey, W.; Dalke, A.; Schulten, K.: VMD - Visual Molecular Dynamics. J. Molec. Graphics., **1996**, *14*, 33-38.

Jinek, M.; Doudna, J. A.: A three-dimensional view of the molecular machinery of RNA interference. *Nature,* **2009**, *457*, 405-412.

Laing, C.; Schlick, T.: Computational approaches to 3D modeling of RNA. *J. Phys: Condens Matter* **2010**, *22*, 283101.

Laing, C.; Schlick, T.: Computational approaches to RNA structure prediction, analysis, and design. Curr. Opin. Struct. Biol. **2011**,1-13.

Leach, A. R.: Molecular Modelling: Principles and Applications. 2nd Ed., **2001**, Longman, Cingapura.

Lindorff-Larsen, K.; Piana, S.; Palmo, K.; Maragakis, P.; Klepeis, J. L.; Dror, R. O.; Shaw, D. E.: Improved side-chain torsion potentials for the Amber ff99SB protein force field. *Proteins: Structure, Function, and Bioinformatics*, **2010**, *78*, 1950–1958.

Lu, X.; Olson, W. K.: 3DNA: a software package for the analysis, rebuilding and visualization of three-dimensional nucleic acid structures *Nucl. Acids. Res.,* **2003** *31 (17)*, 5108-21.

Lu, X.; Olson, W. K.: 3DNA: a versatile, integrated software system for the analysis, rebuilding and visualization of three-dimensional nucleic-acid structures. *Nat. Protoc.,* **2008** *3*, 1213-27.

MacKerell, Jr., A.D.; Banavali, N.: All-Atom Empirical Force Field for Nucleic Acids: 2) Application to Molecular Dynamics Simulations of DNA and RNA in Solution. *J. Comp. Chem.* **2000**, *21*, 105-120.

MacKerell, Jr., A.D.; Nilsson, L.: Molecular dynamics simulations of nucleic acid–protein complexes. *Curr. Opin. Struct. Biol.* **2008**, *18*, 194–199.

Mahoney, M. W.; Jorgensen, W. L.: A five-site model for liquid water and the reproduction of the density anomaly by rigid, nonpolarizable potential functions, *J. Chem. Phys.* **2000** ,*112,* 8910-8922.

Meister, G.; Tuschl, T.: Mechanisms of gene silencing by double-stranded RNA. *Nature*, **2004**, *431*, 343-349.

Nosé, S.; Klein, M. L.: Constant pressure molecular dynamics for molecular systems. *Mol. Phys.*, **1983**, *50*, 1055-1076.

Nosé, S.: A molecular dynamics method for simulations in the canonical ensemble. *Mol. Phys*., **1984**, *52*, 255-268.

Novina, C. D.; Sharp, P. A.: The RNAi revolution. *Nature,* **2004**, *430*, 161-164.

Oostenbrink, C.; Villa, A.; Mark, A. E.; van Gunsteren, W. F.: A biomolecular force field based on the free enthalpy of hydration and solvation: the GROMOS force-field parameter sets 53A5 and 53A6. *J. Comput. Chem.*, **2004**, *25*, 1656-1676.

Parrinello, M.; Rahman, A.: Polymorphic transitions in single crystals: A new molecular dynamics method. *J. Appl. Phys.*, **1981**, *52*, 7182-7190.

Pronk, S.; Páll, S.; Schulz, R.; Larsson, P.; Bjelkmar, P.; Apostolov, R.; Shirts, M. R.; Smith, J. C.; Kasson, P. M.; van der Spoel, D.; Hess, B.; Lindahl, E.: GROMACS 4.5: a high-throughput and highly parallel open source molecular simulation toolkit. *Bioinformatics*, **2013**, *29*, 845-854.

Ricci, C. G.; de Andrade, A. S. C.; Mottin, M.; Netz, P. A.: Molecular Dynamics of DNA: Comparison of Force Fields and Terminal Nucleotide Definitions. *J. Phys. Chem. B,* **2010**, *114*, 9882–9893.

Schaftenaar, G.; Noordik, J. H.: MOLDEN: a pre- and post-processing program for molecular and electronic structures. *J. Comput. Aided Mol. Des*., **2000**, *14*, 123-134.

Schrödinger, LLC: The PyMOL Molecular Graphics System, Version 1.8.

Serdyuk, I.N.; Zaccai, N.R.; Zaccai, J.: Molecular dynamics. In: _____. *Methods in Molecular Biophysics: Structure, Dynamics, Function.* Cambridge: Cambridge University Press, **2007**.

Sim, A. YL.; Minary, P.; Levitt, M.: Modeling Nucleic Acids. *Curr. Opin. Struct. Biol.* **2012**, *22*, 273–278.

Soares, T. A.; Hünenberger, P. H.; Kastenholz, M. A.; Kräutler, V.; Lenz, T.; Lins, R. D.; Oostenbrink, C.; van Gunsteren, W. F.: An improved nucleic acid parameter set for the GROMOS force field. *J. Comput. Chem.*, **2005**, *26*, 725-737.

Tomari, Y.; Zamore, P. D.: Perspective: machines for RNAi. *Genes & Development,* **2005**, *19*, 517–529.

van der Spoel, D.; Lindahl, E.; Hess, B.; van Buuren, A. R.; Apol, E.; Meulenhoff, P. J.; Tleleman, D. P.; Sljbers, A. L. T. M.; Feenstra, K. A.; van Druner, R.; Berendsen, H. J. C.: Gromacs User Manual version 4.5.4, *www.gromacs.org* (**2010**)

van Gunsteren, W. F.: Molecular dynamics of proteins and nucleic acids. *Fresenius Z. Anal. Chem.* **1987,** *327*, 69-70.

van Gunsteren, W. F.; Bakowies, D.; Baron, R.; Chandrasekhar, I.; Christen, M.; Daura,, X.; Gee, P.; Geerke, D. P.; Glättli, A.; Hünenberger, P. H.; Kastenholz, M. A.; Oostenbrink, C.; Schenk, M.; Trzesniak, D.; van der Vegt, N. F. A.; Yu, H. B.: Biomolecular modeling: goals, problems, perspectives. *Angew. Chem. Int. Ed. Engl*. **2006**, *43*, 4064–4092.

Verli, H.: Bioinformática da Biologia à flexibilidade molecular. 1st Ed., **2014,** Porto Alegre, Brazil.

Von Kitzing, E.: Modeling DNA structures: Molecular mechanics and molecular dynamics. *Methods in Enzymology*, **1992**, *211*, 449-467.

Wang, Y.; Li, Y.; Ma, Z.; Yang, W.; Ai, C.: Mechanism of MicroRNA-Target Interaction: Molecular Dynamics Simulations and Thermodynamics Analysis. *PLoS Comput. Biol.* **2010,** *6*, e1000866.

Xia, Z.; Zhu, Z.; Zhu, J.; Zhou, R.: Recognition Mechanism of siRNA by Viral p19 Suppressor of RNA Silencing: A Molecular Dynamics Study *Biophys. J.* **2009**, *96*, 1761–1769.

Ye, K.; Malinina, L.; Patel, D.: Recognition of small interfering RNA by a viral suppressor of RNA silencing. *Nature*., **2003,** *426*, 874–878.

9. APÊNDICES

Trabalhos publicados durante o desenvolvimento do mestrado (Apêndices A e B) e artigo em preparação (Apêndice C) durante esse período, que será submetido à revista *European Journal of Medicinal Chemistry*. Desenvolvimento de imagens (Apêndice D) para o livro-texto "Bioinformática: da Biologia à Flexibilidade Molecular" que encontra-se publicado gratuitamente no endereço: http://www.ufrgs.br/bioinfo/ebook/

Apêndice A: Artigo publicado "Conformational Characterization of Ipomotaosides and Their Recognition by COX-1 and 2"

Apêndice B: Artigo aceito para publicação "2´, 3´-Dialdehyde of ATP, ADP, and Adenosine Inhibit HIV-1 Reverse Transcriptase and Infection".

Apêndice C: Dados do Artigo em preparação para submissão "Effects of TMI binding on antithrombin and comparison with the heparin binding".

Apêndice D: Dados do Livro-texto "Bioinformática: da Biologia à Flexibilidade Molecular" publicado com imagens elaboradas durante o mestrado.

9.1 APÊNDICE A

Conformational Characterization of Ipomotaosides and Their Recognition by COX-1 and 2

Arantes PR, Sachett LG, Graebin CS, Verli H.

Molecules, 2014, 19, 5421-5433.

Molecules **2014**, *19*, 5421-5433; doi:10.3390/molecules19045421

OPEN ACCESS

molecules

ISSN 1420-3049

www.mdpi.com/journal/molecules

Article

Conformational Characterization of Ipomotaosides and Their Recognition by COX-1 and 2

Pablo R. Arantes [1], Liana G. Sachett [1], Cedric S. Graebin [2] and Hugo Verli [1,*]

[1] Centro de Biotecnologia, Universidade Federal do Rio Grande do Sul, Avenida Bento Gonçalves 9500, CP 15005, Porto Alegre, RS 91500-970, Brazil; E-Mails: pabloarantes@cbiot.ufrgs.br (P.R.A.); lianasachett@cbiot.ufrgs.br (L.G.S.)

[2] Departamento de Química, Instituto de Ciências Exatas, Universidade Federal Rural do Rio de Janeiro, Cidade Universitária, Seropedica, RJ 23897-000, Brazil; E-Mail: cedric@ufrrj.br

* Author to whom correspondence should be addressed; E-Mail: hverli@cbiot.ufrgs.br; Tel./Fax: +55-51-3308-7770.

Received: 5 March 2014; in revised form: 18 April 2014 / Accepted: 21 April 2014 / Published: 24 April 2014

Abstract: The aerial parts of *Ipomoea batatas* are described herein to produce four new resin glycosides, designated as ipomotaosides A, B, C, and D. Ipomotaoside A was found to present inhibitory activity on both cyclooxygenases. However, the conformational elucidation of these molecules may be difficult due to their high flexibility. In this context, the current work presents a conformational characterization of ipomotaosides A–D in aqueous and nonaqueous solvents. The employed protocol includes metadynamics evaluation and unrestrained molecular dynamics simulations (MD). The obtained data provided structural models for the ipomotaosides in good agreement with previous ROESY distances measured in pyridine. Accordingly, the most abundant conformation of ipomotaoside A in solution was employed in flexible docking studies, providing a structural basis for the compound's inhibition of COX enzymes. The so-obtained complex supports resin glycosides' role as original scaffolds for future studies, aiming at structural optimization and development of potential new anti-inflammatory agents.

Keywords: ipomotaosides; resin glycosides; disaccharides; molecular dynamics; docking; COX; inflammatory process

---

1. Introduction

Ipomotaosides are resin glycosides derived from the aerial parts of *Ipomea batatas*. These resin glycosides are separated in four different structures, named ipomotaosides A (**1**), B (**2**), C (**3**), and D (**4**) [1] (Figure 1).

Figure 1. Representations of the ipomotaosides characterized in the current work.

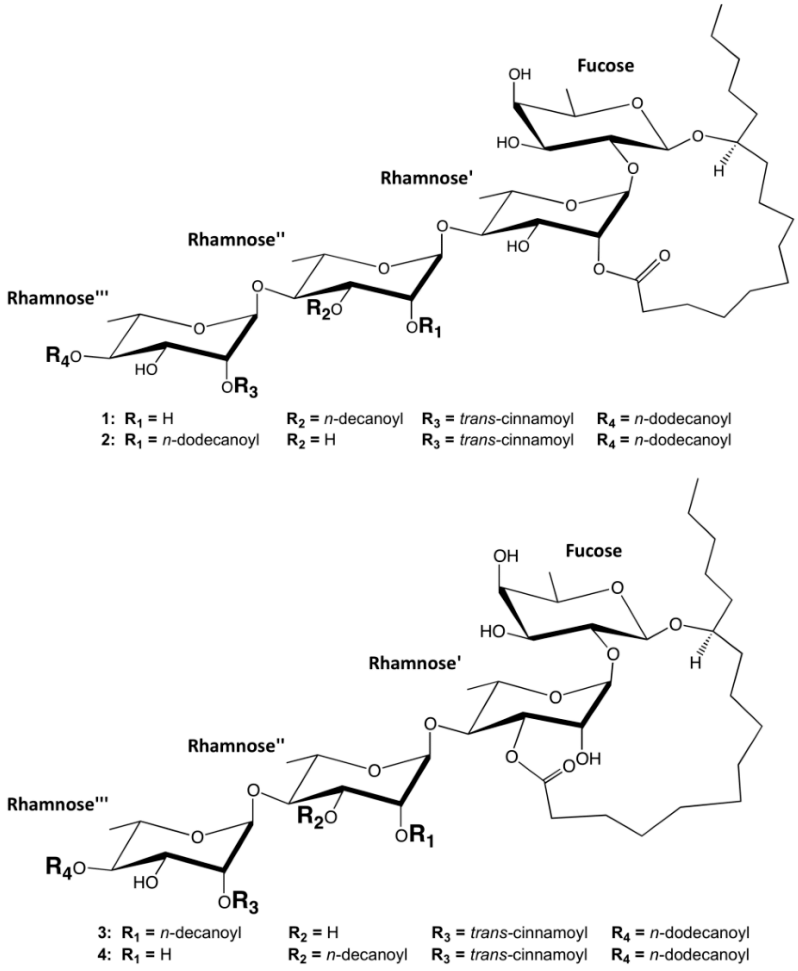

These compounds are composed of a macrocyclic structure, various hydrophobic acyl chains and the same hydrophilic oligosaccharide core. Differently from the roots of *I. batatas*, which are used in folkloric medicine for anemia, diabetes, hemorrhage and hypertension [2], resin glycosides from the aerial parts as well as roots are inactive cytotoxic agents and known to exhibit several biological effects such as inhibition of multidrug resistance efflux pumps (EPIs) [3–5]. Additionally, recent results demonstrated that ipomotaoside A from *I. batatas* is capable of inhibiting cyclooxygenases (COX) 1 and 2 [1]. These enzymes are committed in prostanoid biosynthesis, converting arachidonic acid (AA) and O_2 to prostaglandin endoperoxide PGH_2 in two different active sites, cyclooxygenase and peroxidase [6]. The first step consists in oxygenating AA to prostaglandin G_2 (PGG_2) in the cyclooxygenase site. In the second step, this intermediate moves to the peroxidase active site to be

reduced to PGH_2, which is converted into other prostaglandins and thromboxanes responsible for mediating the inflammatory process [6], so the inhibition of both COXs by ipomotaoside A indicates a potential role of these molecules in modulating inflammation.

Future efforts to develop these compounds through rational design, however, are impaired by the lack of structural information on their complexation to COX. Although there are crystallized glycoconjugates described in the literature [7] due to the high flexibility of glycosidic linkages in carbohydrates [8,9] and acyl chains and the consequent high amount of conformers coexisting in solution, [8,10,11] it is unusual to obtain 3D models for glycoconjugates from crystallographic methods. On the other hand, NMR methods are the main choice for dealing with such flexible compounds, for example, if a reasonable amount of ROESY/NOESY contacts are obtained [8]. Still, the chemical environment in which NMR experiments are performed may not correspond to that of physiological solutions, with potential conformational influences. In the case of ipomotaosides, the spectroscopic elucidation was performed on pyridine, a heterocyclic and aromatic solvent that does not offer a good resemblance to biological media.

Considering the adversities found in obtaining atomistic models for complex carbohydrates and glycoconjugates in environments mimicking biological solutions, the current work aimed to characterize ipomotaosides **1**–**4** in aqueous and pyridine solutions. Therefore, the conformational characterization of all molecules was included in the manuscript in order to offer to the researcher of the field additional structural information on this class of compounds. Also, the conformational ensemble in pyridine was used as reference for spectroscopic validation, and the so-obtained most abundant conformation of ipomotaoside A in aqueous solution was submitted to docking studies to provide insights into its inhibitory activity against COXs.

The strategy employed for conformational characterization of ipomotaosides was previously described [11] and validated against NMR data for compounds such as saponins [12], exopolysaccharides [13], galactans and fucans [14], and a series of glycoproteins and glycopeptides [11,15], based on building glycan chains from most abundant conformational states in solution, as determined by MD simulations. The built molecules were submitted to additional simulations in order to account to potential inter-residue interactions and, consequently, conformational effects.

2. Results and Discussion

2.1. Dynamics of Isolated Disaccharides

On the basis of the ipomotaosides' structures, two glycosidic linkages had their conformational behavior were evaluated by metadynamics, in both pyridine and water: α-L-Rha-(1→4)-α-L-Rha and α-L-Rha-(1→2)-β-D-Fuc. The obtained patterns point to similar conformations in both solvents, with a displacement of the global minimum from the northwest to the southwest quadrants upon modification of rhamnose residue linkage from C-2 (fucose) to C-4 (rhamnose) (Figure 2A,B).

The obtained conformational behavior of ipomotaosides disaccharide units was further compared to previous crystallographic and molecular mechanics (MM3) data of tricolorin A, the only member of this class of oligosaccharides with a published crystal structure [7] for the α-(1→2) linkage. The two main minima are located in similar regions as clearly demonstrated for both works. However, the main

minimum is inverted, located in the southwest quadrant in MM3 (region in which the crystallographic geometry was observed), and in the northwest quadrant in GROMOS. Some aspects may be related to this difference, such as the nature of the force field (united atom or all atom, validated against condensed or gas phase) and of the employed method (metadynamics or adiabatic maps). Also, it should be noted that the location of the minimum in pyridine is on the opposite quadrant than the crystallographic geometry.

Figure 2. (**A**,**B**) Conformational behavior of α-L-Rha-(1→2)-β-D-Fuc and α-L-Rha-(1→4)-α-L-Rha linkages, as obtained from metadynamics in both pyridine and water; (**C**,**D**) Distribution of Φ and Ψ dihedral angles during simulations associated with the glycosidic linkages of isolated disaccharides. The aqueous solution is represented as black and the nonaqueous solution (pyridine) is indicated as red.

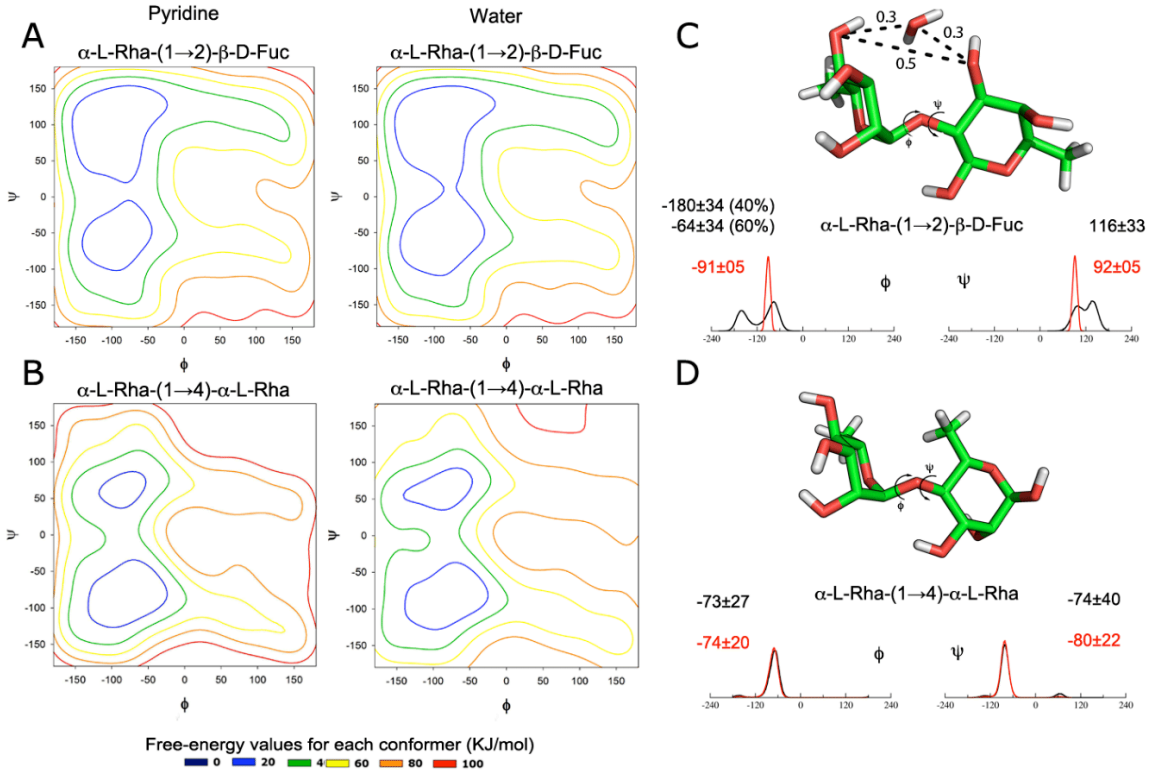

Despite the identification of two minima on the metadynamics contour plots, the MD simulations of both minima populated a single region, corresponding to the global minima (Figure 2C,D), which could indicate a similar conformational state between the two solvents. Still, glycosidic linkages presented a more rigid pattern on pyridine than on water, in agreement with the usual choice of the first for spectroscopic studies. Even being more rigid, the linkages dynamic under pyridine lies within the conformational behavior observed in water (Figure 2C,D). This data is in agreement with previous results indicating that pyridine has a discrete effect on molecule conformation [12].

The conformation observed in water for Rha-(1→2)-β-D-Fuc, with the appearance of a second minimum at the Φ angle, is a result of the hydrogen bonds between water and hydroxyl groups of of rhamnose C-4 and fucose C-3 (Figure 2C). This behavior is demonstrated at radial distribution function (Figure S1), where the respective oxygen atoms indicate the presence of a water molecule during the simulation. The distance between these two oxygen atoms is lower when the water is present (Figures 2C and S2), showing a solvent influence on Φ angle and so resulting on its second minimum in water.

The most abundant conformational states of each glycosidic linkage were then used as starting geometries for the construction of complete models of structures **1**–**4**, previously described as a successful approach to obtain 3D models of glycan chains in solution, [11–13,15] and submitted to MD simulations for further geometry refinement in the whole molecule scaffold as well as for conformational sampling.

2.2. Ipomotaosides Dynamics

The MD simulation of complete ipomotaosides allowed a comparison between the conformational profile adopted by the isolated glycosidic linkages and their behavior when composing the whole molecules (Table 1 and Figure S3). For the α-L-Rha-(1→2)-β-D-Fuc linkage, upon inclusion within ipomotaosides in pyridine, a new conformational state, at Φ and Ψ angles, is observed in compounds **1**, **3**, and **4** (Table 1) in comparison to the isolated linkage (Figure 2). Such effect appears to be related to the rigidity promoted by the macrocycle, more pronounced than the influence of acyl chains (Figure 3 and Figures S4–S6).

Table 1. Dihedral angles from Ipomotaosides glycosidase linkages, as obtained from MD.

		Glicosidic Linkage					
Compound	**Condition**	**α-L-Rha′-(1→2)-β-D-Fuc**		**α-L-Rha″-(1→4)-α-L-Rha′**		**α-L-Rha‴-(1→4)-α-L-Rha″**	
		Φ	Ψ	Φ	Ψ	Φ	Ψ
Ipomotaoside 1	MD in pyridine	−171 ± 29 (42%)	79 ± 40 (37%)	−75 ± 22	−85 ± 14	−71 ± 11	−81 ± 10
		−73 ± 28 (58%)	−51 ± 29 (63%)	-	-	-	-
	MD in water	−163 ± 15	86 ± 19	−74 ± 22	−87 ± 21	−71 ± 15	−82 ± 12
Ipomotaoside 2	MD in pyridine	−165 ± 14	82 ± 15	−76 ± 14	−83 ± 11	−76 ± 14	−83 ± 11
	MD in water	−71 ± 26 (14%)	−51 ± 13 (14%)	−76 ± 42	−87 ± 19	−78 ± 40	−88 ± 18
		−170 ± 31 (86%)	81 ± 56 (86%)	-	-	-	-
Ipomotaoside 3	MD in pyridine	−183 ± 25 (47%)	76 ± 27 (47%)	−74 ± 11	−82 ± 10	−75 ± 14	−82 ± 11
		−91 ± 29 (53%)	−35 ± 37 (53%)	-	-	-	-
	MD in water	−173 ± 10	87 ± 11	−72 ± 26	−82 ± 13	−77 ± 37	−86 ± 17
Ipomotaoside 4	MD in pyridine	−171 ± 25 (43%)	83 ± 26 (43%)	−71 ± 39	−85 ± 16	−74 ± 11	−84 ± 10
		−85 ± 25 (57%)	−31 ± 40 (57%)	-	-	-	-
	MD in water	−173 ± 09	87 ± 09	−97 ± 33 (34%)	−83 ± 20 (34%)	−80 ± 26	−84 ± 15
		-	-	−185 ± 18 (66%)	−150 ± 18 (66%)	-	-

Figure 3. Root mean square fluctuation (RMSF) for ipomotaoside A macrocycle and acyl chains. A tridimensional representation of each structure is highlighted in green, at the top, and the corresponding RMSF is at the bottom. Aqueous solution is represented in black and pyridine is indicated in red.

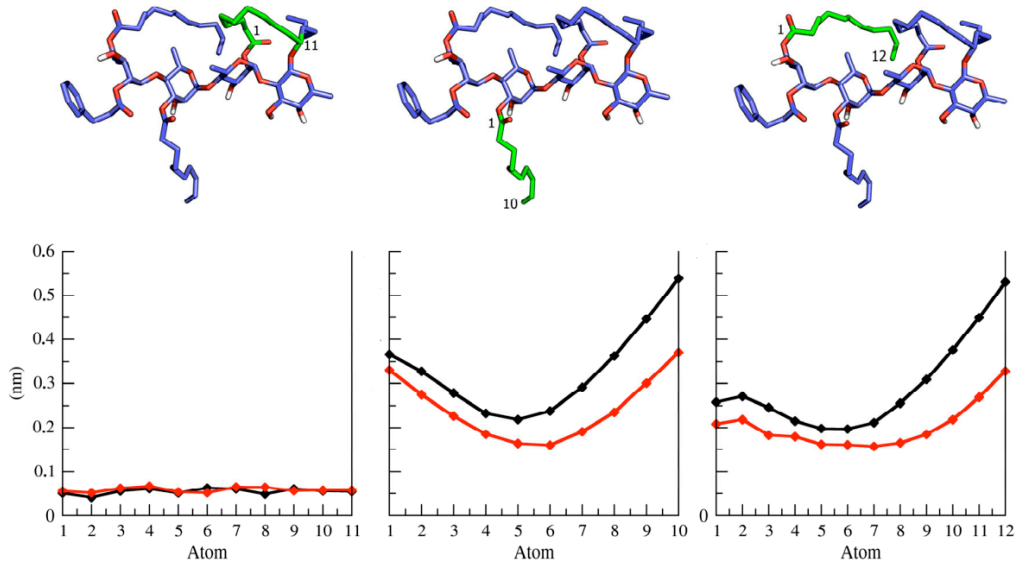

In fact, a similar situation is described in the literature for tricolorin A [7], a glycoconjugate in which the macrocycle imposes a conformational limit on the linked carbohydrate residues. On the other hand, the α-L-Rha-(1→4)-α-L-Rha linkage in pyridine and water, outside the macrocycle, shows no conformational dependence on the entire molecule scaffold (Table 1 and Figure S3), pointing again to a minor conformational influence of the hydrophobic acyl chains, as demonstrated on tricolorin A [7].

Considering that structures **1**–**4** have been previously characterized by NMR spectroscopy, [1] the interproton contacts were used to validate the conformational ensemble obtained from unrestrained MD simulations (Table 2). As a general feature, most of the experimentally observed contacts between ipomotaosides protons were properly reproduced on the performed simulations, pointing to a precise conformational characterization of these compounds in pyridine. These results are in agreement with previous Calonyctin A restrained MD studies [16], another glycoconjugate of the resin glycoside type, where the average of NOESY violation is less than 10%. Such results also supported the validity of the conformational sampling of these compounds in water, since no spectroscopic data is available for this solvent.

While ipomotaoside A represents a new scaffold to modulate COX [1], future medicinal chemistry efforts to guide the optimization of its chemical structure may be reinforced by the elucidation of the inhibitor-enzyme complex 3D structure. Such a complex could also explain the molecular basis for the activity of these structurally unusual compounds when compared to drugs in clinical use modulating this enzyme. In this context, the most abundant conformational states of ipomotaoside A in water were employed in docking studies on both COX enzymes.

Table 2. Comparison between ROESY * contacts of Ipomotaosides and the interproton distances from MD Simulations.

Ipomotaoside	Proton 1	Proton 2	Average of Interproton distance from MD (Å)	Ipomotaoside	Proton 1	Proton 2	Average of Interproton distance from MD (Å)
1	Fuc-(H1)	Fuc-(H5)	2.4 ± 0.2	**3**	Fuc-(H1)	Fuc-(H5)	2.4 ± 0.2
	Rha'-(H1)	Fuc-(H1)	2.5 ± 0.7		Rha'-(H1)	Fuc-(H1)	2.5 ± 0.7
	Rha'-(H1)	Fuc-(H2)	3.2 ± 0.5		Rha'-(H1)	Fuc-(H2)	3.2 ± 0.4
	Rha'-(H1)	Fuc-(H3)	3.4 ± 0.8		Rha'-(H1)	Fuc-(H3)	3.6 ± 0.8
	Rha'-(H1)	Fuc-(H4)	5.5 ± 0.5		Rha'-(H5)	Fuc-(H1)	4.9 ± 0.3
	Rha"-(H1)	Rha'-(H3)	3.4 ± 0.3		Rha"-(H1)	Rha'-(H2)	4.7 ± 0.2
	Rha"-(H1)	Rha'-(H4)	2.5 ± 0.3		Rha"-(H1)	Rha'-(H4)	2.5 ± 0.2
	Rha'"-(H1)	Rha"-(H4)	2.6 ± 0.3		Rha"-(H1)	Rha'-(H5)	4.4 ± 0.1
2	Fuc-(H1)	Fuc-(H5)	2.4 ± 0.2		Rha'"-(H1)	Rha"-(H3)	3.3 ± 0.2
	Rha'-(H1)	Fuc-(H1)	3.3 ± 0.3		Rha'"-(H1)	Rha"-(H4)	2.5 ± 0.3
	Rha'-(H1)	Fuc-(H2)	2.6 ± 0.3		Rha'"-(H1)	Rha"-(H5)	4.4 ± 0.1
	Rha'-(H1)	Fuc-(H3)	4.4 ± 0.1	**4**	Fuc-(H1)	Fuc-(H5)	2.4 ± 0.2
	Rha'-(H2)	Fuc-(H2)	2.2 ± 0.3		Rha'-(H1)	Fuc-(H1)	2.5 ± 0.7
	Rha'-(H2)	Fuc-(H3)	4.7 ± 0.3		Rha'-(H1)	Fuc-(H2)	3.1 ± 0.5
	Rha"-(H1)	Rha'-(H3)	3.4 ± 0.2		Rha'-(H1)	Fuc-(H3)	3.5 ± 0.8
	Rha"-(H1)	Rha'-(H4)	2.5 ± 0.3		Rha"-(H1)	Rha'-(H4)	2.5 ± 0.3
	Rha"-(H1)	Rha'-(H5)	4.4 ± 0.1		Rha"-(H1)	Rha'-(H5)	4.3 ± 0.2
	Rha"-(H2)	Rha'-(H3)	4.1 ± 0.3		Rha'"-(H1)	Rha"-(H4)	2.5 ± 0.3
	Rha"-(H2)	Rha'-(H4)	4.3 ± 0.2		Rha'"-(H1)	Rha"-(H5)	4.4 ± 0.1
	Rha'"-(H1)	Rha"-(H3)	3.4 ± 0.2		-	-	-
	Rha'"-(H2)	Rha"-(H3)	4.1 ± 0.3		-	-	-

* ROESY contacts were obtained from previously published NMR Data [1].

2.3. Docking on COX

Since ipomotaoside A binding to COXs is not yet determined [1], docking calculations were performed on the enzymes' two catalytic sites, pointing to a better binding to the peroxidase cleft. The binding energy for ipomotaoside on cyclooxygenase site was extremely positive, suggesting a lack of binding to this region. This result reinforces the originality of this resin glycosides scaffold, since the activity of most non-steroidal anti-inflammatory drugs in therapeutic use modulates the cyclooxygenase site. Also, as no crystallographic structure of COXs is available complexed to compounds modulating the peroxidase site, its biological substrate, PGG_2, was docked for comparison and validation.

Accordingly, PGG_2 (Figure 4 and Supporting Information, Figure S7) demonstrated an orientation at peroxidase site in agreement with the catalytic mechanism of the enzyme, interacting directly with heme through PGG_2 hydroperoxide. Such an orientation is essential for PGG_2 to be reduced to PGH_2, and exert its role on inflammatory processes [6], reinforcing the adequacy of the employed docking proceedings.

Figure 4. Complexes obtained for PGG_2 (**A**,**C**) and ipomotaoside 1 (**B**,**D**) with COX-1 as derived from docking calculations. Heme group is highlighted in yellow. 2D images, generated with the PoseView server [17], present only interactions between the ligand and amino acid residues. Common amino acid residues between PGG_2-COX-1 are indicated in red.

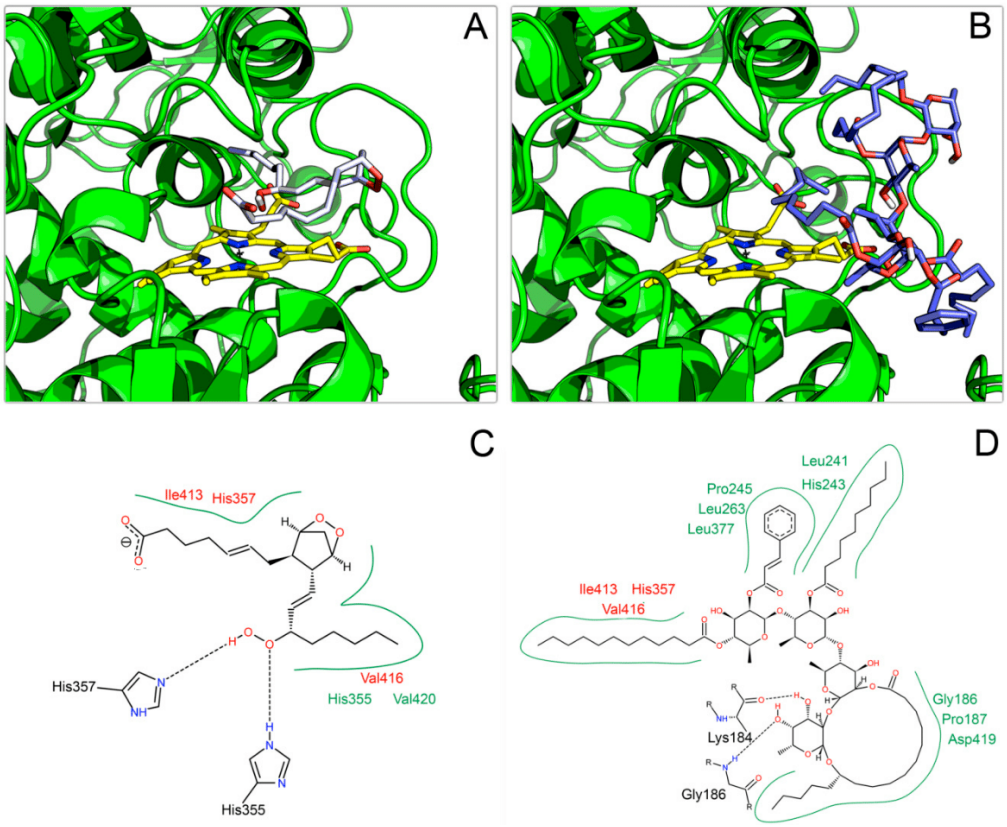

Like PGG_2, ipomotaoside A demonstrated a direct interaction between heme and an acyl chain on both COX-1 and COX-2 (Figure 4 and Supporting Information, Figure S7), suggesting that this acyl group is the main responsible for the pharmacological effect of ipomotaoside A. Additionally, hydrophobic amino acids residues from peroxidase site, participating in PGG_2binding, also interact with ipomotaoside (Figure 4 and Supporting Information, Figure S7), emphasizing the similarity of both molecules' mechanism of interaction with the target enzyme.

3. Experimental

3.1. Nomenclature, Topologies and Software

The recommendations and symbols of nomenclature as proposed by IUPAC [18] were used. The relative orientation of a pair of contiguous carbohydrate residues was described by two torsional angles at the glycosidic linkage, Φ and Ψ, for α-L-Rha-(1→2)-β-D-Fuc and α-L-Rha-(1→4)-α-L-Rha, as shown below:

- α1→2:

$\Phi = O5 - C1 - O1 - C2'$

$\Psi = C1 - O1 - C2' - C1'$

- α1→4:

$\Phi = O5 - C1 - O1 - C4'$

$\Psi = C1 - O1 - C4' - C3'$

Initially, the disaccharide structures were built using MOLDEN, [19] and the topologies of saccharide residues and ipomotaosides were generated by the PRODRG server [20]. Structures were manipulated using PyMOL [21]. Simulations and analyses were performed using GROMACS [22] simulation suite, version 4.5.1, and the GROMOS96 43a1 [23] force field, while metadynamics calculations [24] were performed using a modified version of GROMACS 4.5.1 interfaced with the PLUMED plugin package, version 1.2.2 [25]. The free energy surfaces were obtained through *sum_hills* tool from PLUMED package.

3.2. Topology Construction

Each ipomotaoside was built with the most prevalent conformations of its minimal components in solution (disaccharides). All compounds were built using MOLDEN and submitted to the PRODRG server to receive their crude topologies and atomic coordinates. HF/6-31**-derived Löwdin atomic charges, from previous studies [26], and improper dihedrals for maintenance of the conformational states of the monosaccharides α-L-rhamnose ($^{1}C_4$), and β-D-fucose ($^{4}C_1$), were included. Additionally, proper dihedral angles were included according to the GROMOS96 force field. Pyridine solution values were retrieved from the literature [12].

3.3. Metadynamics

Metadynamics calculations for the isolated disaccharides consisted of 10 ns MD simulations, employing a height of 0.1 for the Gaussian height, and a σ of 0.5 to each of the θ and φ angular coordinates of Cremer and Pople [27].

3.4. MD Simulations

Each minimum energy conformation of disaccharides, obtained from the metadynamics, as well as the complete ipomotaosides, was submitted to MD simulations in pyridine and water (SPC water model) [28] in a triclinic box using periodic boundary conditions. Counterions (Na^{+}) were added to neutralize the system charge when necessary. The systems were submitted to energy minimization by steepest Descents algorithm and subsequently to MD simulations. The Lincs method [29] was applied to constrain covalent bond lengths, allowing an integration step of 2 fs. The particle mesh Ewald method [30] was applied in the calculation of electrostatic interactions. Temperature and pressure were kept constant by coupling ipomotaosides (or carbohydrates), ions, and solvent to external temperature and pressure baths, with coupling constants of $\tau = 0.1$ and 0.5 ps, respectively. Finally, the simulations were performed at the constant temperature of 310 K for 0.1 μs.

3.5. ROESY Signals

ROESY ^{1}H-NMR data for compounds **1**–**4** [1] was employed to validate the intra-molecular H-H contacts observed on the performed simulations. The present work is based on a united-atom force field, which significantly reduce the computational costs, thus allowing faster simulations with longer time scales. Thus, to allow a comparison of the simulations to ROESY data, nonpolar hydrogens atoms were added to frames retrieved from trajectories, at every 10 ps, for each ipomotaoside. The correct geometry and hybridization were respected, and the obtained models were used to calculate the average interproton distances from simulations.

3.6. Docking Procedures

Docking calculations were performed with Autodock, version 4.2 [31]. COXs from PDB IDs 1Q4G and 1CVU were used. PGG_2 was built as described for ipomotaosides. Water molecules were removed prior to docking procedures. The Lamarckian Genetic Algorithm (LGA) was used to explore the binding sites. For each run, a maximum number of energy evaluations was set to 250,000,000, and a maximum number of 27,000 LGA operations was generated on populations of 10 individuals. In the current work 100 runs were performed, in a population of 1,000 individuals for each ligand. Crossover, mutation, and elitism were set to 0.80, 0.02, and 1, respectively. All rotatable dihedral angles of hydrophobic chains were treated as flexible, while Φ and Ψ dihedral angles of disaccharides were maintained rigid in the most abundant conformational states. The orientations of ipomotaosides and PGG_2 at the binding site were selected from docked conformations as representative of the lower energy clusters generated by Autodock. The bidimensional images were generated with the PoseView server [17].

4. Conclusions

In the present study, ipomotaosides A to D had their tridimensional structures obtained from the most abundant conformational states of their glycosidic linkages. These compounds were submitted to refinement under MD simulations in both aqueous and nonaqueous solvents and were compared to experimental data. A minor influence of pyridine on the compounds dynamic was observed, which reinforces the validity of the previously described NMR data for the understanding of ipomotaosides' behavior under biological conditions. The reproduction of inteproton ROESY contacts during unrestrained simulations on pyridine solvent suggests a precise conformational characterization of these flexible molecules, offering solution representative geometries for docking calculations. The so- obtained complexes pointed to ipomotaoside A as an inhibitor of the COX enzymes' peroxidase site, in a similar binding to that of PGG_2, providing a structural basis for future studies aiming at optimization of ipomotaosides as potential new anti-inflammatory agents.

Supplementary Materials

Supplementary materials can be accessed at: http://www.mdpi.com/1420-3049/19/4/5421/s1.

Acknowledgments

This work was supported by Conselho Nacional de Desenvolvimento Científico e Tecnológico (CNPq), MCT, by Coordenação de Aperfeiçoamento de Pessoal de Nível Superior (CAPES), MEC, Brasília, DF, Brazil, and the Fundação de Amparo à Pesquisa do Estado do Rio Grande do Sul (FAPERGS).

Author Contributions

H. V. conceived the computational study. P. R. A. developed the atomic models of ipomotaosides and performed molecular dynamics and analysis. L. G. S. and P. R. A. performed the docking calculations and analysis. C. S. G and P. R. A. performed the analysis of ^{1}H NMR Spectroscopic Data of compounds **1**–**4**. All authors read and approved the manuscript.

Conflicts of Interest

The authors declare no conflict of interest.

References

1. Yoshikawa, K.; Yagi, C.; Hama, H.; Tanaka, M.; Arihara, S.; Hashimoto, T. Ipomotaosides A-D, resin glycosides from the aerial parts of Ipomoea batatas and their inhibitory activity against COX-1 and COX-2. *J. Nat. Prod.* **2010**, *73*, 1763–1766.
2. Li, S.Z. *Min Dynasty, Compendium of Materia Medica*; Medical Publishing House: Beijing, China, 1999; p. 1501.
3. Corona-Castañeda, B.; Pereda-Miranda, R. Morning glory resin glycosides as modulators of antibiotic activity in multidrug-resistant Gram-negative bacteria. *Planta Med.* **2012**, *78*, 128–131.
4. Figueroa-González, G.; Jacobo-Herrera, N.; Zentella-Dehesa, A.; Pereda-Miranda, R. Reversal of multidrug resistance by morning glory resin glycosides in human breast cancer cells. *J. Nat. Prod.* **2012**, *75*, 93–97.
5. Pereda-Miranda, R.; Rosas-Ramírez, D.; Castañeda-Gómez, J. Resin glycosides from the morning glory family. In *Progress in the Chemistry of Natural Products*; Kinghorn, D.A., Falk, H., Kobayashi, J., Eds.; Springer: New York, NY, USA, 2010; Volume 92, pp. 77–153.
6. Smith, W.L.; Garavito, R.M.; DeWitt, D.L. Prostaglandin Endoperoxide H Synthases (Cyclooxygenases)-1 and -2. *J. Biol. Chem.* **1996**, *271*, 33157–33160.
7. Rencurosi, A.; Mitchell, E.P.; Cioci, G.; Pérez, S.; Pereda-Miranda, R.; Imberty, A. Crystal Structure of Tricolorin A: Molecular Rationale for the Biological Properties of Resin Glycosides Found in Some Mexican Herbal Remedies. *Angew. Chem. Int. Ed.* **2004**, *43*, 5918–5922.
8. Woods, R.J. Computational carbohydrate chemistry: What theoretical methods can tell us. *Glycoconj. J.* **1998**, *15*, 209–216.
9. Dwek, R.A. Glycobiology: Toward Understanding the Function of Sugars. *Chem. Rev.* **1996**, *96*, 683–720.
10. Pérez, S.; Mulloy, B. Prospects for Glycoinformatics. *Curr. Opin. Struct. Biol.* **2005**, *15*, 517–524.

11. Pol-Fachin, L.; Fernandes, C.L.; Verli, H. GROMOS96 43a1 performance on the characterization of glycoprotein conformational ensembles through molecular dynamics simulations. *Carbohydr. Res.* **2009**, *344*, 491–500.
12. Pedebos, C.; Pol-Fachin, L.; Verli, H. Unrestrained conformational characterization of *Stenocereus eruca* saponins in aqueous and nonaqueous solvents. *J. Nat. Prod.* **2012**, *75*, 1196–1200.
13. Pol-Fachin, L.; Serrato, R.V.; Verli, H. Solution conformation and dynamics of exopolysaccharides from *Burkholderia* species. *Carbohydr. Res.* **2010**, *345*, 1922–1931.
14. Castro, M.O.; Pomin, V.H.; Santos, L.L.; Vilela-Silva, A.C.E.S.; Hirohashi, N.; Pol-Fachin, L.; Verli, H.; Mourao, P.A.S. A Unique 2-Sulfated β-Galactan from the Egg Jelly of the Sea Urchin Glyptocidaris crenularis Conformation Flexibility Versus Induction of the Sperm Acrosome Reaction. *J. Biol. Chem.* **2009**, *284*, 18790–18800.
15. Pol-Fachin, L.; Verli, H. Effects of glycosylation on heparin binding and antithrombin activation by heparin. *Carbohydr. Res.* **2008**, *343*, 1435–1445.
16. Jiang, Z.; Geyer, A.; Schmitd, R.R. The Macrolidic Glycolipid Calonyctin A, a Plant Growth Regulator: Synthesis, Structural Assignment, and Conformational Analysis in Micellar Solution. *Angew. Chem. Int. Ed.* **1995**, *34*, 2520–2524.
17. Stierand, K.; Maaß, P.; Rarey, M. Molecular complexes at a glance: Automated generation of two-dimensional complex diagrams. *Bioinformatics* **2006**, *22*, 1710–1716.
18. Horton, D. Nomenclature of carbohydrates. *Pure Appl. Chem.* **1996**, *68*, 1919–2008.
19. Schaftenaar, G.; Noordik, J.H.J. Molden: A pre- and post-processing program for molecular and electronic structures. *Comput.-Aided Mol. Des*. **2000**, *14*, 123–134.
20. Schuettelkopf, A.W.; van Aalten, D.M.F. PRODRG: A tool for high-throughput crystallography of protein-ligand complexes. *Acta Crystallogr.* **2004**, *D60*, 1355–1363.
21. DeLano, W.L. *The PyMOL Molecular Graphics System*; DeLano Scientific LCC: San Carlos, CA, USA, 2002.
22. Van der Spoel, D.; Lindahl, E.; Hess, B.; Groenhof, G.; Mark, A.E.; Berendsen, H.J. GROMACS: Fast, flexible, and free. *J. Comput. Chem.* **2005**, *26*, 1701–1718.
23. Scott, W.R.P.; Hünenberger, P.H.; Tironi, I.G.; Mark, A.E.; Billeter, S.R.; Fennen, J.; Torda, A.E.; Huber, T.; Krüger, P.; van Gunsteren, W.F. The GROMOS biomolecular simulation program package. *J. Phys. Chem. A* **1999**, *103*, 3596–3607.
24. Barducci, A.; Bonomi, M.; Parrinello, M. Metadynamics. *WIREs Comput. Mol. Sci.* **2011**, *1*, 826–843.
25. Bonomi, M.; Branduardi, D.; Bussi, G.; Camilloni, C.; Provasi, D.; Raitieri, P.; Donadio, D.; Marinelli, F.; Pietrucci, F.; Broglia, R.A.; *et al*. PLUMED: A portable plugin for free energy calculations with molecular dynamics. *Comput. Phys. Commun.* **2009**, *180*, 1961–1972.
26. Verli, H.; Guimarães, J.A.A. Molecular dynamics simulation of a decasaccharide fragment of heparin in aqueous solution. *Carbohydr. Res.* **2004**, *339*, 281–290.
27. Cremer, D.; Pople, J.A. A General Definition of Ring Puckering Coordinates. *J. Am. Chem. Soc.* **1975**, *97*, 1354–1358.
28. Berendsen, H.J.C.; Grigera, J.R.; Straatsma, T.P.J. The missing term in effective pair potentials. *Phys. Chem*. **1987**, *91*, 6269–6271.
29. Hess, B.; Bekker, H.; Berendsen, H.J.C.; Fraaije, J.G.E.M. LINCS: A linear constraint solver for molecular simulations. *J. Comput. Chem.* **1997**, *18*, 1463–1472.

30. Darden, T.; York, D.; Pedersen, L. Particle mesh Ewald: An N·log(N) method for Ewald sums in large systems. *J. Chem. Phys.* **1993**, *98*, 10089–10092.
31. Morris, G.M.; Huey, R.; Lindstrom, W.; Sanner, M.F.; Belew, R.K.; Goodsell, D.S.; Olson, A.J. AutoDock4 and AutoDockTools4: Automated docking with selective receptor flexibility. *J. Comp. Chem.* **2009**, *16*, 2785–2791.

Sample Availability: Not available.

9.2 APÊNDICE B

2´,3´-Dialdehyde of ATP, ADP, and Adenosine Inhibit HIV-1 Reverse Transcriptase and HIV-1 Replication.

Schachter J, Valadão ALC, Aguiar RS, Barreto-de-Souza V, Rossi AD, **Arantes PR**, Verli H, Quintana PG, Heise N, Tanuri A, Bou-Habib DC, Persechini PM.

Current HIV Research, 2014, 12, 301-308.

Current HIV Research, 2014, *12*, 301-308

2′,3′-Dialdehyde of ATP, ADP, and Adenosine Inhibit HIV-1 Reverse Transcriptase and HIV-1 Replication

Julieta Schachter[*,1,2], Ana Luiza Chaves Valadão[3], Renato Santana Aguiar[3], Victor Barreto-de-Souza[4], Atila Duque Rossi[3], Pablo Ricardo Arantes[6], Hugo Verli[6], Paula Gabriela Quintana[5], Norton Heise[5], Amilcar Tanuri[3], Dumith Chequer Bou-Habib[4] and Pedro Muanis Persechini[2,5]

[1]Instituto de Biofísica, Carlos Chagas Filho (IBCCF), Universidade Federal do Rio de Janeiro, Polo de Xerem, RJ, Brasil; [2]Instituto Nacional de Ciência e Tecnologia para Pesquisa Translacional em Saúde e Ambiente na Região Amazônica (INPeTAm), Conselho Nacional de Desenvolvimento Científico e Tecnológico, Brasil; [3]Departmento de Genética, Instituto de Biologia, Universidade Federal do Rio de Janeiro, RJ, Brasil; [4]Laboratório de Pesquisa sobre o Timo, Instituto Oswaldo Cruz, Fundação Oswaldo Cruz, Rio de Janeiro, RJ, Brasil; [5]Instituto de Biofísica, Carlos Chagas Filho (IBCCF), Universidade Federal do Rio de Janeiro, RJ, Brasil; [6]Centro de Biotecnologia, Universidade Federal do Rio Grande do Sul, RS, Brasil

Abstract: The 2′3′-dialdehyde of ATP or oxidized ATP (oATP) is a compound known for specifically making covalent bonds with the nucleotide-binding site of several ATP-binding enzymes and receptors. We investigated the effects of oATP and other oxidized purines on HIV-1 infection and we found that this compound inhibits HIV-1 and SIV infection by blocking early steps of virus replication. oATP, oxidized ADP (oADP), and oxidized Adenosine (oADO) impact the natural activity of endogenous reverse transcriptase enzyme (RT) in cell free virus particles and are able to inhibit viral replication in different cell types when added to the cell cultures either before or after infection. We used UFLC-UV to show that both oADO and oATP can be detected in the cell after being added in the extracellular medium. oATP also suppresses RT activity and replication of the HIV-1 resistant variants M184V and T215Y. We conclude that oATP, oADP and oADO display anti HIV-1 activity that is at in least in part due to inhibitory activity on HIV-1 RT.

Keywords: HIV-1, macrophage, oxidized adenosine, oxidized ADP, oxidized ATP, reverse transcriptase.

INTRODUCTION

HIV-1 infects $CD4^+$ T lymphocytes, monocyte/macrophages and dendritic cells through interaction of the viral envelope glycoprotein gp120/41 with the CD4 molecule and the chemokine receptors CCR5 or CXCR4 [1]. After entry into a target cell, the HIV-1 RNA genome must be retrotranscribed into an integration-competent double stranded DNA. This step is catalyzed by the HIV-1 reverse transcriptase (RT) enzyme, which has DNA- and RNA-dependent DNA polymerase and RNase H activities. Nowadays, the highly active antiretroviral therapy (HAART), which comprises the use of inhibitors of RT and viral protease, is the most efficient chemotherapy against HIV-1 infection [2-4].

Ideally, an antiretroviral agent should fulfill several requirements, such as to act directly on the virion, act at the replication stages prior to integration of viral DNA into the infected host cell genome, be absorbed by uninfected cells in order to provide a barrier to infection through residual active virions, and finally, be effective at non cytotoxic concentrations readily attainable *in vivo* [5]. RT inhibitors are characterized in two classes: the nucleoside/nucleotide analogue reverse transcriptase inhibitors (NRTIs) and the non-nucleoside reverse transcriptase inhibitors (NNRTIs) [6]. NRTIs compete with the deoxynucleoside triphosphates (dNTPs) during DNA synthesis and act as chain terminators. On the other hand, NNRTIs are noncompetitive inhibitors that bind to allosteric binding sites of HIV-1 RT [7]. Thus, design of novel compounds that can inhibit wild type and drug resistant HIV-1 RTs is a subject of major interest in the field of antiretroviral research.

The 2′,3′ dialdehyde of ATP or oxidized ATP (oATP) is a compound largely known as a specific label for the nucleotide binding site of several ATP-requiring enzymes, since oxidative cleavage of the bond between C-2' and C-3' of the ribose ring generates a 2',3'-dialdehyde derivative that forms covalent bonds with the side chain amino group of lysine residues present at the ATP-binding sites [8]. oATP was originally used to modify and/or label ATP-binding sites in a variety of purified proteins, including pyruvate carboxylase [8], adenylate cyclase [9], histone kinase [10], tryptophanyl-tRNA synthetase [11], sarcoplasmic/endoplasmic reticulum Ca^{2+}-ATPase (SERCA) [12], and Na^+, K^+- ATPase [13]. Later studies showed that oATP is an antagonist of the purinergic receptor P2X7 [14] and since then it has been widely used to study P2X7 associated phenomena *in vivo* and *in vitro* [15-17].

Interestingly, in recent studies extracellular ATP and nucleotide (P2) receptors have been involved in HIV-1 infection [18-20]. Some of those studies show that oATP inhibits different sets of P2 receptors and blocks HIV-1

*Address correspondence to this author at the Instituto de Biofísica, Carlos Chagas Filho (IBCCF), Universidade Federal do Rio de Janeiro, Polo de Xerem, RJ, Brasil; Tel: +55-21-3938-6560; Fax: +55-21- 2280-8193; E-mail: julieta@biof.ufrj.br

1570-162X/14 $58.00+.00

infection; however, its action has not been related to RT activity [19, 20].

Here we report that oATP inhibits HIV-1 replication by blocking the early steps of virus replication. The antiretroviral effect of oATP was evaluated in HIV-1 indicator cells (GHOST R3/X4/R5) and in primary human macrophages. We further show that oATP, oxidized ADP (oADP), and oxidized Adenosine (oADO) inhibit natural endogenous RT activity (NERT) in isolated virus particles. oATP also inhibits replication of two HIV-1 mutants resistant to multiple NRTIs, opening new possibilities for the development of a new class of anti HIV-1 compounds.

MATERIALS AND METHODS

Cell culture and Reagents. Human monocyte-derived macrophages were obtained from peripheral blood mononuclear cells (PBMC) isolated by density gradient centrifugation (Hystopaque -Sigma-Aldrich, St. Louis, MO, USA) from buffy coat preparations of healthy blood donors, through adherence onto plastic plates, as previously described [21]. Briefly, PBMCs were plated in culture plates (Corning, MA, USA) in Dulbecco's modified Eagle's medium (DMEM, LGC Bio, SP, Brazil) supplemented with 10% human serum (Sigma-Aldrich) and penicillin/streptomycin (Sigma-Aldrich). Cells were maintained for 7 days for monocyte differentiation into macrophages. Non-adherent cells were washed out. The purity of macrophages was ≥ 94% as determined by flow cytometry (FACScanto, BD Becton, Dickinson and Company, NJ, USA) with the use of anti-CD68 labeled antibodies (Santa Cruz Biotechnology, Santa Cruz, CA, USA). The HEK-293T cells were cultured in the same conditions. GHOST cell line was obtained through the NIH AIDS Research and Reference Reagent Program (GHOST R3/X4/R5, Catalog Number 3943) from Dr. Vineet N. Kewal Ramani and Dr. Dan R. Littman as described [22]. The expression of CCR3, CXCR4 and CCR5 was maintained by adding hygromycin (100 μg/ml), Geneticin (500 μg/ml), and puromycin (1 μg/ml) to the culture medium. oATP, oADP and oADO (Sigma-Aldrich) was diluted in saline solution (pH 7.4). The NNRTI efavirenz (EFV) and the NRTI 2', 3'-dideoxy-3'-thiacytidine (3TC) were obtained from the AIDS Research and Reference Reagent Program, NIH. These drugs were suspended in dimethyl sulfoxide (DMSO) (Merck, Darmstadt, Germany). All experimental solutions tested negative to the presence of endotoxin/LPS using a Limulus amoebocyte assay (LAL) kit (LONZA, Basel, Switzerland).

Plasmids. HIV-1 proviral plasmids pNL4-3 Luc (HIV-1 subtype B) has already been described [23]. The full-length, envelope-defective SIVmac239 reporter virus (pSIVmac Luc E–R–) was kindly provided by Dr. Nathaniel Landau [24]. The envelope-defective HIV reporter virus (pNL4-3 Luc.R-E-) was obtained from NIH AIDS Research and Reference Reagent Program (Catalog Number 3418). Both HIV-1 proviral clones encoded luciferase in place of the *nef* gene. Reporter viruses lacking *env* gene were generated as vesicular stomatitis virus glycoprotein (pVSV-G) pseudotypes. NL4-3 Luc M184V mutant was generated by introducing the M184V mutation at the RT with QuikChange Site-Directed Mutagenesis kit (Strategene, La Jolla, CA, USA), following the manufacturer's instructions. This mutation is known to decrease the susceptibility of HIV-1 to the NRTIs 3TC and abacavir [25]. The following primers were used in this site-directed mutagenesis: M184V (F) – 5' -TATCTATCAATACGTGGATGATTTGTAT-3' and M184V (R) 5'-ATACAAATCATCCACGTATTGATAGATA-3'; T215Y (F) 5'-GTTGAGGTG GGGATTTTACACACCA GACAAAAAACATC-3' and T215Y (R) 5'-GATGTTTTTT GTCTGGTG TGTAAAATCCCCACCTCAAC-3'. Both constructs were sequenced and checked by digestion mapping to confirm the presence of the desired mutation and plasmid integrity.

Virus isolates. All infection assays of human primary macrophages were performed with CCR5-dependent isolate HIV-1Ba-L (donated by the AIDS Research and Reference Reagent Program, NIH). To produce virus stocks, HIV-1 Ba-L was expanded in phytohemagglutinin (5 μg/mL)-activated PBMCs cultivated with 5 U/mL of recombinant human IL-2 (Sigma-Aldrich), as described [21]. We also used pseudotyped HIV Δ*env* viruses with vesicular stomatitis virus envelope glycoprotein (VSV-G). Full-length HIV virus stocks (NL4-3 Luc) were generated by transient transfection of HEK-293T cells using Lipofectamine-2000 protocols in OptiMEM medium (Invitrogen). To produce pseudotyped viral stocks, the *env* deleted HIV (pNL4-3 Luc.R-E-) was transfected with equal proportions of VSV-G envelope expressing vector (pVSV-G) following the above described procedure. This pseudptyped virus will be thereafter referred to as HIV Δenv Luc. Culture supernatants were harvested 48 h after transfections, and filtered through a 0.22 μM pore size filter to remove cell debris. Virus production was evaluated in cell culture supernatants using a commercial ELISA kit against p24 virus antigen according to manufacturer's instructions (ZeptoMetrix Corp, Buffalo, NY, USA).

Determination of Cell Viability. The effect of oATP on GHOST cell viability was assessed using a CellTiter-Blue Cell viability Assay, according to the manufacturer´s protocol (Promega, Madison, WI, USA). Briefly, cells were exposed to increasing concentrations of oATP. After 48 h incubation, CellTiter-Blue reagents were added and the plates were incubated overnight. The fluorescence values were measured with CytoFluor 4000 plate reader (Applied Biosystems). The cell viability was calculated relative to the percentage of control cells not treated with oATP.

Virus Infection and oATP antiretroviral activity. Macrophages were infected with the HIV-1 CCR5-dependend isolate Ba-L using 5 to 10 ng/mL of p24 antigen in the presence or not of oxidized purines. After 4 h incubation, cells were washed to remove non-internalized viruses. HIV-1 infectivity was evaluated in cell culture supernatants or in cell lysates using a commercial ELISA kit for HIV-1 p24 antigen, according to manufacturer's instructions (ZeptoMetrix). To measure the amount of intracellular HIV-1, infected macrophages were washed twice with PBS at day 10 post-infection, treated with Trypsin (1 BTEE unit/mL, Sigma) to release adsorbed viruses and lysed with Triton X100 (1%). Then, virus production was evaluated as above. In another set of experiments, oATP was added to macrophages 3 h before or after HIV-1 infection. NL4-3 Luc virus (5 ng/ml of p24 antigen) were used to infect GHOST cells in the presence of increasing

concentrations of oATP. Cells were lysed in CAT lysis buffer (Promega) 48 h later, and, after removing the nuclei, the cytosolic fraction was used to determine the luciferase activity (Luciferase assay kit, Promega). To evaluate oATP impact in HIV DNA synthesis, GHOST cells were infected with NL4-3 Luc virus (RLU production of 5 Log) in the presence of oATP 100 µM. The virus aliquots were previously treated with DNAse to rule out any DNA plasmid contamination. 12 h post infections the cells were washed with PBS, collected by trypsin treatment and the DNA extracted using QIAamp DNA Mini Kit (QIAGEN) following the manufacturer's recommendations. The HIV-1 virus DNA was measured using quantitative PCR (qPCR) using the same primers and probes described in the follow section.

NERT assay based on PCR quantification. Natural Endogenous Reverse Transcriptase activity (NERT) was performed as previously described [26]. Briefly, aliquots of purified virus particles were incubated in DMEM supplemented with 20 U of DNase I (Invitrogen) and 10 mM of $MgCl_2$ for 60 min at 37°C in a final reaction volume of 25 µl. dNTPs (2.5 mM) were further added to each tube (except to the negative controls) in the presence of increasing concentrations of oATP. The reaction proceeded for 120 min at 37°C. This preincubation time is a requirement of the covalent bonds that oATP makes within ATP-binding sites and is a standard procedure when using oATP [8, 12, 14, 16]. Enzymatic activity was then terminated by the addition of 37.5 µl of a stop solution (10 mM Tris-HCl, pH 7.4, 10 mM EDTA, 20 mg/ml of sheared salmon sperm DNA (Sigma-Aldrich) 50 mg/ml of proteinase K (Sigma-Aldrich) and heated at 95°C for 10 min to lyse the virus particles. The amounts of newly synthesized double-stranded strong stop DNA (ssDNA) were measured by qPCR using combinations of the following HIV-1-specific oligonucleotides and probe: SSF1 (5'-GCTAACTAGGGAACCCACTGCTT-3'), SSR1 (5'-CAACAGACGGGCACACACTACT-3'), and ssDNA probe (5'-FAM-AGCCTCAATAAAGCTTGCCTTGAGTG CTTC-BHQ1-3′) [26]. Reaction mixtures were as follows: 1 µL Taqman Universal PCR mixture (Applied Biosystems, Foster City, CA), 0.25 pmol of each primer, 0.05 pmol ssDNA probe, 4 µl of NERT stopped reaction mixture in a final volume of 25 µl. Amplifications were performed with a model 7500 Sequence Detection System (Applied Biosystems). The cycle conditions were as follows: 50°C for 2 min, 95°C for 10 min, and 50 cycles at 95°C for 15 s and 60°C for 1 min. pNL4-3 proviral DNA was serially diluted in NERT stop solution and used as qPCR standard curves (dilutions were from 10^7 to 10^1 copies of DNA, and the detection limit of the assay was 10 initial template copies). Standard curves were used for the quantification of ssDNA. At least three dilutions of each sample were assayed, and data sets in which the linear correlation coefficient of the standard curve was less than 0.98 were not included for further analysis. EFV was used as inhibition control of NERT activity in purified viruses. Virus particles not exposed to dNTPs were used as NERT negative controls.

In vitro RT activity. We used the RT colorimetric assay (Roche, Basel, Switzerland) for the quantification of the inhibitory effect of oATP, oADP, and oADO on the HIV-1 RT activity *in vitro*. HIV-1 RT (2ng/µl) was incubated by 2 h with oATP, oADP or oADO and then incubated with the dNTPs by 1 h for the RT reaction. The inhibitory activity was calculated as the percent of inhibition as compared to a HIV-1 RT sample that does not contain any inhibitor. We used the non-nucleoside reverse transcriptase inhibitor EFV as a control of RT inhibition.

Intracellular detection of oxidized nucleotides by ultra-performance liquid chromatography analysis (UFLC–UV). GHOST cells were incubated with oADO or oATP (1 mM) by 3 h, washed two times with PBS, treated with trypsin and centrifuged. The pellet was resuspended in 40µl of 3M perchloric acid, incubated for 15 min at 0 °C and centrifuged. The supernatant was adjusted at pH 6.5 with 3.5 M NaOH/1M HCO_3 and centrifuged [27]. The supernatant was analyzed on an UFLC Shimadzu (Shimadzu, Japan), equipped with a vacuum degasser, a binary pump, manual injector and UV detector. C-18 Kromasil (250 mm×4.6 mm) was used for separation. Chromatographic conditions: mobile phase A, 100 mM H_3PO_4, pH adjusted with triethylamine to pH 6.2. The flow-rate was 1 ml/min and the column was operated at room temperature. Peaks were detected at 254 nm of UV detection. Retention times were assessed using standard samples of nucleotide.

Molecular Docking. The construction of oATP was performed with Molden [28], and the *ab initio* calculations were performed using GAMESS [29]. CHELPG atomic charges were employed for the ligand, obtained at the HF/6-31G** level. Docking procedures were realized with Autodock, version 4.2 [30]. The HIV-RT crystal structure complexed with AZTTP was used (PDB 3V4I), and the docking was centered in its binding site. The original ligand and water molecules were removed prior to docking procedures and only polar hydrogens were added. The Lamarckian Genetic Algorithm (LGA) [31] was used to explore the space of the binding site, centered on oATP site on RT-HIV. For each run, a maximum number of energy evaluations were set to 25,000,000, and a maximum number of 27,000 LGA operations were generated on populations of 10 individuals. A total of 100 runs were performed, and a population of 1000 individuals was employed. Crossover, mutation, and elitism were set to 0.80, 0.02, and 1, respectively. The orientation of oATP at the binding sites was selected from the lowest energy docked conformation generated by Autodock. The 2D images were generated with the PoseView server [32], and 3D images were performed using Pymol program [33].

Statistical analysis. Means were compared using the Mann Whitney's test and significance was assumed when P was less than 0.05(*) or 0.001(**). Computations were carried out using PRISM statistical software (GraphPad Software, Inc., version 5.01).

ETHICS STATEMENT

All experimental procedures involving human blood were performed with samples obtained after written informed consent and all procedures were approved by the Research Ethics Committee of the Oswaldo Cruz Foundation under the number 397-07.

RESULTS

oATP Inhibits Early Steps of HIV-1 Infection

To evaluate the effect of oATP on HIV-1 replication, we initially performed HIV-1 infection of GHOST cells with the HIV NL4-3 Luc virus. In this system, 100% luciferase activity indicates efficiently integrated viruses. Cells were infected with the HIV NL4-3 Luc virus in the presence of increasing concentrations of oATP for 5h. After washing to remove non-internalized viruses, cells were maintained in culture for 48 h, and the infectivity levels were evaluated by measuring luciferase activity of cell lysates. oATP treatment decreased HIV-1 infection by more than 80% at 100 µM, with an IC_{50} of 27.71 ± 0.03 µM (Fig. **1A**).

These data strongly suggest that oATP inhibits HIV-1 cycle either at the integration of the viral cDNA into the host DNA or at a previous step. Because this oxidized nucleotide was previously shown to inhibit HIV integrase *in vitro* [34], we decided to investigate its effect at a previous step: the synthesis of HIV-1 DNA. GHOST cells were infected with HIV NL4-3 Luc in the presence of 100 µM oATP and the viral DNA synthesis by HIV-1 RT was evaluated 12 h post-infection in the cell lysates by qPCR. The results showed that oATP inhibits HIV-1 DNA synthesis up to 95% (Fig. **1B**). We ruled out any cytotoxic effects of oATP treatment on the host cells, by showing that the viability of cells treated at the same concentrations of oATP in the absence of the virus remaining at 100 % (Fig. **1C**).

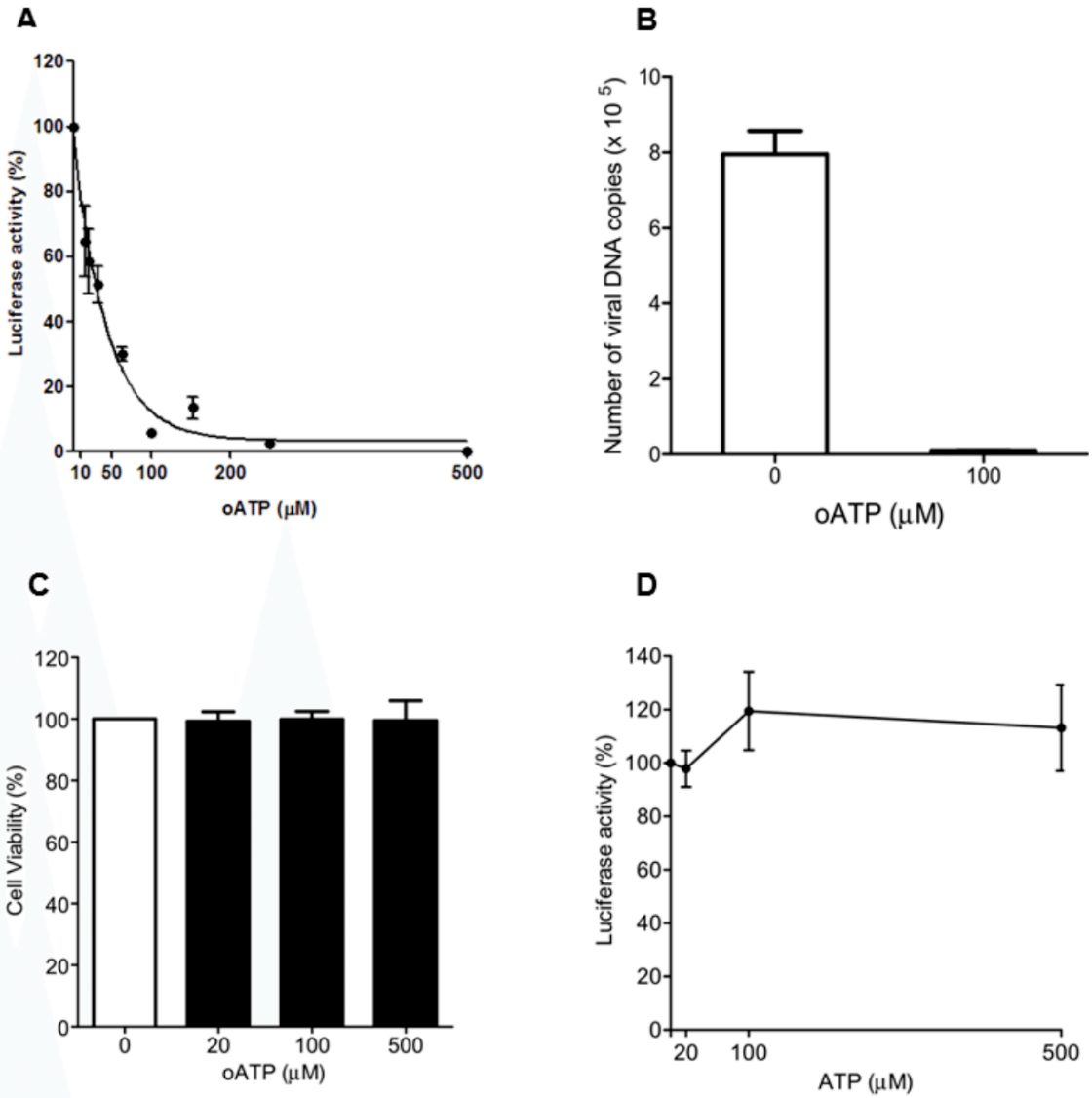

Fig. (1). oATP inhibits early steps of HIV-1 infection in GHOST cells. (**A**) GHOST cells were infected with NL4-3 Luc virus in the presence of indicated concentrations of oATP or (**D**) ATP, washed out, and 48 h later, the infectivity levels were evaluated measuring luciferase activity. (**B**) GHOST cells and virus were prepared as above in the presence or not of 100 µM oATP, washed out, and 12 h later the cells were lysed and cDNA extracted for the qPCR assays. (**C**) Viability of GHOST cells after incubation with oATP at indicated concentrations for 48 h, measured by a CellTiter-Blue assay. The results represent the means ± SD calculated from three independent experiments with triplicate samples and are expressed as percentages of untreated cells.

Because it was shown by others that ATP can bind to the p66 subunit of HIV-1 RT and modulate its enzymatic kinetic [35], we performed the same GHOST experiment in the presence of similar concentrations of ATP and evaluated the infectivity levels by measuring luciferase activity of cell lysates. In contrast with oATP, ATP treatment did not affect the HIV-1 infection (Fig. **1D**), suggesting that the lack of 3´-OH in oATP [36] is probably necessary for the inhibition of the infection.

oATP Also Blocks HIV Infection Even After Virus Entry

To better characterize the mechanism of action of oATP on HIV infection, we used pseudotyped HIV virus particles *env* deleted (Δenv) with vesicular stomatitis virus envelope glycoprotein (p NL4-3.Luc.R$^-$E$^-$ + pVSV-G). Since this pseudotyped virus enters by a process not mediated by gp120-CD4 receptor contact, this strategy allowed us to evaluate if oATP can block HIV-1 infection at a step after the entry process. As depicted in Fig. (**2**), oATP also inhibits infection of HIVΔenv Luc pseudotyped viruses. HIVΔenv Luc viruses that were not complemented with VSV-G envelope proteins were not infectious, as expected (not shown). This result suggested that oATP could block HIV infection after entry steps, since this compound still blocks the replication of pseudotyped viruses that bypass the initial steps to gain access to the cytoplasm. Higher concentrations of oATP were necessary to achieve the same levels of inhibition of HIV VSV-G pseudotyped viruses in comparison with HIV viruses. This can be explained by the different routes of cell entry considering that VSV-G pseudotyped viruses requires endocytosis and vesicle acidification.

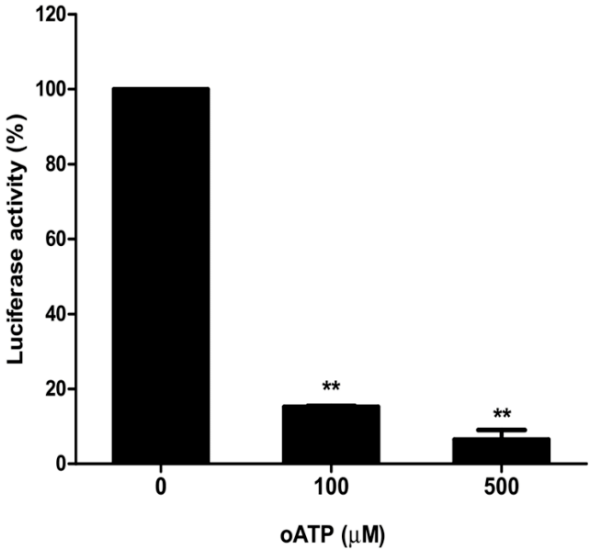

Fig. (2). oATP blocks HIV-1 infection even after virus entry. GHOST cells were infected for 5h with pseudotyped HIVΔenv Luc (pNL4-3 luc. R-E + pVSV-G) in the presence of indicated concentrations of oATP. Virus infection was estimated by measuring luciferase activity 48 h post-infection. The results represent the means ± SD calculated from three independent experiments with triplicate samples and are expressed as the percentage of untreated cells.

oATP Inhibits SIV Infection

To test whether oATP inhibitory effects are specific for HIV-1 or if it can also restrict the replication of other retrovirus infections, we infected GHOST cells with simian immunodeficiency virus macaques (SIVmac) that also harbor Luciferase reporter gene in the presence of increasing concentrations of oATP for 5h. As we can see in Fig. (**3**), oATP treatment decreased HIV-1 infection with an IC_{50} of 71.5 ± 0.03 μM, showing that, although less potently, oATP can inhibit other retroviruses.

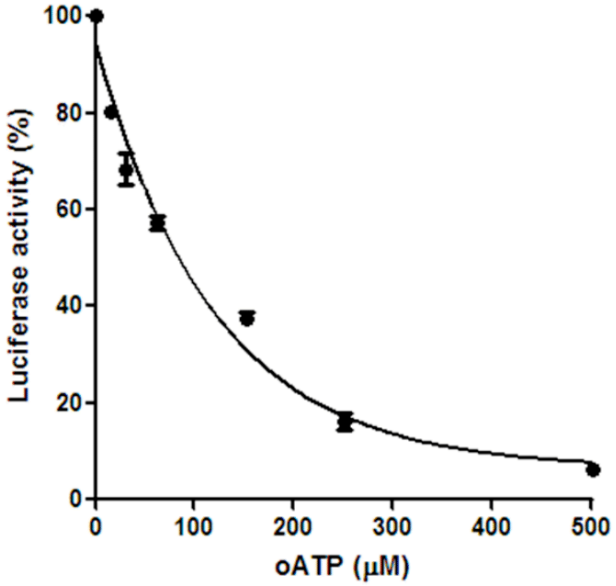

Fig. (3). oATP inhibits SIV infection in GHOST cells. GHOST cells were infected with SIVmac Luc virus in the presence of the indicated concentrations of oATP, washed out, and 48 h later the infectivity levels were evaluated measuring luciferase activity. The results represent the means ± SD calculated from three independent experiments with triplicate samples and are expressed as percentages of untreated cells.

Inhibition of HIV-1 RT by oATP, oADP and oADO

One important characteristic of NRTIs that allow them to act as chain terminators and inhibit DNA synthesis is the lack the ribose 3´-OH group. Since oATP also has a modification at the 3'position, we decided to investigate whether its antiretroviral effects could be due to a direct inhibition of the RT. In fact, using an *in vitro* RT colorimetric assay we showed that oATP inhibits 40% of HIV-1 RT activity at 10μM and 90% at 100 μM (Fig. **4**, black bars).

Next, we hypothesized if other oxidized nucleotides and nucleosides with the same 2', 3'-dialdehyde structure possibly have similar effects on HIV-1 RT. We observed that oADP, was also able to inhibit RT activity *in vitro* at a similar dose as oATP (Fig. **4**, gray bars). The oADO did not inhibit the RT activity (Fig. **4**, open bars).

We also asked whether oATP could directly act on HIV-1 RT activity of cell-free virus particles. In order to investigate this possibility we used the NERT [26]. The

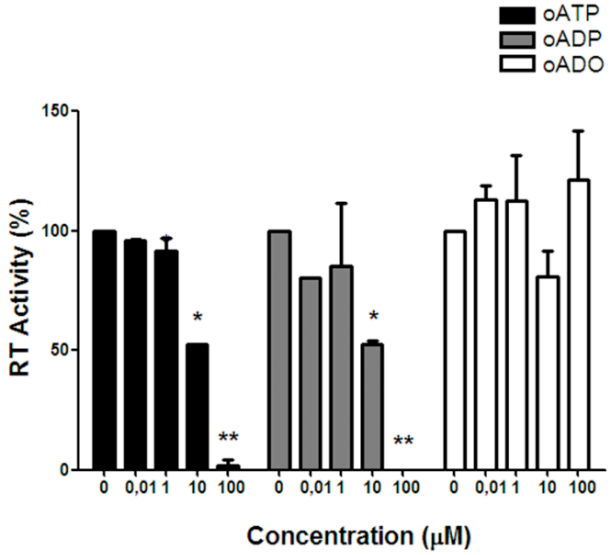

Fig. (4). oATP and oADP, but not oADO inhibit HIV-1 RT activity *in vitro*. The colorimetric assay was used to measure RT activity *in vitro*. Inhibitory activity of oATP, oADP and oADO was calculated as percent inhibition as compared to a HIV-1 RT sample (2ng/μl) that does not contain inhibitor. The results represent the means ± SD calculated from two independent experiments with triplicate samples and are expressed as the percentage of the activity of the untreated enzyme.

NERT assay is based on intravirion DNA synthesis by endogenous RT activity and it is made possible by the amphipathic domains of the gp41 transmembrane protein, which render the HIV-1 envelope permeable to a range of small molecules, such as dNTPs and Mg^{2+} [37]. HIV NL4-3 env gp120 virus particles were purified and incubated with dNTPs and different concentrations of oxidized purines. Following NERT reaction, newly synthesized DNA was extracted and the cDNA products were quantified by qPCR. The presence of oATP during NERT reaction significantly reduced the amount of cDNA synthesis compared with positive controls not exposed to oATP (Fig. **5A**, black bars). We also showed that both oADP and oADO were also able to inhibit NERT activity (Fig. **5A**, gray and white bars respectively). Control experiments using EFV showed that 90 % inhibition of RT activity was achieved at 1.25 μM (Fig. **5B**). These results suggested that oATP, oADP, and oADO can penetrate the virus envelope and inhibit intravirion RT activity. Consistent with these results, oADP and oADO also inhibited the replication of HIV-1 in GHOST cells (data not shown).

oADO and oATP Can Incorporate into the Cells and Phosphorylated/Dephosphorylated

The fact of oADO inhibits NERT activity but not *in vitro* RT activity suggested that the oADO molecule could be phosphorylated in the intracellular milieu or inside the virion. To test this possibility, GHOST cells were treated with oADO or oATP by 3 h, washed out and the cellular extracts analyzed by UFLC-UV (Fig. **6**). We observed that in the oADO treated cells both oADO and oATP could be detected in the cell extracts, showing that oADO can cross the plasma membrane and phosphorylated to oATP. On the other hand, when cell are treated with oATP, oATP and oADO can be detected in the cell extracts, indicating that this molecule can be dephosphorylated and transformed in other oxidized nucleotide derivatives.

oATP Inhibits HIV-1 Production in Primary Human Macrophages

To investigate further the efficacy of the antiretroviral effects of oATP directly in HIV-1 target cells, we infected

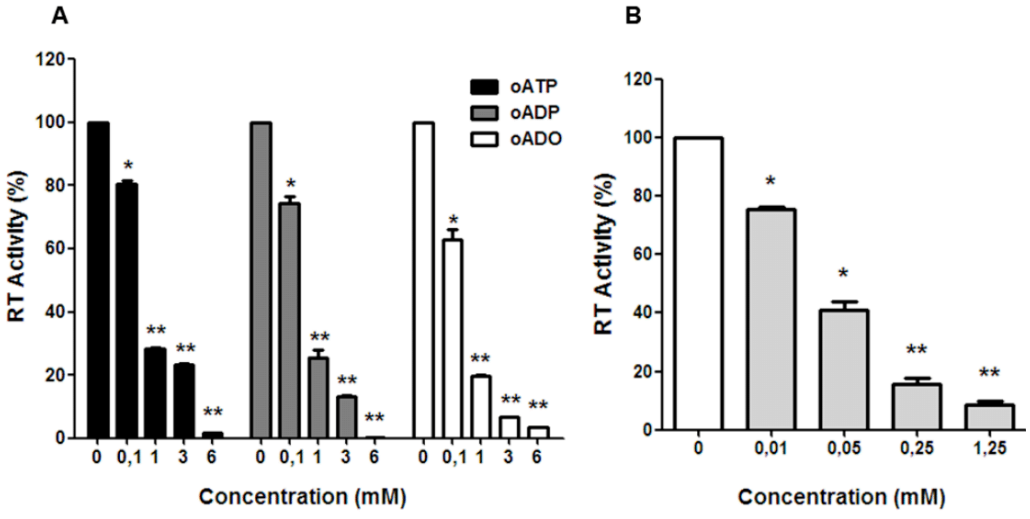

Fig. (5). oATP, oADP and oADO inhibit HIV-1 NERT activity. Aliquots of the NL4-3 virus were exposed to increasing concentrations of oxidized purines and the NERT activity was measured by qPCR. (**A**) Cell free virus particles were incubated with oATP, oADP and oADO before NERT assay. (**B**) As a positive control for NERT inhibition, cell-free virus was exposed to EFV. The absolute quantification of ssDNA synthesis was obtained by comparison with a DNA standard curve. A plasmid containing the NL4-3 infectious clone was serially diluted in the NERT stop solution (10^1 to 10^7 copies of DNA) and subjected to qPCR amplification. The results are expressed as a percentage of control and are means ± SD of triplicate experiments.

human primary monocyte-derived macrophages *in vitro* with HIV-1 Ba-L and oATP was added during (Fig. **7A**, **B**), 3 h before (Fig. **7C**) or immediately after (Fig. **7D**) viral entry. Cells infected in the absence of oATP were used as positive control of infection (100 % infectivity). The virus production was evaluated though measurement of the amount of p24 antigen in the extracellular medium.

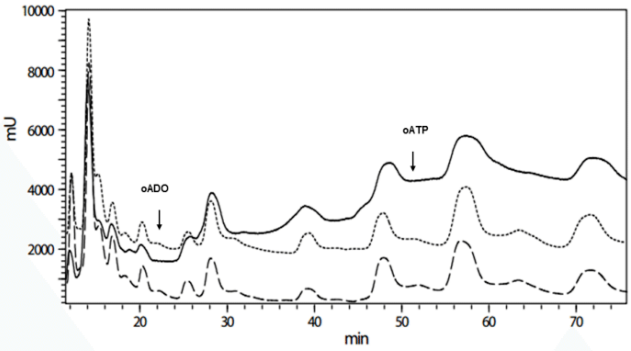

Fig. (6). oATP and oADO can be detected in the cell after extracellular treatment. GHOST cells were treated for 3 h with oADO (dot line), oATP (trace line) or nothing (black line) and the cell extract was analyzed on an UFLC. Arrows indicate peaks of oADO and oATP according to retention times corresponding to the standards.

We first observed that oATP inhibited HIV-1 replication in a dose-dependent manner reaching up to 80 % inhibition at 100 μM (Fig. **7A**). Similar results were observed when intracellular p24 production was measured (Fig. **7B**), indicating that there is indeed an inhibition of virus production inside the cell and not an inhibition of virion budding. These experiments were performed by exposing both the virus and macrophages to oATP during the initial 3 h period of interaction that include binding and entry on the cells [38]. To investigate further the effects of oATP in HIV-1 replication, we assessed the activity of this oxidized nucleotide on viral production by macrophages treated with oATP before infection with the virus. As depicted in Fig. (**6C**), the exposure to macrophages were treated for 3h with oATP after viral infection (Fig. **7D**).

Taken these results together, we can conclude that oATP can block HIV-1 infection in primary macrophages, and that direct oATP decreased viral replication in macrophages up to 90%. A similar result was observed when interaction between virus particles and the oATP is not required for the antiviral effect.

oATP Inhibits Replication of HIV-1 Variants Resistant to Multiple NRTIs

In the next step, we investigated whether oATP can be effective against HIV-1 variants that are resistant to NRTIs.

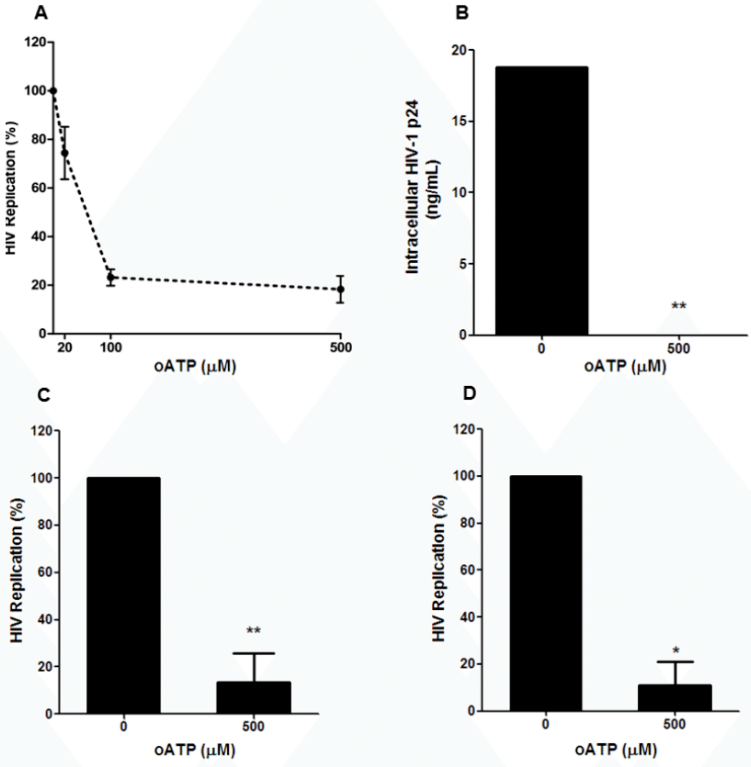

Fig. (7). oATP inhibits HIV-1 production in primary human macrophages. (**A-B**) Human monocyte-derived macrophages were infected by HIV-1 Ba-L in the presence of oATP at the indicated concentrations for 3 h. HIV-1 replication was evaluated after 10 days measuring p24 Ag on the culture supernatants (**A**) and cell lysates (**B**). (**C**) Macrophages were pre-treated, or not, with oATP 500 μM for 3 h, washed out and then infected with HIV-1. Virus replication was measured 10 days later. (**D**) Macrophages were infected with HIV-1 as in (**A**) in the absence of oATP. After washing, infected cells were treated for 2 h with oATP and HIV-1 replication was measured after 10 days. The mean of p24 concentration in HIV-1-infected cells cultured only with medium without oATP (100% virus production) was 147 ng/mL. Data represent means ± SD for 3 different donors, performed in duplicate.

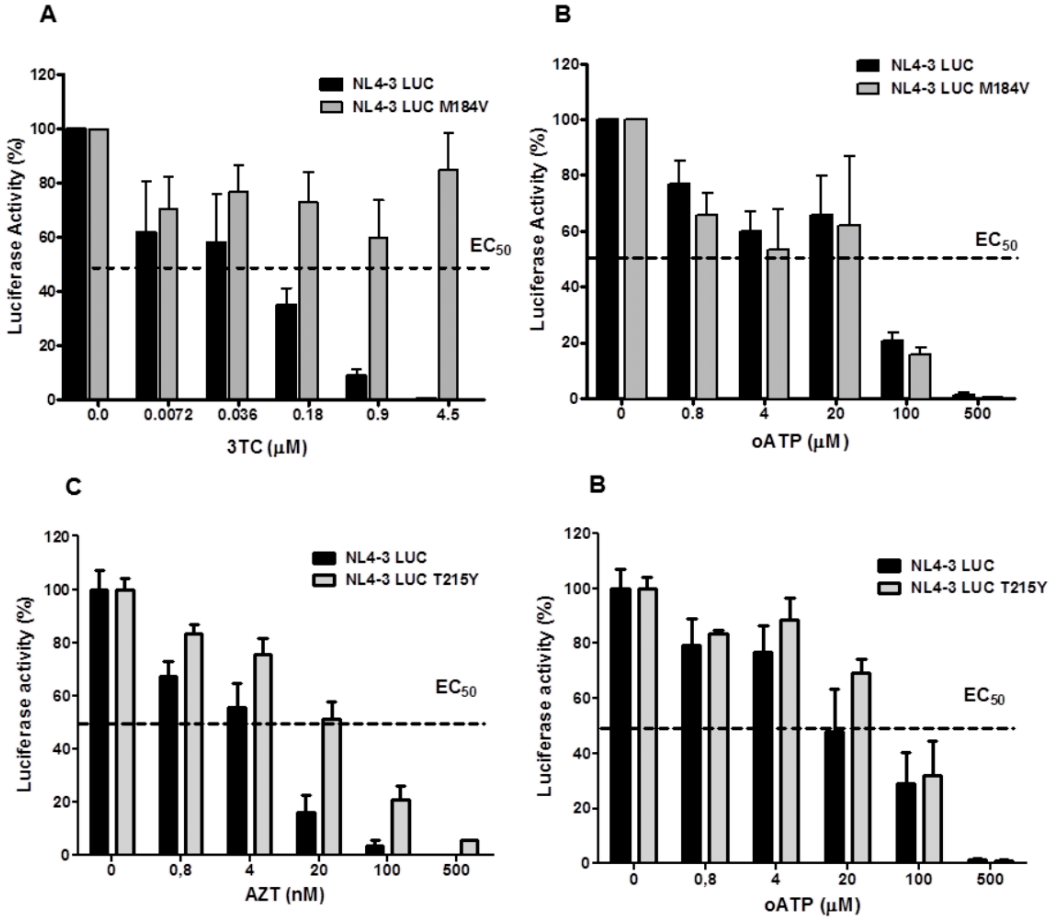

Fig. (8). oATP inhibits infectivity of mutant HIV-1 resistant to multiple NRTIs. GHOST cells were infected for 6 h with the same amount of NL4-3 Luc virus (black bars) or with M184V variant (grey bars) in the presence of increasing concentrations of 3TC (**A**) or oATP (**B**). In another series of experiments GHOST cells were infected during the same time with similar amount of NL4-3 Luc virus (black bars) or with T215Y variant (gray bars) in the presence of increasing concentrations of AZT (**C**) or oATP (**D**). The virus infectivity was evaluated by luciferase activity. The infectivity was normalized by the positive controls not exposed to drug treatment. All the results were obtained from two independent experiments with four replicates and the means and SD are shown. The IC_{50} line is represented in each graphic.

A NL4-3 Luc gp120 virus harboring the M184V mutation that confer multi NRTI resistance was created by site directed mutagenesis [25], produced in HEK-293T cells, and normalized by ELISA anti p24 antigen. The same amount of virus was used to infect GHOST cells in the presence of increasing concentrations of 3TC or oATP. As shown in Fig. (**8A**), the NL4-3 Luc M184V was resistant to 3TC treatment with a fold resistance up to 25x the IC_{50} described for wild type virus (0.18 μM) [39]. However, oATP was effective in inhibiting HIV infection of both wild type and M184V virus (Fig. **8B**). oATP also restrained *in vitro* RT activity of the M184V virus (data not shown).

A set of mutations, known as thymidine analog mutations (TAMs) emerged in patients as distinctive mutations leading to AZT resistance. To evaluate if oATP is still effective in these HIV-1 variants, we created a NL4-3 Luc gp120 virus with RT carrying the T215Y mutation, the most prevalent TAM [40] and infected GHOST cells in the presence of increasing concentrations of AZT or oATP. The NL4-3 Luc T215Y virus was resistant to AZT treatment with a fold resistance up to 5x the IC_{50} described for wild type virus (0.003 μM) [41] (Fig. **8C**). The oATP was again effective in inhibiting HIV infection of both wild type and T215Y virus (Fig. **8D**). These results demonstrated the potential of oATP to affect RT activity even in viruses harboring NRTI resistant mutations.

Molecular Docking

The fact that oATP can inhibit HIV-1 RT DNA polymerization and having modifications at ribose ring as AZT and other NRTIs, prompted us to study its interaction with HIV-1 RT. In order to identify oATP binding site in HIV-1 RT, a search on Protein Data Bank was done for NRTIs previously complexed to enzyme. Accordingly, Zidovudine triphosphate (AZTTP) was identified and employed as reference for docking calculations (Fig. **9A**). Centered on AZTTP binding sites, oATP were submitted to docking calculations including compound flexibility and the so obtained complexes were compared to the crystallographic data, suggesting a similar binding patter between the two compounds (Fig **9**) and similar interaction with equivalent amino acid residues (Ala114, Asp113).

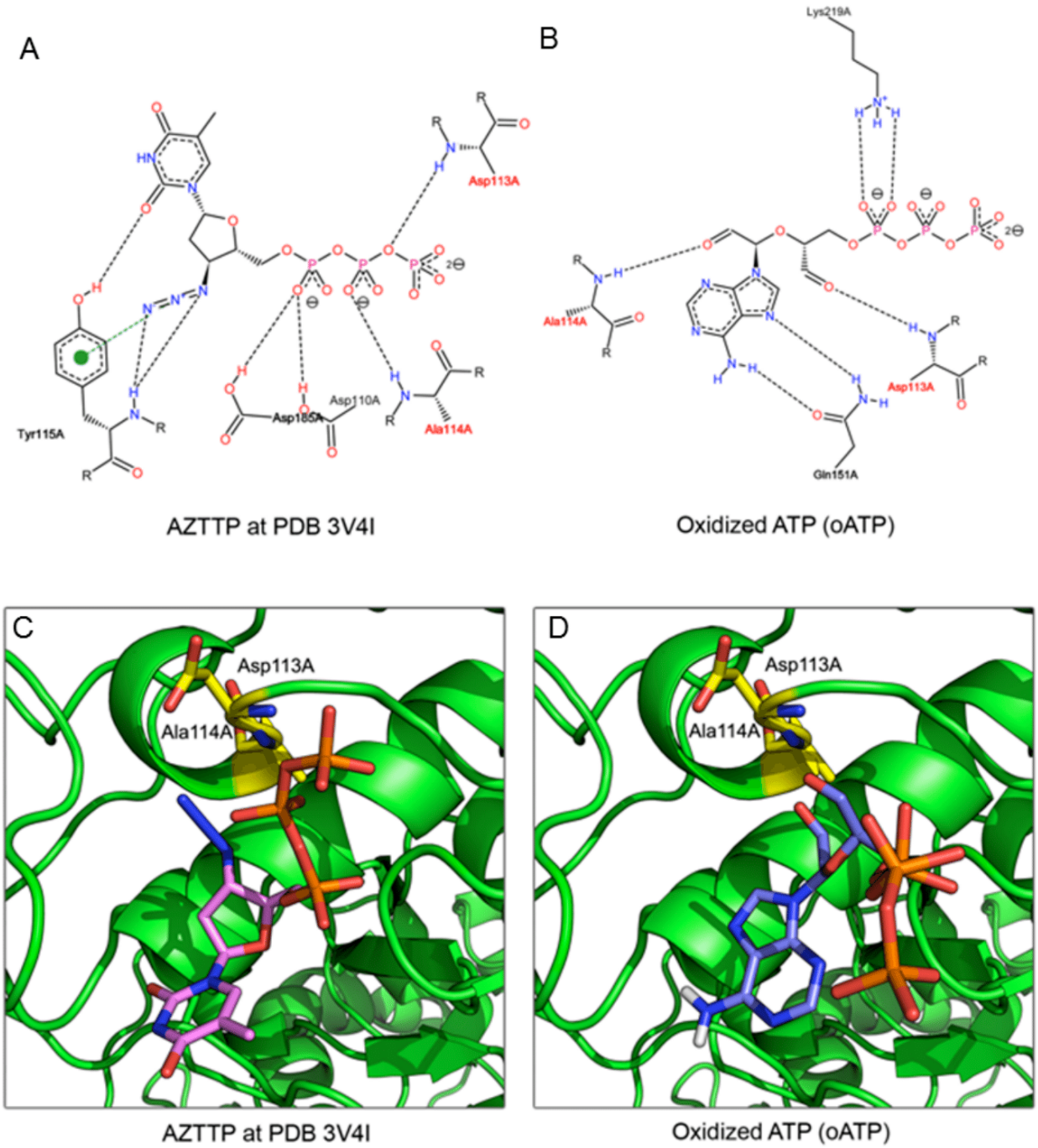

Fig. (9). Binding patterns of AZTTP and oATP. 2D representation of AZTTP (**A**) and oATP (**B**) binding to RT. The main amino acid residues on compounds binding to RT are presented. Amino acid residues highlighted (red) indicate interactions observed between both compounds. Crystallographic AZTTP-RT (**C**) and docking result of oATP (**D**). Common amino acid residues for both complexes are indicated as yellow sticks.

DISCUSSION

In this study, we report the inhibitory effect of oATP on HIV-1 replication in primary macrophages and GHOST cells (Figs. **1**, **7**). The inhibitory effect of oxidized nucleotides on RT activity was demonstrated using an *in vitro* assay with virus-free enzymes (Fig. **4**) and in a system of cell-free virus particles (Fig. **5**), suggesting that oATP could also help preventing HIV-1 infection acting as microbicide directly in the virus particles and preventing infections of new cells.

Several nucleoside analogs are used as RT inhibitors, and many of them are included in the treatment of HIV/AIDS patients. oATP is an ATP derivative that is widely used as an inhibitor of P2X7 receptors [14-16] and ATP-induced P2X7-mediated immune responses both *in vitro* [42] and *in vivo*

[43-47]. These data indicate that oATP has the potential to be a useful tool to investigate new anti-HIV-1 drugs.

The first report of oATP effects on HIV-1 biology used a virus-free *in vitro* reaction to show that oATP inhibits 98% the oligonucleotide cleavage activity of HIV-1 integrase at a concentration of 500 μM [34]. However, these authors did not investigate the effects of oATP directly on RT activity or in HIV-1 infection.

We demonstrated that production of viral cDNA is significantly diminished in cells treated with oATP (Fig. **1B**) and that oATP is also effective in blocking a VSV-G-pseudotyped virus that enters the cell by other mechanism that bypasses binding to CD4 and CXCR4/CCR5 molecules (Fig. **2**). Our results presented in the Fig. (**2**) showed that oATP treatment impaired VSV-G-pseudotyped HIV as well as full HIV, clearly indicating the existence of an inhibition target step also after virus entry. Moreover, in macrophages, oATP inhibits HIV-1 replication even when added after virus entry (Fig. **7**).

These results does not exclude the possibility that oATP can also inhibit virus replication by affecting its entry into the cell as recently proposed [19, 20]. More experiments are required to elucidate fully the mechanism(s) of oATP action on HIV-1.

Our data obtained with *in vitro* assay with virus-free enzymes strongly support the direct inhibitory effect of oATP and oADP on HIV-1 RT. Recent results have demonstrated that interaction between the K65 residue of RT and the γ-phosphate of the incoming nucleotide is not required for polymerase activity, suggesting that a nucleoside diphosphate could be utilized as a substrate by RT [48-50]. This is a possible reason why oADP can also interfere with RT activity *in vitro* while oADO does not.

The inhibitory effect of oATP on RT activity on cell-free NL4-3 virus particles (NERT assay, Fig. **5**) is consistent with previous studies demonstrating that the amphipathic domain of gp41 transmembrane glycoproteins renders HIV-1 envelope permeable to dNTPs, favoring RT activity still inside the virion [26]. The oATP could also enter the virion and blocks virus RT activity. Our results concerning the potential antiviral activity of other oxidized nucleotides/nucleosides showed that oATP, oADP and oADO also inhibit endogenous RT activity and HIV-1 infection of GHOST cells, while only oATP and oADP are effective on the *in vitro* RT assay.

Because the enveloped virus is released by budding through cell membranes, several surface components are incorporated on the surface of the viral particle during its formation. In addition, intracellular proteins have also been reported to be incorporated into HIV-1 particles [51, 52]. It is possible that, in the NERT experiment, a mammalian-derived kinase from HEK-293T cells could have been able to phosphorylates oADO converting it into a RT substrate what could explain the difference between the NERT assay and enzymatic RT *in vitro* assay inhibition [10]. Our UFLC-UV analysis corroborates this hypothesis because oATP can be detected in the cell after the treatment with extracellular oADO (Fig. **6**). Others have demonstrated the intracellular effects of oATP [53]. In addition, oADO can be detected after treatment with oATP indicating that this molecule can be dephosphorylated. These results provides an explanation to why oADO is not effective in the enzymatic RT *in vitro* assay and, in addition, suggest that the viral particles incorporates a kinase activity that could phosphorylate oADO to its RT-inhibitory nucleotide.

The concentration of oATP required to inhibit completely the RT activity in the NERT assay was almost 100-fold higher relative to the dose used to inhibit virus production in GHOST cells and macrophages. This is possibly due to a characteristic of the cell-free system since the same increase in the effective dose is also required for NNRTIs such as EFV under similar conditions ([26] and Fig. **5B**).

We also showed that oATP effectively inhibits HIV-1 replication in primary macrophages, even if these cells were treated with oATP for 3 h before infection or after the initial 3 h period of virus-cell interaction and entry (Fig. **7**). These results demonstrate that the suppressive effect of oATP does not require the blockage of virus-receptor interaction and suggests a multi-step mechanism of action, possibly mediated by more than one molecular target. In addition, we showed that oATP is equally effective against the wild type and the HIV-1 variant M184V and T215Y resistant to multiple NRTIs (Fig. **8**).

The molecular docking analysis provide a potential explanation of inhibitory effect of oATP on HIV-1 RT, showing that oATP interacts with the substrate binding site as does others NRTIs (Fig. **9**). The possibility that the aldehyde could engage in covalent bonds requires further investigation.

It is also important to notice that oATP, oADP and oADO are increasingly being used as experimental tools for both *in vitro* and *in vivo* assays targeting not only P2 receptors but also ATP-binding enzymes such as ATPases and methyltransferases [15-17, 54-56]. Therefore, regardless of the relatively high doses used of these compounds, we showed that they could have multiple effects on HIV-1 infection that goes well beyond its recognized action of oATP on P2X7 receptors and that they are a useful tool to better understand the different purinergic signaling involved in the various steps of the viral cycle.

CONCLUSION

We show that oATP is able to inhibit HIV infection in primary human macrophages and GHOST cells. Our results suggest that oATP inhibits HIV RT enzyme. Our data introduces 2', 3'-dialdehydes of nucleotides and nucleoside as a new class of antiretroviral/microbicide agent acting at both pre- and post-infection stages of the HIV-1 replicative cycle.

ABBREVIATIONS

3TC = 2', 3'-dideoxy-3'-thiacytidine

AIDS = Acquired immunodeficiency syndrome

AZTTP = Zidovudine triphosphate

dNTP = Deoxynucleoside triphosphate

EFV = Efavirenz

HAART = Highly active antiretroviral therapy

NERT = Natural endogenous reverse transcriptase

NNRTI = Non-nucleoside reverse transcriptase inhibitor

NRTI = Nucleoside/nucleotide analogues reverse transcriptase inhibitor

oATP = 2'3'- dialdehyde of ATP or oxidized ATP.

oADP = 2'3'- dialdehyde of ADP or oxidized ADP

oADO = 2'3'- dialdehyde of adenosine or oxidized adenosine

PBMC = Peripheral blood mononuclear cells

RT = Reverse transcriptase

ssDNA = Strong stop DNA

CONFLICT OF INTEREST

The authors confirm that this article content has no conflicts of interest.

ACKNOWLEDGMENTS

We thank the Hemotherapy Service of the Hospital Clementino Fraga Filho of the Federal University of Rio de Janeiro for providing buffy coats. The HIV-1 isolate Ba-L, NRTI, NNRTIs, and GHOST cells were kindly donated by the AIDS Research and Reference Reagent Program, Division of AIDS, NIH (Bethesda, MD, USA).

Financial Support

This work was supported by the Conselho Nacional de Desenvolvimento Científico e Tecnológico (CNPq), Fundação Carlos Chagas Filho de Amparo à Pesquisa do Estado do Rio de Janeiro (FAPERJ), Programa de Núcleos de Excelência (PRONEX-CNPq), POM/IOC (Fiocruz), Coordenação de Aperfeiçoamento de Pessoal do Ensino Superior (CAPES), and Instituto Nacional para Pesquisa Translacional em Saúde e Ambiente na Região Amazônica, Conselho Nacional de Desenvolvimento Científico e Tecnológico/MCT (INCT-INPeTAm/CNPq/MCT), Brasil.

REFERENCES

[1] Berger EA, Murphy PM, Farber JM. Chemokine receptors as HIV-1 coreceptors: roles in viral entry, tropism, and disease. Annu Rev Immunol 1999; 17: 657-700.

[2] Hull MW, Montaner J. Antiretroviral therapy: a key component of a comprehensive HIV prevention strategy. Current HIV/AIDS Reports 2011; 8: 85-93.

[3] UNAIDS. (2011). GLOBAL HIV/AIDS RESPONSE Epidemic update and health sector progress towards Universal Access. Progress report 2011. In.

[4] Anderson KS. Perspectives on the molecular mechanism of inhibition and toxicity of nucleoside analogs that target HIV-1 reverse transcriptase. Biochim Biophys Acta 2002; 1587: 296-299.

[5] Borkow G, Barnard J, Nguyen TM *et al*. Chemical barriers to human immunodeficiency virus type 1 (HIV-1) infection: retrovirucidal activity of UC781, a thiocarboxanilide nonnucleoside inhibitor of HIV-1 reverse transcriptase. J Virol 1997; 71: 3023-30.

[6] De Clercq E. New developments in anti-HIV chemotherapy. Biochim Biophys Acta 2002; 1587: 258-75.

[7] Adamson CS, Freed EO. Novel approaches to inhibiting HIV-1 replication. Antiviral Res 2010; 85: 119-41.

[8] Easterbrook-Smith SB, Wallace JC, Keech DB. Pyruvate carboxylase: affinity labelling of the magnesium adenosine triphosphate binding site. Eur J Biochem 1976; 62: 125-30.

[9] Westcott KR, Olwin BB, Storm DR. Inhibition of adenylate cyclase by the 2',3'-dialdehyde of adenosine triphosphate. J Biol Chem 1980; 255: 8767-71.

[10] Kochetkov SN, Bulargina TV, Sashchenko LP *et al*. Studies on the mechanism of action of histone kinase dependent on adenosine 3':5'-monophosphate. Evidence for involvement of histidine and lysine residues in the phosphotransferase reaction. Eur J Biochem 1977; 81: 111-8.

[11] Fournier M, Labouesse B, Labouesse J. Reaction of tryptophanyl-tRNA synthetase from beef pancreas with periodate-oxidized ATP. Eur J Biochem 1987; 167: 533-40.

[12] Mignaco J, Scofano HM, Barrabin H. Inhibition and labeling of the Ca2(+)-ATPase from sarcoplasmic reticulum by periodate oxidized ATP. Biochim Biophys Acta 1990; 1039: 305-12.

[13] Bernikov LR, Dzhandzhugazyan KN, Lutsenko SV *et al*. Dialdehyde ATP derivative as an affinity modifier of the Na+, K(+)-ATPase active site. Eur J Biochem 1990; 194: 413-21.

[14] Murgia M, Hanau S, Pizzo P *et al*. Oxidized ATP an irreversible inhibitor of macrophage purinergic P2Z receptor. J Biol Chem 1993; 268: 8199-203.

[15] Di Virgilio F. Novel data point to a broader mechanism of action of oxidized ATP: the P2X7 receptor is not the only target. Br J Pharmacol 2003; 140: 441-3.

[16] Gever JR, Cockayne DA, Dillon MP *et al*. Pharmacology of P2X channels. Pflugers Arch 2006; 452: 513-37.

[17] Hattori F, Ohshima Y, Seki S *et al*. Feasibility study of B16 melanoma therapy using oxidized ATP to target purinergic receptor P2X7. Eur J Pharmacol 2012.

[18] Barat C, Gilbert C, Imbeault M *et al*. Extracellular ATP reduces HIV-1 transfer from immature dendritic cells to CD4+ T lymphocytes. Retrovirology 2008; 5: 30.

[19] Seror C, Melki MT, Subra F *et al*. Extracellular ATP acts on P2Y2 purinergic receptors to facilitate HIV-1 infection. J Exp Med 2011; 208: 1823-34.

[20] Hazleton JE, Berman JW, Eugenin EA. Purinergic Receptors Are Required for HIV-1 Infection of Primary Human Macrophages. J Immunol 2012; Published online before print March 26, 2012, doi: 10.4049/jimmunol.1102482.

[21] Regis EG, Barreto-de-Souza V, Morgado MG *et al*. Elevated levels of macrophage migration inhibitory factor (MIF) in the plasma of HIV-1-infected patients and in HIV-1-infected cell cultures: a relevant role on viral replication. Virology 2010; 399: 31-8.

[22] Morner A, Bjorndal A, Albert J *et al*. Primary human immunodeficiency virus type 2 (HIV-2) isolates, like HIV-1 isolates, frequently use CCR5 but show promiscuity in coreceptor usage. J Virol 1999; 73: 2343-9.

[23] Aguiar RS, Lovsin N, Tanuri A *et al*. Vpr.A3A chimera inhibits HIV replication. J Biol Chem 2008; 283: 2518-25.

[24] Mariani R, Chen D, Schrofelbauer B *et al*. Species-specific exclusion of APOBEC3G from HIV-1 virions by Vif. Cell 2003; 114: 21-31.

[25] Johnson VA, Brun-Vezinet F, Clotet B *et al*. Update of the drug resistance mutations in HIV-1: December 2010. Top HIV Med 2010; 18: 156-63.

[26] Aguiar RS, Costa LJ, Pereira HS *et al*. Development of a new methodology for screening of human immunodeficiency virus type 1 microbicides based on real-time PCR quantification. Antimicrob Agents Chemother 2007; 51: 638-44.

[27] Coomber DW, O'Sullivan WJ, Gero AM. Adenosine analogues as antimetabolites against Plasmodium falciparum malaria. Int J Parasitol 1994; 24: 357-65.

[28] Schaftenaar G, Noordik JH. Molden: a pre- and post-processing program for molecular and electronic structures. J Comput Aided Mol Des 2000; 14: 123-34.

[29] Schmidt MW, Baldridge KK, Boatz JA *et al*. General atomic and molecular electronic structure system. J Comput Chem 1993; 14: 1347-6313.

[30] Morris GM, Huey R, Lindstrom W *et al*. AutoDock4 and AutoDockTools4: Automated docking with selective receptor flexibility. J Comput Chem 2009; 30: 2785-91.

[31] Morris GM, Goodsell DS, Halliday RS *et al*. Automated docking using a Lamarckian genetic algorithm and an empirical binding free energy function. J Comput Chem 1998; 19: 1639-62.

[32] Stierand K, Rarey M. Drawing the PDB: Protein-ligand complexes in two dimensions. ACS Medic Chem 2010; 1: 540-5.

[33] Delano WL. (2002). The PyMOL Molecular Graphics System. DeLano Scientific, Sao Carlos, CA, USA, 2002. http://www.pymol.org. In.

[34] Lipford JR, Worland ST, Farnet CM. Nucleotide binding by the HIV-1 integrase protein *in vitro*. J Acquir Immune Defic Syndr 1994; 7: 1215-23.

[35] Yokoyama M, Mori H, Sato H. Allosteric Regulation of HIV-1 Reverse Transcriptase by ATP for Nucleotide Selection. PLoS ONE 2010; 5: e8867.

[36] Lowe PN, Baum H, Beechey RB. Preparation and chemical properties of periodate-oxidized adenosine triphosphate and some related compounds [proceedings]. Biochem Soc Trans 1979; 7: 1131-3.

[37] Zhang H, Dornadula G, Alur P *et al*. Amphipathic domains in the C terminus of the transmembrane protein (gp41) permeabilize HIV-1 virions: a molecular mechanism underlying natural endogenous reverse transcription. Proc Natl Acad Sci U S A 1996; 93: 12519-24.

[38] Souza TM, Rodrigues DQ, Passaes CP *et al*. The nerve growth factor reduces APOBEC3G synthesis and enhances HIV-1 transcription and replication in human primary macrophages. Blood 2011; 117: 2944-52.

[39] Coates JA, Cammack N, Jenkinson HJ *et al*. (-)-2'-deoxy-3'-thiacytidine is a potent, highly selective inhibitor of human immunodeficiency virus type 1 and type 2 replication *in vitro*. Antimicrob Agents Chemother 1992; 36: 733-9.

[40] Boyer PL, Sarafianos SG, Arnold E *et al*. Selective excision of AZTMP by drug-resistant human immunodeficiency virus reverse transcriptase. J Virol 2001; 75: 4832-42.

[41] Balzarini J, Baba M, Pauwels R *et al*. Anti-retrovirus activity of 3'-fluoro- and 3'-azido-substituted pyrimidine 2',3'-dideoxynucleoside analogues. Biochem Pharmacol 1988; 37: 2847-56.

[42] Di Virgilio F, Boeynaems JM, Robson SC. Extracellular nucleotides as negative modulators of immunity. Curr Opin Pharmacol 2009; 9: 507-13.

[43] Fang KM, Wang YL, Huang MC *et al*. Expression of macrophage inflammatory protein-1alpha and monocyte chemoattractant protein-1 in glioma-infiltrating microglia: involvement of ATP and P2X receptor. J Neurosci Res 2011; 89: 199-211.

[44] Schenk U, Westendorf AM, Radaelli E *et al*. Purinergic control of T cell activation by ATP released through pannexin-1 hemichannels. Sci Signal 2008; 1: ra6.

[45] Choi HB, Ryu JK, Kim SU *et al*. Modulation of the purinergic P2X7 receptor attenuates lipopolysaccharide-mediated microglial activation and neuronal damage in inflamed brain. J Neurosci 2007; 27: 4957-68.

[46] Dell'Antonio G, Quattrini A, Dal Cin E *et al*. Antinociceptive effect of a new P(2Z)/P2X7 antagonist, oxidized ATP, in arthritic rats. Neurosci Lett 2002; 327: 87-90.

[47] Wang X, Arcuino G, Takano T *et al*. P2X7 receptor inhibition improves recovery after spinal cord injury. Nat Med 2004; 10: 821-7.

[48] Furman PA, Fyfe JA, St Clair MH *et al*. Phosphorylation of 3'-azido-3'-deoxythymidine and selective interaction of the 5'-triphosphate with human immunodeficiency virus reverse transcriptase. Proc Natl Acad Sci U S A 1986; 83: 8333-7.

[49] Garforth SJ, Parniak MA, Prasad VR. Utilization of a deoxynucleoside diphosphate substrate by HIV reverse transcriptase. PLoS ONE 2008; 3: e2074.

[50] Johnson MA, Ahluwalia G, Connelly MC *et al*. Metabolic pathways for the activation of the antiretroviral agent 2',3'-dideoxyadenosine in human lymphoid cells. J Biol Chem 1988; 263: 15354-7.

[51] Giroud C, Chazal N, Briant L. Cellular kinases incorporated into HIV-1 particles: passive or active passengers? Retrovirology 2011; 8: 71.

[52] Chertova E, Chertov O, Coren LV *et al*. Proteomic and biochemical analysis of purified human immunodeficiency virus type 1 produced from infected monocyte-derived macrophages. J Virol 2006; 80: 9039-52.

[53] Henke W, Hagen T, Jung K *et al*. Periodate-oxidized ATP stimulates the permeability transition of rat liver mitochondria. Biochim Biophys Acta 1998; 1363: 209-16.

[54] Moayeri M, Wickliffe KE, Wiggins JF *et al*. Oxidized ATP protection against anthrax lethal toxin. Infect Immun 2006; 74: 3707-14.

[55] Shiota M, Takeuchi A, Yokomizo A *et al*. Methyltransferase inhibitor adenosine dialdehyde suppresses androgen receptor expression and prostate cancer growth. J Urol 2012; 188: 300-6.

[56] Bostrom B, Hogenkamp HP, Mirkin BL. Inhibitory effect of adenosine dialdehyde on in situ murine neuroblastoma growth. Cancer Res 1988; 48: 5933-6.

Received: January 26, 2014 **Revised: June 11, 2014** **Accepted: August 15, 2014**

9.3 APÊNDICE C

Effects of TMI binding on antithrombin and comparison with the heparin binding

Pablo Ricardo Arantes,[a] Horacio Pérez-Sánchez[b] and Hugo Verli[a,*]

[a] *Centro de Biotecnologia, Universidade Federal do Rio Grande do Sul, Av Bento Gonçalves 9500, CP 15005, Porto Alegre 91500-970, RS, Brazil*

[b] *Bioinformatics and High Performance Computing Research Group, Computer Science Department, Universidad Católica San Antonio de Murcia (UCAM), Spain*

Graphical Abstract:

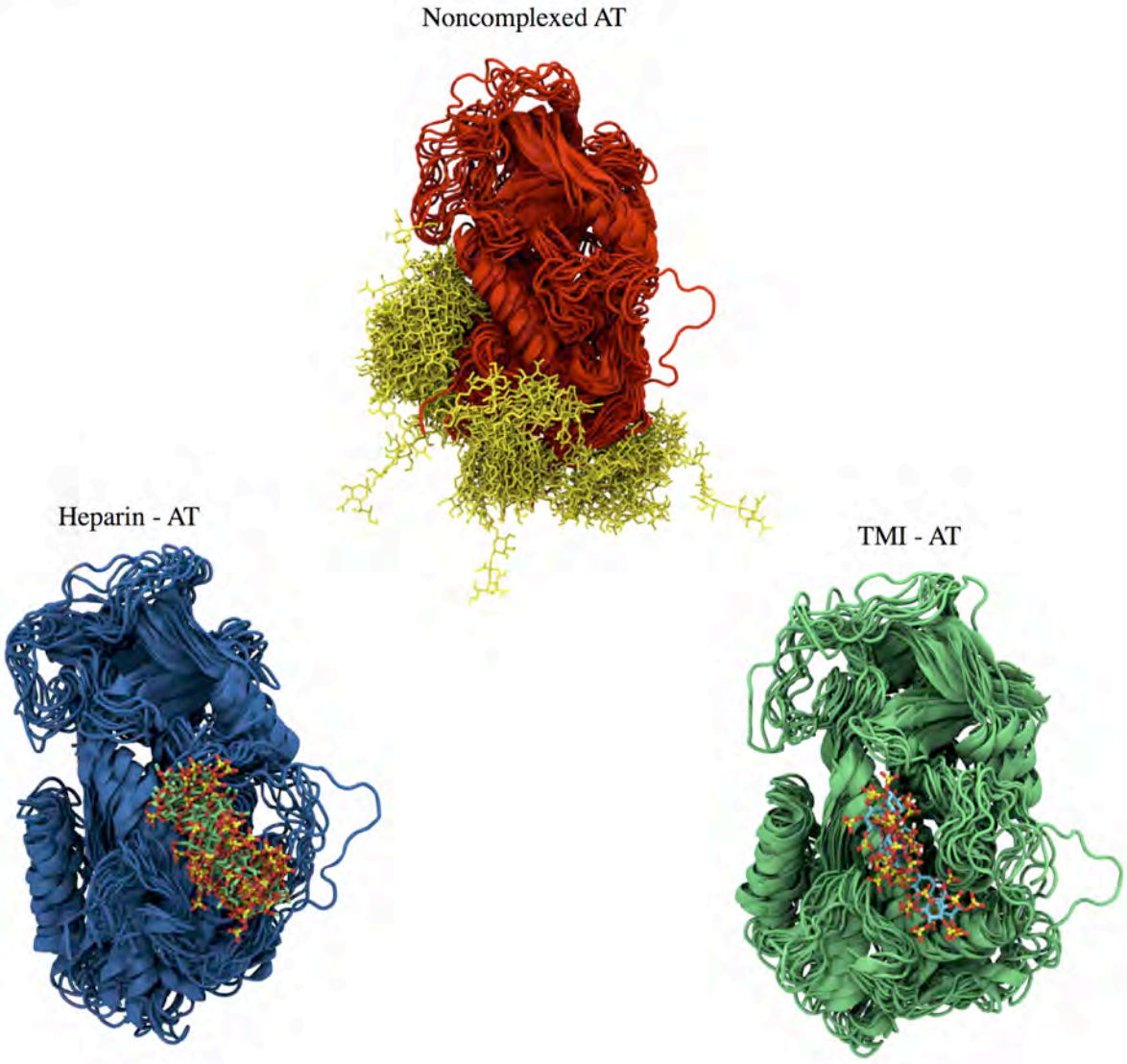

*Corresponding author. Tel.: +55-51-3308-7770; fax: +55-51-3308-7309; e-mail address: hverli@cbiot.ufrgs.br. URL: http://www.ufrgs.br/bioinfo

9.4 APÊNDICE D

Bioinformática: da Biologia à Flexibilidade Molecular

In Verli (Ed.), 2014

Distribuição eletrônica gratuita no endereço: http://www.ufrgs.br/bioinfo/ebook/

Elaboração de Imagens: **Pablo Ricardo Arantes**

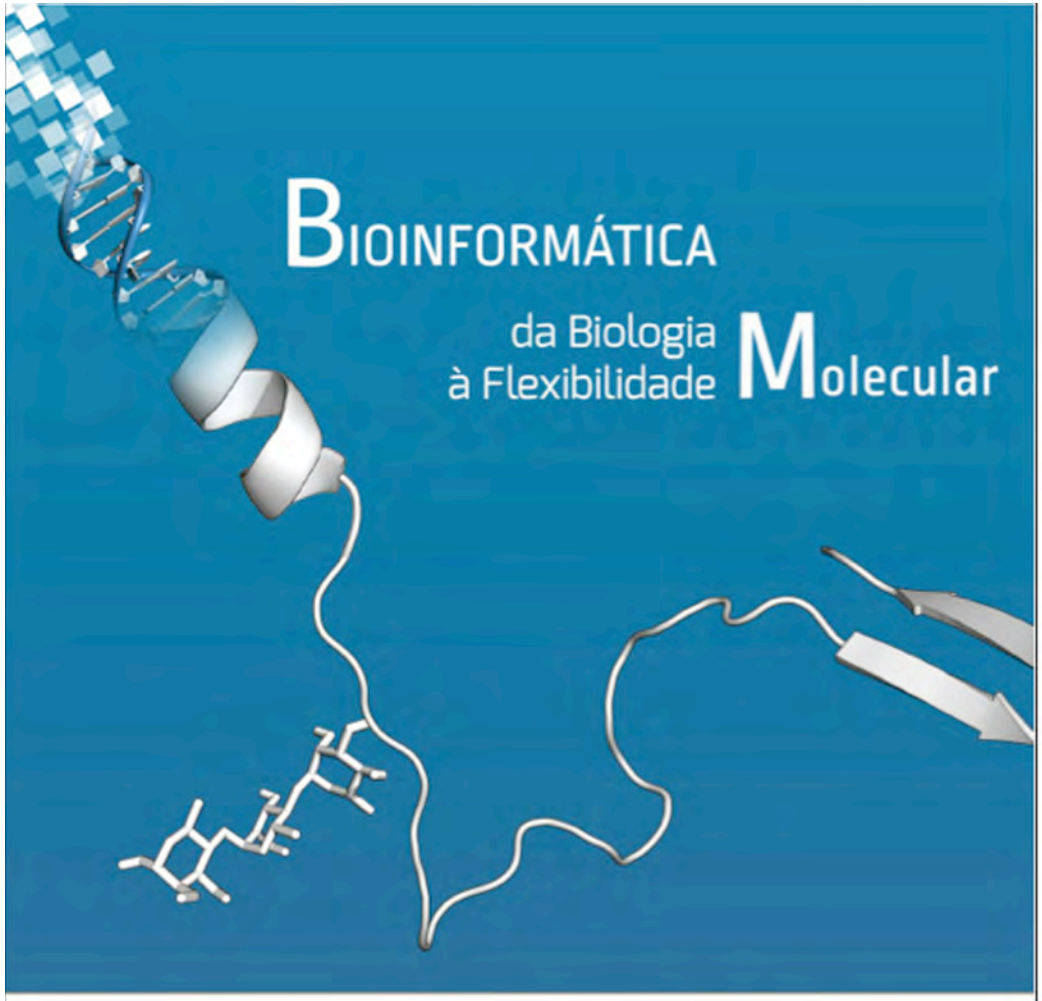

Bioinformática
da Biologia à Flexibilidade Molecular

Hugo Verli (org)

Apoio:
CNPq CAPES FAPERGS UFRGS

Elaboração de imagens

Pablo Ricardo Arantes
pablitoarantes@gmail.com

Revisão de texto

Liana Guimarães Sachett
lianasachett@gmail.com

10. CURRICULUM VITÆ

I. Formação acadêmica

Graduação em Farmácia pela Universidade Federal do Rio Grande do Sul, de 2007/1 a 2011/2. *Caracterização Estrutural e Conformacional do Sulfato de Condroitina Através de Simulações de Dinâmica Molecular*. Orientador: Prof. Hugo Verli.

Mestrado em andamento em Biologia Celular e Molecular pelo Programa de Pós-Graduação em Biologia Celular e Molecular pela Universidade Federal do Rio Grande do Sul, de 2013/1 a 2014/2. *Comparação de Diferentes Campos de Força na Descrição Conformacional de siRNAs*. Orientador: Hugo Verli.

Doutorado em andamento em Biologia Celular e Molecular pelo Programa de Pós-Graduação em Biologia Celular e Molecular pela Universidade Federal do Rio Grande do Sul, a partir de 2014/2. *Glicobiologia Estrutural da Flipase PglK na Via de N-glicosilação*. Orientador: Hugo Verli.

II. Prêmios recebidos

XXII Salão de Iniciação Científica, 2012: Destaque de sessão na área de Ciências Exatas e da Terra - Sessão: Simulação e Modelagem Molecular, UFRGS. Caracterização Conformacional dos Ipomatosideos. Orientador: Hugo Verli.

III. Trabalhos científicos apresentados em congressos

Arantes, P.R.; Verli, H.: Force Fields Reliability on the Description of Protein complexed and uncomplexed siRNA. XLIII Reunião Anual da Sociedade Brasileira de Bioquímica e Biologia Molecular, 2014, Foz do Iguaçu / PR.

Pedebos, C.; **Arantes, P.R.**; Verli, H.: Structural Glycobiology of the Oligosaccharyltransferase PglB from Campylobacter lari. XLIII Reunião Anual da Sociedade Brasileira de Bioquímica e Biologia Molecular, 2014, Foz do Iguaçu / PR.

Trindade, V.M.T.; **Arantes, P.R.**; Zanatta, G.; Salbego, C.G.: Virtual Determination of Liver and Muscle Glycogen Obtained from Fed Rats and from 24-Hour Fasted Rats. XLIII Reunião Anual da Sociedade Brasileira de Bioquímica e Biologia Molecular, 2014, Foz do Iguaçu / PR.

Arantes, P.R.; Verli, H.: Dynamics of siRNAs: Comparison of Force Fields Reliability. XLII Reunião Anual da Sociedade Brasileira de Bioquímica e Biologia Molecular, 2013, Foz do Iguaçu / PR.

Trindade, V.M.T.; **Arantes, P.R.**; Zanatta, G.; Zimmer, E.R.; Ewald, L.; Pettenuzzo, L.F.; Matté, C.; Salbego, C.G.: Evaluation of Serum Lactate Dehydrogenase Activity in a Virtual Environment. XLII Reunião Anual da Sociedade Brasileira de Bioquímica e Biologia Molecular, 2013, Foz do Iguaçu / PR.

Arantes, P.R.; Verli, H.: Conformational Characterization of Ipomotaosides. XLI Reunião Anual da Sociedade Brasileira de Bioquímica e Biologia Molecular, 2012, Foz do Iguaçu / PR.

Arantes, P.R.; Verli, H.: Caracterização Conformacional dos Ipomatosideos. XXIV Salão de Iniciação Científica, 2012, Porto Alegre / RS. Livro de resumos - XXIV Salão de Iniciação Científica, 2012.

Arantes, P.R.; Fernandes, C.L.; Andrade de Lima, M.; Cunha de Farias, E.H.; Verli, H.: Conformation-toxicity relationship on oversulfated chondroitin sulfate. XL Reunião Anual da Sociedade Brasileira de Bioquímica e Biologia Molecular, 2011, Foz do Iguaçu / PR. Programa e Resumos da XL Reunião Anual da Sociedade Brasileira de Bioquímica e Biologia Molecular, 2011.

Arantes, P.R.; Verli, H.: Estudo da Relação entre Conformação e toxicidade no Sulfato de Condroitina Supersulfatado. XXIII Salão de Iniciação Científica, 2011, Porto Alegre / RS. Livro de resumos - XXIII Salão de Iniciação Científica e XX Feira de Iniciação Científica, 2011.

Arantes, P.R.; Zanatta, G.; Zimmer, E.R.; Ewald, L.; Salbego, C.G.; Trindade, V.M.T.: Avaliação da Atividade da Enzima Lactato Desidrogenase Sérica num Ambiente Virtual. XXI Salão de Iniciação Científica, 2009, Porto Alegre / RS.

IV. Publicações em periódicos especializados

Trindade, V.M.T.; Zanatta, G.; **Arantes, P.R.;** Blanco, I.S.; Demore, F.P.; Salbego, C.G. Virtual laboratory activities in basic Biochemistry*. Procedia – Social and Behavioral Sciences,* **2013**, *106*, 3329-3334.

Arantes, P.R.; Sachett, L.G.; Graebin, C.S.; Verli, H. Conformational Characterization of Ipomotaosides and Their Recognition by COX-1 and 2. *Molecules,* **2014**, *19*, 5421-5433.

Schachter, J.; Valadão, A.L.C.; Aguiar, R.S.; Barreto-de-Souza, V.; Rossi, A.D.; **Arantes, P.R.;** Verli, H.; Quintana, P.G.; Heise, N.; Tanuri, A.; Bou-Habib, D.C.; Persechini, P.M. *2´,3´*-Dialdehyde of ATP, ADP, and Adenosine Inhibit HIV-1 Reverse Transcriptase and HIV-1 Replication. *Current HIV Research*, **2014**, *12*, 301-308 “Accepted Article”.

V. Bolsa recebida

Bolsista CNPq de 20010/1 a 2012/2.

Bolsista CAPES – GM do programa de mestrado em biologia molecular e celular pelo Centro de Biotecnologia da UFRGS de março de 2013 a julho de 2014.

Bolsista CAPES do programa de doutorado em biologia molecular e celular pelo Centro de Biotecnologia da UFRGS a partir de agosto de 2014.